Design of Robotically Manufactured Composites for Optimal Structural Performance, Incorporating Manufacturing Constraints

by

Avinkrishnan Ambika Vijayachandran

A dissertation submitted in partial fulfillment
of the requirements for the degree of
Doctor of Philosophy
(Aerospace Engineering)
in The University of Michigan
2021

Doctoral Committee:

Professor Anthony M. Waas, Chair
Professor Kazuhiro Saitou
Professor Henry Sodano
Professor Veera Sundararaghavan

Avinkrishnan Ambika Vijayachandran

avinav@umich.edu

ORCID iD: 0000-0003-1134-1102

To, *Amma* and *Achan*

Chettan, *Chechi* and *Appu*

ACKNOWLEDGEMENTS

Writing this dissertation is the culmination of five years of doctoral studies at the University of Michigan (UM) and the University of Washington (UW). Much has happened in the last five years, but certainly, this would have not been possible without the constant support, mentoring, advise and camaraderie of many individuals. Here I would like to take a moment to acknowledge and thank all of them for their help.

I want to sincerely thank my advisor Dr. Anthony M. Waas. My journey in research started when I took the course AEROSP516- Mechanics of Fibrous Composites, in Fall of 2014. I remember Prof. Waas saying *"This class has resulted in many Ph.D theses"*, and here I am. I was bewildered by his passion for Mechanics, inspired by his enthusiasm and motivated by his encouragement and support over the years. I have learned both Mechanics and life from Prof. Waas. Some of it took many repetitions of his advice; and I am afraid I have missed quite a few of them still.

I have been very privileged to have as my committee members - Prof. Veera Sundararaghavan, Prof. Henry Sodano and Prof. Kazuhiro Saito. Prof. Sundaraghavan mentored me during my Masters' studies at Michigan, and encouraged me to start my doctoral studies with Prof. Waas.

I want to emphasize my gratitude for Dr. S. Rao Varanasi and Dr. Usha Varansi (who I fondly call *Ushamma*) for the two years of endowment fellowship at Washington, and more importantly the parental care and love they ushered on me. I have warm memories of the many discussions on Mechanics with Dr. Rao and the many

recipes and garden tips shared by *Ushamma*.

I want to thank Dr. Paul Davidson for being my mentor in the group, and relentlessly helping me figure out my way around research, many a times.

I am grateful for the guidance of Prof. Jerry Lynch, Prof. Carlos Cesnik and Prof. John Shaw at UM and Prof. Marco Salviato, Prof. Jinkyu Yang and Prof. Peter Mackenzie-Helnwein at UW. I would like to thank my structures professors during my undergraduate studies at NITK, Prof. K. Swaminathan and Prof. Katta Venkataramana for nurturing my interest in Structural Engineering, and my high school Physics teacher Mrs. Ambili. K. I and English teacher Mrs. Jaya Ashok for their support, love and encouragement. I humbly acknowledge the discipline inculcated by the principal of Arya Central School, Mrs. Gayathri Radhakrishnan.

I appreciate the financial support from 'Toray' , Electroimpact and JCATI. I would like to thank John Nancarrow and Andrew Purvis from Electroimpact, and Damon Call and Dongyeon Lee from 'Toray' for helping with manufacturing experimental parts for my studies.

I gratefully acknowledge the support of Prof. Krzysztof Fidkowski and Ed Connery for helping with the transition from UW to UM.

I am also grateful for the support in the department at UM - Terry Larrow, for all the help with making fixtures for my experiments and the abundant help he provided to get my work done better- You have been a super human and a saving grace! I appreciate the prompt help from Ruthie Freeman for all the doctoral paperwork- you are the best and UM-Aero and grad students are lucky to have you! I am thankful for the kind help of Gwen Brown for all the support with meetings and department activities, and Kimberly Johnson for being a friend, mentor and leader for my outreach activities. Many thanks to Tom, David, Sam and Chris for all the technical support in FXB, Jessica for navigating all the HR paperwork, Denise for grad support and Xin for prompt purchasing of my many orders while working on experiments.

I would also like to thank Svenja Fleischer , Michelle Hickner and Bill Kuykendal at UW composites shop and Dzung Tran at UW Aeronautics & Astronautics (UWAA) for all the help with manufacturing laminates and fixtures for my work. Thanks to Kim Maczko and Wanda Frederick for help with scheduling and department activities at UWAA.

I would like to thank my comrades in this journey- Shiyao Lin and Minh Hoang Nguyen. From experiments to a tedious move from Seattle to Ann Arbor, many a conferences, many hotpots, dinners and picnics- we spent good times helping keep each other sane in this journey.

I gratefully acknowledge the help and support of lab members at the Composite Structures Lab over the years, both in Ann Arbor and in Seattle- Dr.Ashith Joseph, Linda Leben, Dr. Ibrahim Kaleel, Alastair Croxford, Dr. Royan J. D'mello, Bao Ngo, Andrew Seamone, James Finlay, Jose Fernando Rojas Sanchez, Adam Kelly, Elisheva Philips, David Singer, Drew Kang, Dr. Deepak Patel and Dr. Armanj Hasanyan.

The greatest asset in the last five years (and before) has been a hotline of friends- Dr. Pınar Acar ,Dr. Doğa Can Su Öztürk and Dr. Setsuko Yokoyama. The many dinners we cooked, the mom recipes, the roadtrip to Chicago and Urbana Champaign, their Ph.D. defenses (and the food we cooked for them, ofcourse), to many many many days and nights of comforting, venting, laughing- QTs/QTzzz as we would call it, ready to help at the snap-of-a-finger.

I would like to express my gratitude for my care providers Dr. Elizabeth Cardinale, Dr. Jasmine Parvaz, Dr. Marianne Carle and Lauren Tatersky for all the help and support in the last five years.

To Dr. Michel Riquelme Sanderson- the first friend I made in Seattle and my Seattle *guru*- for all the emotional support and advice and fun over the years. To, Aditya Kapur, for loving me genuinely and being there to boost my morale in any trouble- professional or personal. To David Day, for the many many brunches and

walks around Greenlake and down to Sand point, and for the ritual of letting me have a few sips of your hot chocolate at *Chocoloati* during all those Greenlake walks. To Linda Leben (again), for the many days of encouragement and venting both during and after Seattle. To, Michael Pasquale for all the fun and brunches and symphonies. To my adopted sister, Norah Fisher for the many food that we made and the moral support. To Bryan King, for all the workouts together and cheering me up during those dull Seattle days. To Rudy Gonzalez, Benjamin Davis and Dr. Aditya Kapoor for the wonderful memories. All of you helped me feel at home in Seattle.

To Saurabh Koparkar, a saving grace in Ann Arbor, for all the times you showed up when I needed support, for all the walks and dinners and brunches and gossips. To Dr. Ian Colloway, for all the movies and walks and drinks. To Najwat Rehman, for being my first *'disciple'*. All of you made me feel at home in Ann Arbor for the last three years.

To Dr. Vivek Bhaskar Kote, who has been an adopted brother in my journey since college and all through my PhD- from gossips, to mechanics to job hunt to life advice- in a two-way street. To Hamza Bilal, for being the most giving person I have known- the many many many times you were there to cheer me up, drive me around, talk and workout. To Prashanth Jayaram for the most complicated sounding simple man that you are- for the fun to food to gossip to all the help- you have had my back since the beginning of grad school at Umich, and Shweta Srinivasan for joining the journey to make it even merrier.

Dr. Albert Thomas who has been a brother, mentor and friend, Jis Thomas who wsa a perennial source of encouragement, and Adiv and Neva for being the bundles of joy. To Apexit Shah, for being the goofiest roomate and my comrade in figuring out how to live in America. To Nikhil Ashok for making me feel like a responsible elder brother, for the many discussions we had on Mechanics. To Dr. Vinay Damodaran, for all the help and support during college and grad school. To my *bestest* friends-

Unnikrishnan B.M, Aravind Karthikeyan and Jennie Unnikrishnan, you have been my biggest cheer leaders for ever. To Deepthy Mukundan, for all the fun and laugh and the many a times you made me feel I am not the dumbest one (by just existing!). To Aahana Ranjit Balan, for the trust in me and all the encouragement.

To my friends at UW, Siddharth Rajagopal, Rupesh Kutte, Anmol Purohit, Karthik Unnikrishnan, Ajay Dhavane and Rakesh Rao for the many fun nights and picnics and celebrations. To Dr. Siddhartha Srivastava, Aaditya Lakshmanan, Yifan Bai and Tran Huynh for all the good memories in Michigan.

Thanks to my cousin Anoop Azad for all the support and encouragement, and many a nights of hearing my troubles and sharing his. Thanks to my aunts Aruna, Anna, Aisha and Animol; uncles Azad. M and K. Somadevan, and my cousins Aashi chechi and Renju chettan for all their love.

I cannot have had this journey in the last three years without the love and friendship of Dr. Arun Thomas, for which I am thankful.

I dedicate this dissertation in appreciation of the selfless love of my family. I am fortunate to have all the endless love and support of my *Amma*, Ambika Madhavan Pillai and *Achan*, K. Vijayachandran. I don't think there are words that can describe how much I feel humbled by all you have given me. To my *Chettan* Harikrishnan for being my rock solid support- showing the path for me in studies, steering me into Mechanics and Composites, leading to this dissertation; to my *Chechi*, Saritha Sajeev and nephew Aarav Krishnan (Appu) for all the love, care and support.

Avinkrishnan Ambika Vijayachandran

TABLE OF CONTENTS

LIST OF FIGURES

Figure

LIST OF TABLES

Table

LIST OF APPENDICES

Appendix

ABSTRACT

Robotic manufacturing of composites has revolutionized the aerospace industry. Traditional manufacturing of carbon fiber composite laminates involved manual hand lay-up of resin pre-impregnated sheets (prepregs) of pristine material. Such lay-up used to be cumbersome and time consuming, as well as inefficient. There is no repeatability of parts, and the method produced significant scrap material. The challenge significantly rises as the parts become larger and complex. Robotic Automated Fiber Placement (RAFP) and Automated Tape Laying (ATL) are the two robotic manufacturing techniques for CFRP laminates. While RAFP lays down "tows" of prepreg material, ATL is used for dry layup which shall require a resin infusion before curing. RAFP has started to be widely used in large scale manufacture of aerospace structures. With aircraft like the Boeing 787, Airbus A350-XWB and Airbus A220 having significant percentage of load bearing composite members, it is imperative to resort to faster and repeatable manufacturing techniques.

RAFP technology also opens up a design space that was previously not explored in traditional manufacture of laminates. An aircraft structural designer now has the capability to derive optimal fiber paths that could be steered, to be spatially varying based on the applied loads and boundary conditions. While the idea of steered fiber paths have been explored since the early 1990's, there has been a recent interest in designing parts for optimal structural performance. It is noted that while RAFP has many benefits, the drawback of the technology is manufacturing induced *defects* like gaps, overlaps and wrinkles of the fiber *"courses"*, generally called the manufacturing

signature (MS). In this work, explicit care has been given to incorporate parameters that drive the manufacturing signatures within the optimization framework, so as to produce realistic, manufacturable structural parts for improved structural performance. Some of the distinctive contributions of this work include- use of parametric curves to model center-lines of individual fiber paths, use of a global manufacturing mesh to reduce the number of optimization variables, explicitly incorporating MS into the finite element framework and including the geometrical changes arising due to compaction during manufacture, and an optimization framework in conjunction with a surrogate model built using machine learning algorithms.

Two design problems are studied - a flat plate under uni-axial and bi-axial, in-plane compressive loading, and a flat plate with an elliptical cut-out under in-plane tensile loading. The optimal designs for the uni-axial buckling are manufactured and studied for the manufacturing signatures using non destructive testing, and then subjected to in-plane compression to evaluate the laboratory performance to compare against analytical models. Further,a study on the optimal steered fiber paths is conducted for a rectangular plate with an elliptical cutout. Here the objective is to generate designs that incorporate the manufacturing signature and produce minimum stress concentration.

CHAPTER I

Introduction

The strive for lightweight structures in aerospace and aeronautical applications have driven the development of some of the cutting edge materials known to humans. These range from ceramic and metal matrix composites, carbon and glass fiber reinforced plastics (CFRP/GFRP), super alloys, textile and twill composites, 2D and 3D braided composites among others. The key to the development of these materials is the superior performance in terms of stiffness and strength while minimizing the weight of the structures, which is critical in aerospace applications. Traditionally, savings in weight meant lesser fuel burn and larger range of flight, but it is of immense importance currently in terms of controlling the emission of green house gases to minimize the human impact on climate change. The airline industry moving from a hub-and-spoke model to point-to-point model has further established the need for larger ranges for smaller aircraft. This has been evidenced in the development of aircraft like the Boeing 787 Dreamliner, Airbus 350XWB and the Airbus 220. The key factor is that more than 50% by weight and 80% by volume of the material used in these advanced aircraft are made of light weight composite material.

With the development of these materials, newer and better technologies for faster and precise manufacturing of such structures at higher throughput have also been

developed. The most advanced of them being additive manufacturing of metallic alloys, plastics and carbon fiber reinforced plastics. The design aspirations of future commercial aircraft include high aspect ratio wings that produce increased lift and highly fuel efficient, non cylindrical fuselages that are aerodynamically shape optimized, among others. Supported wings and foldable wings have already been included in development of current variations of commercial aircraft. The development of such large structures are constrained by the manufacturing capabilities, and newer additive manufacturing technologies will contribute heavily for the future designs of aircraft.

Robotic Automated Fiber Placement (RAFP) is an advanced additive manufacturing modality using robotic arms to manufacture structural panels made out of carbon fiber reinforced polymer(CFRP). Traditionally, manufacture of laminated composites using resin pre-impregnated tows involved manual hand lay-up of each ply. This process is not only cumbersome but time consuming and inefficient and causes larger amount of scrap, making the end product less *"green"*. There is evidently no repeatability of parts (*i.e.,* accuracy in placing of the material) in the case of hand lay-up.

RAFP has been increasingly used to produce large aircraft parts and has revolutionized industrial production by providing a faster, cheaper alternative to manufacture CFRP parts. It has significant advantages over traditional hand lay-up to manufacture composite parts with varying large contours. Once programmed, a single machine can produce these large parts much faster, and being an additive manufacturing modality means the process would involve much less scrap material. It has also opened the possibility to now steer the fiber paths to manufacture variable stiffness composite parts with curvilinear fibers that can optimize critical structural perfor-

mance indices.

1.1 RAFP Manufacturing

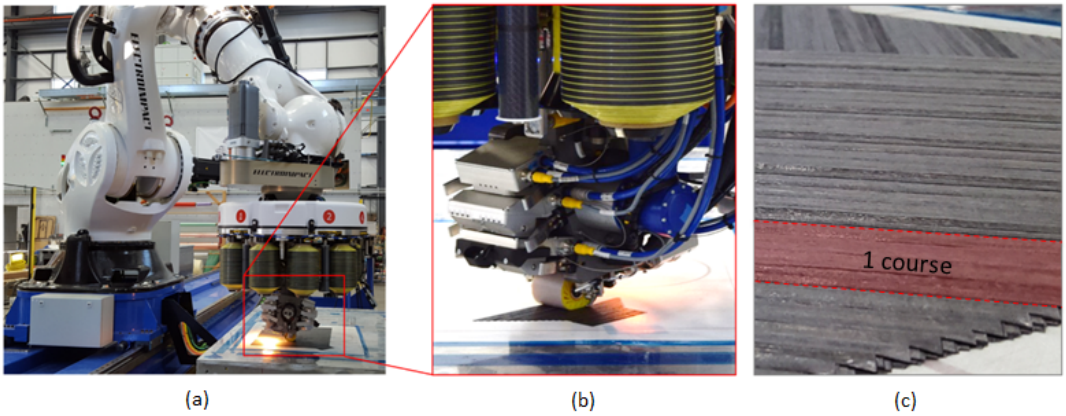

Figure 1.1: (a) An Electroimpact AFP Machine (b) Fiber Placement head of an Electroimpact machine showing roller head and spools of RAFP compliant pre-preg slit tapes (c) Process of lay-up

RAFP technology has helped create an alternative manufacturing process for precise, cheap, large structural parts for aircrafts- including wings, spars and fuselage, all with varying sizes and complexity of part geometry.

RAFP machines are robotic heads loaded with spools of carbon fiber tapes impregnated with resin material ("slit tapes") that are concurrently fed into a roller that lays down the material on a tool surface- either an aluminum caul plate or a mylar sheet, as shown in Figure 1.1(a-b). The fiber placement heads can be on a robotic arm or mounted on a vertical axis gantry or a horizontal axis gantry. This is chosen based on the part geometry, contour and size. RAFP manufacturers offer either fixed heads that cannot be replaced while in production, or newer modular heads, where the spools are mounted within the head of the machine which can be replaced during manufacturing.

1.1.1 Terminology and available options

Slit tapes used in RAFP are generally bundles of fibers that are supplied as spools or "tows" of resin pre-impregnated fibers. The modular head of the machine can be loaded with 8 to 32 spools of slit tapes to lay up multiple strips or "courses" of material, varying from 1 in to 4 in wide. The slit tapes are generally 1/8 in, 1/4 in or 1/2 in wide. Tow width and number of tows in a single course are significant manufacturing parameters and will directly influence gaps and overlaps. Thus, within a single course of width $1in$ to $4in$, one cam have tapes of different widths. Figure 1.1(c) shows a typical course and the slit tapes. Notice that there are gaps between individual courses. These parameters and layup speed also influence the minimum steering radius while manufacturing. This matters more when the designs involve steered fiber paths with constantly changing curvature.

1.1.2 Steering study

Minimum steering radius, as explained earlier is an important manufacturing constraint to be included for curved fiber designs as any derived optimal steered path shall now be restricted to this constraint in the design space. Thus, a steering study was conducted. Panels of orientation $[90/C]_S$, of size 18 in $\times$24 in were manufactured, where 90^o is in the direction along the horizontal axis Y in the Figure 1.2 and the lamina design C were simple curves of steering radius 100 in or 75 in or 50 in. For the operating speeds of the machine, a minimum radius of curvature constraint of 50 in is assumed for this work which would cause no tow pullover or wrinkling.

1.1.3 Un-tensioned area during lay- up

While designing fiber paths for a steered fiber study, one must be aware of programming the RAFP machine. While some machines allow cut and restart of tows while laying up, the particular machine that was used for this study has an approx-

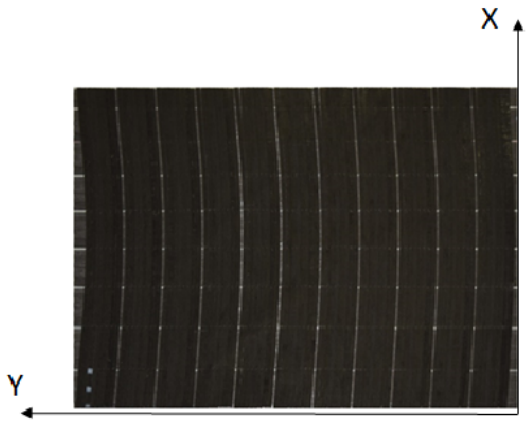

Figure 1.2: Curvature study Panel $[90/C]_S$ with radius of curvature 100 in

imately 4 in region of un-tensioned fibers at the beginning and end of laying each course. As seen in Figure 1.1(a-b), spools of pre-preg slit tapes are fed into a roller head which in turn lays the material down on a tooling surface or plies that were previously laid . The blades that cut the feed of slit-tapes at the end of each course are at a distance of approximately 4 in (Figure 1.3) and thus, this portion of the material has no control on the course as the tension in the tapes are lost. Similarly, when the next course is laid up there would be a region of no or less tension on the tapes as the part that is already laid has to get tacky to provide required adhesiveness.

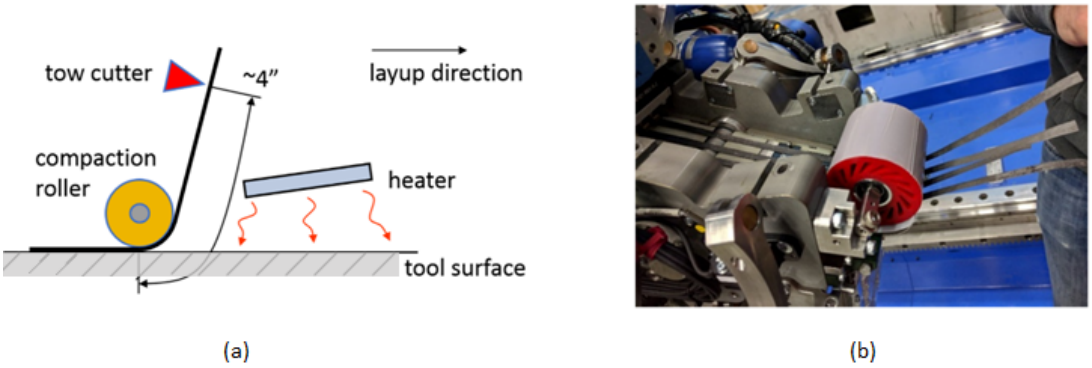

Figure 1.3: (a) Schematic of untensioned area at the initial and final 4 inches of a course layup (b) Opened lay-up head

1.2 Unique contributions and Organization of the Thesis

The unique contributions of this thesis are as follows:

- A novel method to represent center lines of fiber courses using parametric curves referred to as Bézier splines. The use of parametric curves provides the flexibility in modeling non- traditional, steered fiber paths while explicitly ensuring the continuity of these fiber paths.

- Each course is modeled individually and is allowed to spatially vary independent of the adjacent courses. Manufacturing parameters such as course width and minimum radius of curvature is explicitly included in the computations.

- A concept of *'global manufacturing mesh'* is introduced, that helps to reduce the number of optimization variables, while independently model each course path. It also ensures that, irrespective of the width of the course used- which will change the number of courses in each design, the number of optimization variables remain the same.

- The use of Bézier control points along with global manufacturing mesh ensures that adjacent courses do not completely overlap or create wide gaps.

- Explicitly including the creation of manufacturing signatures (MS) due to independently varying fiber paths and incorporating the microstructural changes caused due to MS on the mechanical response of the structures. This in particular, has not been addressed in the prior literature so as to illustrate the effect of MS on structural performance.

- Optimal fiber paths for specific structural performance indies have been developed in this work. A surrogate model in conjunction with a global optimizer (like Genetic Algorithm) is used to obtain optimal solutions. The use of surrogate models reduces the computational time significantly.

This thesis is arranged as follows. Chapter II introduces a brief literature review on the history and current status of research on variable stiffness panels. Chapter III introduces the problem of optimization of steered fiber paths for maximizing uni-axial and bi-axial in-plane compressive loads. It explains the use of parametrized curves for steered fiber paths with a detailed explanation on the concept of manufacturing mesh and the inclusion of manufacturing parameters and constraints. Chapter IV details the manufacturing of optimized panels for uni-axial tension and both non-destructive inspection and in-plane compressive tests of these panels. Chapter V introduces the numerical modeling of the experiments and modifications to the boundary conditions to simulate the laboratory test results. Chapter VI discusses the optimization problem for minimizing the stress concentration around an elliptical cutout in a rectangular flat panel. Conclusions and future research directions are discussed in chapter VII. In addition, two appendices are included. Appendix A explains the mathematical formulations of the pre-buckling and buckling equations of a generalized laminated flat plate. Appendix B introduces a new class of laminates called Double- Double (DD) which has promising structural performance. Three lay-up cases including DD is studied for optimal uiaxial and biaxial in-plane compression and it is established that DD laminates have significantly superior performance than traditional quasi-isotropic laminates. A comparison on response analysis of *thin* and *thick* unsymmetric DD laminates is also presented.

CHAPTER II

Review of Current Literature on Steered Fiber Paths in Laminated Aerostructural Parts

Initial research on the use of steered fibers or curvilinear fibers for the optimization of structural performance by distributing stiffness effectively was proposed by *Hyer and Lee* (1991) and, *Hyer and Charette* (1991) for improved buckling resistance of flat plates with a circular hole. Their work used discrete patches/regions of the structure to be optimized for discontinuous, discrete fiber angles in a 16 ply symmetric panel with four $\pm 45^o$ and twelve discrete angle layers that was able to provide 126% increase in buckling load compared to a baseline quasi isotropic laminate. These studies from early 1990's were conducted much before automated technologies for composites manufacturing like Automated tape laying (ATL) or Robotic Automated Fiber Placement (RAFP) were introduced and thus did not consider actual parameters or constraints for realization of the actual product. Thus, these theoretical designs were not manufactured or verified through experimental studies.

The commonly used nomenclature as variable stiffness panels (VSP) was introduced by Gurdal et.al in *Gurdal and Olmedo* (1992) and later in *Gurdal and Olmedo* (1993). This work provided a numerical platform for the analysis of composite laminates made of steered fibers and proposed a discretization method that would ensure

fiber continuity. This work was extended to include stability analysis of variable stiffness panels by *Olmedo and Gurdal* (1993). Numerical solutions using Rayleigh- Ritz method were presented in this work and reestablished that steered fibers produce higher buckling performance than straight fibers. A more generalized formulation to have one discrete fiber path as a reference curve and then shift the paths was introduced by *Waldhart et al.* (1996). The reference path could be shifted either by creating parallel curves to cover the design space, or it could be shifted laterally until the space is covered. Constraints on radius of curvature of these steered paths were also proposed in this work. It is to be noted that these initial studies did not consider optimization of VSP, but rather introduce the concept, and methods of analysis for solving the associated elliptical partial differential equations with variable coefficients. *Nagendra et al.* (1995) used an approach similar to Hyer et.al using discrete regions, combined with the use of non-uniform rational B-Splines (NURBS) interpolating through control points to derive optimal angles to tailor fiber paths.

Some of the studies presented also used lamination parameters as a mode for deriving fiber paths. Parametrization using lamination parameters was first introduced by *Tsai and Hahn* (1980). This was particularly useful in representing straight fiber angles in optimization studies prior to the concept of VSP [*Fukunaga and Vanderplaats* (1991) , *Fukunaga and Sekine* (1993), *Fukunaga et al.* (1994), *Grenestedt* (1991) and *Grenestedt and Gudmundson* (1993)]. The study by *Hammer et al.* (1997) extended the idea of lamination parameters to include local optimization of discrete angles in variable stiffness panels by iterative use of a finite element based solver in conjunction with a global optimizer. Both in-plane and out-of-plane load cases were studied and optimal fiber paths were proposed, though, such a design did not ensure fiber continuity. This work was later extended by *Setoodeh et al.* (2006a) and *Setoodeh et al.* (2006b) to obtain partially continuous tows by requiring an additional

post-processing step to retrieve the exact fiber paths. These studies too did not include the manufacturing parameters with respect to RAFP or ATL manufacturing. Further, *Crothers et al.* (1997), proposed a tailored fiber placement to derive optimal fiber paths for a flat plate with a cutout under tension using FE based Computer Aided Internal Optimization (CAIO).

The introduction of Tow Placement System (TPS) as a precursor to RAFP had more of the above works being implemented including some manufacturing parameters. *Gürdal and Tatting* (1998) first proposed including manufacturing considerations in optimization of *"Tow-placed"* VSP. This study was followed up by *Tatting and Gurdal* (2002) and *Gurdal et al.* (2005), which discussed the design and manufacture of *"Elastically Tailored"* tow placed plates including manufacturing parameters like radius of curvature as constraints, and artifacts including tow drop and overlap due to shifting of reference curves as proposed earlier. The presence of thickness variations due to tow drops and tow overlaps was also elucidated in this work. *Jegley et al.* (2003) and *Tatting and Gurdal* (2003) introduced a formal analysis tool for VSP using Finite Element Analysis (FEA) and included optimization studies to establish the benefits of fiber steering on improving the buckling loads of flat plates and, plates with holes under in-plane compression and shear loading. The initial reference path parametrization proposed in *Waldhart et al.* (1996) was used for representing the fiber paths including shifting of paths to have no overlaps or gaps. These studies were followed up experimental verification in *Wu and Gurdal* (2001), *Wu et al.* (2002). These panels had applied mechanical pre-stress to flatten out the initial curvature. Experimental testing of these panels showed upto 260% increase in transition loads compared to baseline crossply laminates of the same thickness; and this was attributed to the significant presence of overlaps causing a 120% increase in the total mass of the structure. However, the effects of overlaps were not captured

in the numerical models that were used to predict the transition loads. *Abdalla et al.* (2006), *Gürdal et al.* (2008) and *Setoodeh et al.* (2009) further established the superiority of variable stiffness panels for improved buckling performance under in plane compressive loads. The designs proposed by *Setoodeh et al.* (2009) showed upto 66% increase in buckling loads, though the theoretical designs were not manufacturable due to discontinuity of fiber paths.

First ply failure and progressive failure of tow steered variable stiffness panels were first studied by *Groenwold and Haftka* (2006), *Lopes et al.* (2007) and *Lopes et al.* (2008), showing marked improvements when compared to traditional straight fiber laminates. These studies established that the laminates with curvilinear fiber paths, especially the ones with overlaps delay the damage initiation and provides higher strength by around 50% when compared to straight fiber laminates. Application of tow steering in the manufacture of conical and cylindrical shells were introduced by *Blom et al.* (2006), *Wu* (2008), *Wu et al.* (2009) and *Khani et al.* (2015). These designs were modeled as continuous fiber paths in the shell circumferential direction, similar to the reference path definition for a flat plate proposed in *Waldhart et al.* (1996). This was followed by optimization studies on such structures in *Blom et al.* (2007). *Blom et al.* (2008) and *Blom et al.* (2010) identified that thickness build up in tow steered conical shells are not unique and depends on the starting point the placement machine. A theoretical model to study the effect of tow dropping while manufacturing on the stiffness and failure strength of a VSP was proposed by *Blom et al.* (2009). Experimental studies on buckling performance of tow steered composite cylindrical shells were presented in *Wu et al.* (2013a) and *White et al.* (2015). Two cylindrical shells with curvilinear paths were studied, one with fiver course overlaps and one with minimal overlaps of gaps. The former designs showed 62% higher axial stiffness, and 78% higher normalized transition load than the latter, which further

established that the overlaps created by adjacent courses improve buckling performance. The only drawback here was that the shell with overlaps was 27% heavier than the one without defects.

Further use of lamination parameters for optimization was proposed by *IJsselmuiden et al.* (2010) for maximizing the buckling loads under in-plane compression for flat variable stiffness panels. The major drawback being the inability to realize the fiber paths in a lamination parameter space. This work was further extended by *Khani et al.* (2011) to study optimal designs that shall maximize the strength using Tsai-Wu failure envelopes. This study established that incorporating failure criteria in the lamination parameter space was difficult due the dependency on fiber angles. A review of optimization strategies for constant stiffness and variable stiffness panels using lamination parameters are provided in the article by *Ghiasi et al.* (2010) and *Albazzan et al.* (2019). *Demir et al.* (2019) incorporated fiber steering constraints with in the optimization framework by using lamination parameters and enforced fiber continuity to some extent. In general, use of lamination parameters within discrete patches have provided fiber paths that are either not manufacturable, or at times even non-unique. Another method for parametrization of fiber paths is by using the level-set method as introduced by *Shirinzadeh et al.* (2007). Such an algorithm is robust in the sense that it ensures continuity of fiber paths as a contour/ level-set derived from a surface in space shall not be discontinuous. By utilizing this advantage a few more studies investigated the use of level-set methods as described in *Bruyneel and Zein* (2011), *Bruyneel and Zein* (2013) and *Brampton and Kim* (2013). Though the algorithm ensures continuity, it is difficult to implement manufacturing constraints like minimum radius of curvature in designs derived using level-sets.

Later works started identifying manufacturability and incorporation of manufac-

turing parameters and constraints to be imperative within the optimization framework. *Lopes et al.* (2010) studied the steering of composite fiber tows to tailor the strength in plate with cutouts under in-plane loads, rendering the buckling loads and first ply failure insensitive to the presence of a cutout. The representation of fiber paths for this study used the previously proposed reference curve and shifting method by *Gurdal and Olmedo* (1993) and, *Waldhart et al.* (1996), but incorporated tow cutting and restart to eliminate any overlaps there by avoiding any thickness build up. Even though such designs avoids the formation of large gaps by ensuring full coverage, cut- restart method creates small pockets of wedge-gaps which will be filled with the resin material during curing. *Fayazbakhsh et al.* (2013) presented the idea of a defect-layer method for analysis of laminates with gaps or overlaps. This involved adding a *'defect layer'* in the ply stack-up to incorporate the presence of gaps and overlaps in steered fiber panels. Minimal variations in thickness was enforced by using cut and restart of the fiber placement head which would cause local wedges of either resin-rich gaps or overlaps. An automated framework was developed to identify these locations and introduce a *"defect-layer"* in the lay-up of plies within the FE model to incorporate the effect of defects.

Nik et al. (2014) presented an extension of this work using an optimization framework to include the presence of these manufacturing artifacts in steered fibers by presenting one sided or two sided cut and restart. This study also included designs that either had only gaps or only gaps and analyzed the effect of the presence of these defective areas on the buckling load and in-plane stiffness of a flat panel. This study was followed up by *Marouene et al.* (2016a) which presented an experimental investigation on the buckling behavior of such optimized VSP under in-plane compression. It was established that manufacturable panels derived from ideal pristine solutions, by either incorporating an all gap or an all overlap strategy by tow cut and restarting

still shows significant improvement in buckling loads compared to a traditional quasi-isotropic laminate. A comprehensive summary of analytical and experimental studies on buckling behavior of manufactured fiver- steered panels is presented in *Marouene et al.* (2016b)

The study by *van Tooren et al.* (2015) and *Van Tooren et al.* (2016) introduced the idea of a manufacturing mesh to realize optimization variables which has been modified and adopted in this thesis. A coarse manufacturing mesh unrelated to a Finite Element mesh is first established, with the nodal values being fiber angles. These nodal values then become the optimization variable. This method requires an additional post processing step to visualize the fiber paths. As an illustration, a variable stiffness panel with multiple cutouts loaded in in-plane tension is designed to maximize the failure strength, imposing curvature constraints within the optimization framework. The effect of gaps and overlaps in such designs were proposed as stiffness corrections in *Lucas et al.* (2017). A follow up study by *Khani et al.* (2017) experimentally verified the results and established that steering the fiber paths results in a non localized failure that spreads across the panel instead of being concentrated at the edges of the cutouts. The idea of Manufacturing Mesh was further extended for curved shells in *van Zanten et al.* (2019).

Further studies on the post buckling behavior of VS panels and methods to analyze the buckling, post-buckling and thermal behavior of such structures were presented in *Raju et al.* (2012), *White et al.* (2015), *Wu et al.* (2012) and *Raju et al.* (2013). Some of these initial studies considered pristine optimal paths without the inclusion of manufacturing parameters or manufacturing induced defects. A parallel nomenclature of Variable Angle Tow (VAT) was introduced in these studies, and the initial experimental work included manufacturing using continuous tow shearing method

which is similar to RAFP, but differ in the fact that this uses dry tows in place of pre-preg spools [*Kim et al.* (2012a), *Kim et al.* (2012b) and *Kim et al.* (2014)]. These studies also established the presence of inherent defects in these additive manufacturing modalities, and established the exacerbation of defects due to steering and curvature [*Kim et al.* (2012a) and *Kim et al.* (2014)]. An optimization framework including post-buckling stiffness as an objective was introduced by *Wu et al.* (2013b) and *Wu et al.* (2015), though discrete fiber orientations in this study did not explicitly ensure fiber continuity and there by lacked manufacturability. These were extended to incorporate fiber continuity by *Kim et al.* (2015) using computer aided modeling to derive manufacturable paths from discrete optimal fiber angles.

The use of tow steered panels in morphing structures was studied in *Panesar and Weaver* and *Panesar and Weaver* (2012) for optimizing the out of plane displacement and maximizing the angle of attack of a wing flap. This was done by utilizing the thermally induced bi-stable behavior in specific tow steered laminates [*Panesar et al.* (2012)]. Buckling, post-buckling and failure of VAT/VSP panels under in-plane shear loading were studied by *Raju et al.* (2015), *Madeo et al.* (2017) and *Gomes et al.* (2014). These post buckling analysis methods were included in an optimization framework by *Raju et al.* (2018) and *Wu et al.* (2018) using a multi-level optimization approach. These methods were further extended to the buckling and post buckling analysis of stiffened, tow steered variable stiffness panels in *Coburn et al.* (2014) and *Telford et al.* (2018). A practical application of VSP was studied in the optimization of a composite wing box for optimal post buckling stiffness in *Liguori et al.* (2019) which was followed up by experimental investigation by *Oliveri et al.* (2019) and *Zucco et al.* (2020). A FE model set-up to predict the behavior of these composite wing boxes was also presented which was able to accurately predict the most critical areas for material failure. The experiments also established that in the buckling-driven

designs for VAT, buckling occurs prior to material failure, as anticipated. A similar study on buckling and post buckling of a variable stiffness composite wing box was conducted by *Wang et al.* (2018).

A design tool to realize such steered fiber paths for a flat panel with cutouts was introduced by *Zucco et al.* (2021) which also identifies the varying thickness profile due to the presence of overlaps and gaps. Further, a theoretical model for an *"imperfection insensitive"* cylinder using steered fiber paths manufactured using CTS was proposed recently in the works of *Lincoln et al.* (2021). An extensive review of the literature on VSP/ VAT/ tow- steered laminates is presented in *Aragh et al.* (2021), providing manufacturable insights into the modeling and design of such structures.

Composite laminate optimization for VSP using RAFP may involve a significantly higher number of optimization variables, and with the current emphasis on data science, many researchers have used Surrogate modeling (meta-modeling) approaches. Global optimization techniques like Genetic algorithm (GA) might require few thousands of evaluations of the designs which will make the task of finding optimal solutions extremely time expensive. The idea of meta-modeling is to use a large set of data (objective function) calculated at sampled points in the design space using suitable sampling methodologies like Latin Hypercube Sampling (LHS) or Sobol. This data is then used to create computationally inexpensive low fidelity functions that can converge faster to an optimal solution *Wang and Shan* (2007). *Blom et al.* (2010) utilized surrogate modeling for optimal VS cylinders using Design Explorer. *Rouhi et al.* (2014) and *Rouhi et al.* (2015) used a radial basis function (RBF) based surrogate model to analyze the bending induced buckling performance of VS cylinders. In past studies, the author of the current work has proposed the use of Artificial Neural Networks (ANNs) combined with an optimization algorithm for minimizing stress

concentrations [*Vijayachandran et al.* (2017)] and maximizing buckling performance [*Vijayachandran et al.* (2019), *Vijayachandran et al.* (2020a) and *Vijayachandran et al.* (2020b)] The last three publications has been incorporated in chapter 3 of this thesis.

A detailed study on the effect of defects in RAFP manufacturing is discussed in *Nguyen et al.* (2019a) and *Nguyen et al.* (2019b). This work identified that gaps between adjacent courses and overlap of adjacent courses are significant defects that contribute to reduction in stiffness and strength of the final part. There is also varying effect of the location and size of these defects. Together, these two common defects in RAFP manufacturing are called Manufacturing Signature (MS) of the machine.

In this thesis, a clear distinction is made by introducing a novel method to represent individual fiber paths using Bézier splines. In doing so, each course can be individually modeled, and manufacturing parameters like course width and minimum radius of curvature can be explicitly included. This also helps in identifying gaps between and overlap of adjacent courses. Further, a scheme using the concept of manufacturing mesh to reduce the number of optimization variables by creating locus curves for the control points of these Bézier splines and, a surrogate modeling technique based on Artificial Neural Networks (ANN) or Radial Basis Function (RBF) in conjunction with genetic algorithm GA) for global optimization is introduced.

CHAPTER III

Optimization of Steered Fiber Paths for In-plane Compressive Loading

Compressive response and buckling are critical design indices in aircraft design. While in flight, the top skin of the wing is in compression while internal ribs and spars are subjected to shear loading. An advantage of steering fiber paths to distribute stiffness could be to improve the compressive response of aircraft structures with no or minimal increase in structural mass. As discussed previously, while, many researchers proposed designs to optimize critical structural performance indices like buckling load, most of the initial studies did not account for the manufacturing signature(MS)[*Nguyen et al.* (2019a),*Nguyen et al.* (2019b)] of steering fibers using RAFP or CTS as these technologies were still under development. As described earlier, the MS accounts for real deviation from the intended microstructure of a RAFP manufactured part. Hence, proper accounting for the MS in computing buckling loads, for example, is a novel contribution in this thesis.

This study investigates the optimization of steered fiber paths to maximize the critical buckling loads for a 20 in $\times$20 in square, laminated composite plate under uni-axial and bi-axial in-plane compression. Additional constraints on gain in total structural mass and loss of in-plane stiffness is also incorporated. A novel methodol-

ogy is introduced here to represent the fiber path by which manufacturing parameters such as course width and constraints like fiber continuity and radius of curvature shall be explicitly incorporated. A pixelated FE mesh is introduced for the in-plane buckling analysis that identifies the manufacturing signatures like gaps and overlaps and associated changes in the geometry and incorporate those in the stiffness matrices.

3.1 Problem Statement

A flat square panel of size 20 in $\times$20 in is considered with applied in-plane compressive loads (Figure 3.1). As seen in the figure, two loading conditions are considered. Load case I where a uni-axial load is applied, and Load case II with a 2 : 1 bi-axial loading. The plate is simply supported on all the edges and Toray $T800/3900S$ material properties (Table 3.1) are considered. Courses of 4in RAFP tapes are used in the study with a nominal thickness of 0.0075 in as provided by the manufacturer. The fiber volume fractions are assumed to not change within the plate.

The aim of the study here is to obtain optimal, manufacturable fiber paths that are allowed to vary spatially so as to maximize the critical buckling load. Details of the manufacturing process such as gaps and overlaps are accounted for. The second objective here is also to ensure that the total mass compared to a 0° pristine UD four ply laminate is minimized.

A multi-objective global optimization is proposed for the problem. For loading case I, the objectives are to maximize the critical buckling load N_0, maximize the transverse global stiffness, K_Y, and minimize the total mass of the plate m. For loading case II, the objective is to maximize the critical buckling load N_0 and minimize the total mass of the plate m.

Table 3.1: Material Properties of T800/3900S

Property	Value	Unit
E_{11}	21.5	Msi
E_{22}	1.23	Msi
ν_{12}	0.329	
G_{12}	0.571	Msi

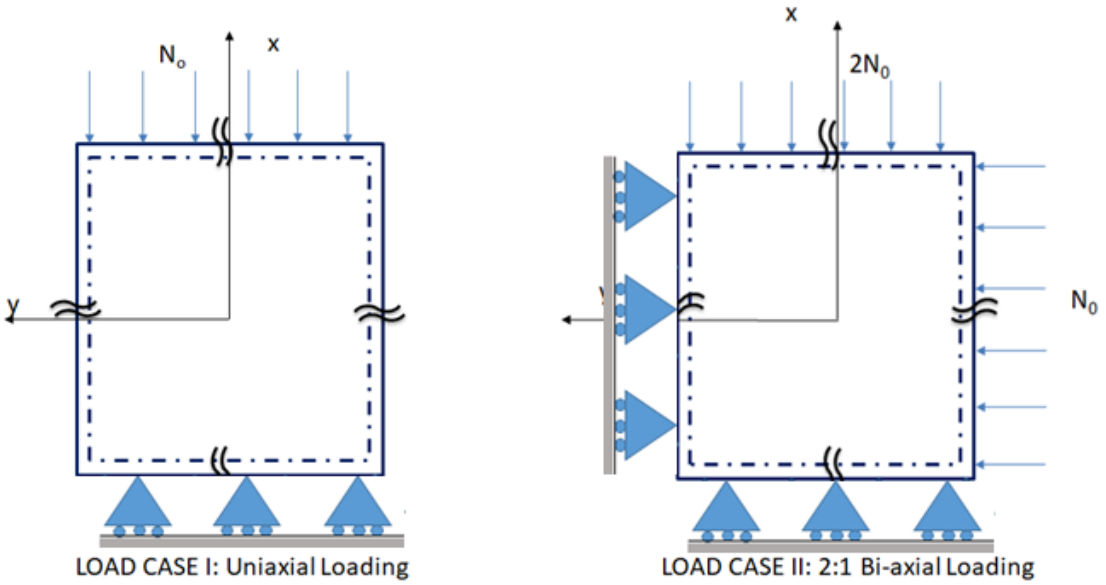

Figure 3.1: Loading and Boundary conditions

3.2 Modeling Fiber Paths

The trivial constraint in deriving the fiber paths is to ensure continuity- which means there are no abrupt cuts or jumps in the fiber path. Secondary constraints arise from the manufacturing process as mentioned earlier- inclusion of course width, minimum steering radius, accounting for unintended manufacturing signatures etc. Using a parametric function to represent the fiber paths imply that continuity is ensured. In this study, Bézier curves are used to define the centerlines of fiber tows. The general form of the curves is as shown.

$$B(n,t) = \Sigma_{i=0}^{n} \binom{n}{i} C_i (1-t)^{n-i} t^i, \ \forall \quad 0 \leq t \leq 1 \tag{3.1}$$

where $n = O + 1$. O is the order of the curve and C_i represents the co-ordinate of the i^{th} point on the curve. Specifically, cubic splines are used for modeling the fiber paths, and shall be expressed as,

$$x(t) = x_1(1-t)^3 + 3x_2t(1-t)^2 + 3x_3t^2(1-t) + x_4t^3, \ \forall \quad 0 \leq t \leq 1 \tag{3.2}$$

$$y(t) = y_1(1-t)^3 + 3y_2t(1-t)^2 + 3y_3t^2(1-t) + y_4t^3, \ \forall \quad 0 \leq t \leq 1 \tag{3.3}$$

where x_i and y_i $(i = 1, 2, 3, 4)$ are the co-ordinates of the control points.

3.2.1 Manufacturing Global Mesh

Cubic splines are used for modeling the fiber paths as it is the least degree polynomial with an inflection point. While using Bézier curves would ensure continuity, this means that 4 control points are necessary for each spline- which means there are 8 optimization variables (co-ordinates or weights of the control points) per course. Thus a *"global manufacturing mesh"* is proposed to introduce an interpolation scheme, whereby the control points of all splines lie on certain "locus curves", thus reducing the number of optimization variables. It is to be noted that the manufacturing mesh is independent of any structural calculations.

The interpolation scheme is used to change the "nodal shifts" at the nodes that would then move the control points from the "initial seed" locations, deriving new paths in doing so. The method is discussed in detail here. Firstly, to ensure a full coverage of the design space while iterating various designs, the steered fiber paths are designed for a larger panel (40 in $\times$40 in). The assumption here is that a larger part shall be built, and the required structural part could then be cut out from the

manufactured panel. In reality, only the physical part and the curves within the actual part dimensions matter. The lengths of the paths in excess is useful for the 4 inches of untensioned tows at the beginning and end of each pass of the machine as discussed in Chapter 1, and any additional length shall be ignored while programming the machine for lay-up.

A total of 10 courses, each of width 4 in is placed along vertical direction (in Figure 3.2) with no overlaps or gaps, ensuring full coverage of the panel. This is called an "initial seed" - means the Bézier control points for the splines representing the centerlines of each of the tapes are now collinear.

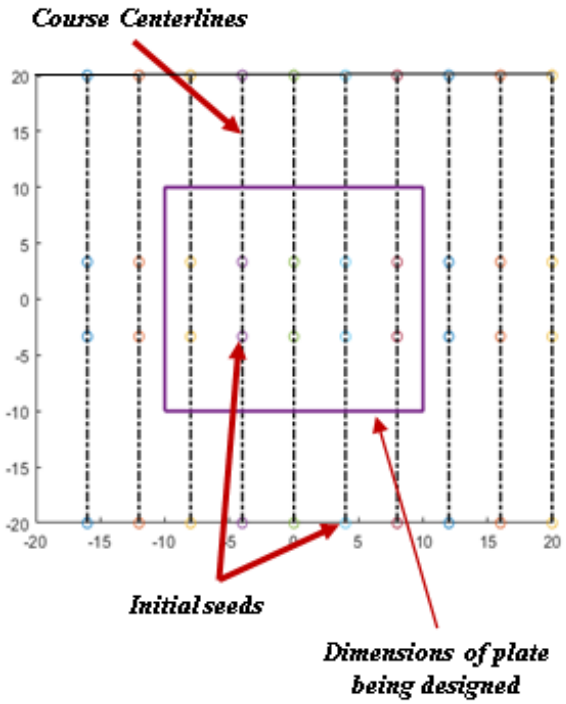

Figure 3.2: Centerlines of initial paths showing initial seeds

The nodal values of this manufacturing mesh are the nodal shift distances- δ_x and δ_y. These values of nodal shifts shall now become the optimization variables for

varying the design in each iteration. The values of nodal shifts shall be interpolated to the initial seeds and the coordinates of the seeds shall be moved to ($x_i + \Delta x_i$, $y_i + \Delta y_i$) to obtain the updated Bézier control points for the centerline of each course, where (x_i, y_i) are the initial co-ordinates of the seed 'i' and $\Delta(x_i, y_i)$ is the shift interpolated from the nodal values. The initial seeding points (shown for two courses in Figure 3.3) of all the cubic splines lie within the three elements and are collinear. The nodal variables at the manufacturing mesh nodes are then interpolated to the initial seed locations to get new designs in each iteration as explained. The machine is assumed to start and end at the bottom and top edges of the manufacturing mesh, thereby constraining the δ_y at these nodes to be zero. So the optimization variables are δ_x at nodes 1, 4, 5, 8 and both δ_x and δ_y at nodes 2, 3, 6, 7 as show in Figure 3.3. This means we have a total of 12 design variables per independent ply. Further, the manufacturing mesh can be rotated with respect to the $x - y$ co-ordinate system with an angle ϕ, thereby giving an additional optimization variable for steering the fiber angles. To summarize, for a 4-ply symmetric design, there are 26 optimization variables- 12 nodal variables and one angle of rotation per ply. An example of how the initial seeds are shifted to derive new steered fiber paths, is illustrated in Figure 3.4.

By using Bézier splines for parametrization combined with an interpolation scheme to align the control points on a controlled locus curve, multiple benefits are obtained. Firstly, the fiber paths are continuous by definition. Secondly, the control points of adjacent courses will not overlap or crossover, since they fall on a locus curve dictated by the linear interpolation within the manufacturing mesh element. Thus, the adjacent courses will always have a separation. Lastly, by defining the bounds of the nodal shifts, the amount of overlap or gap allowed in the design space shall be controlled.

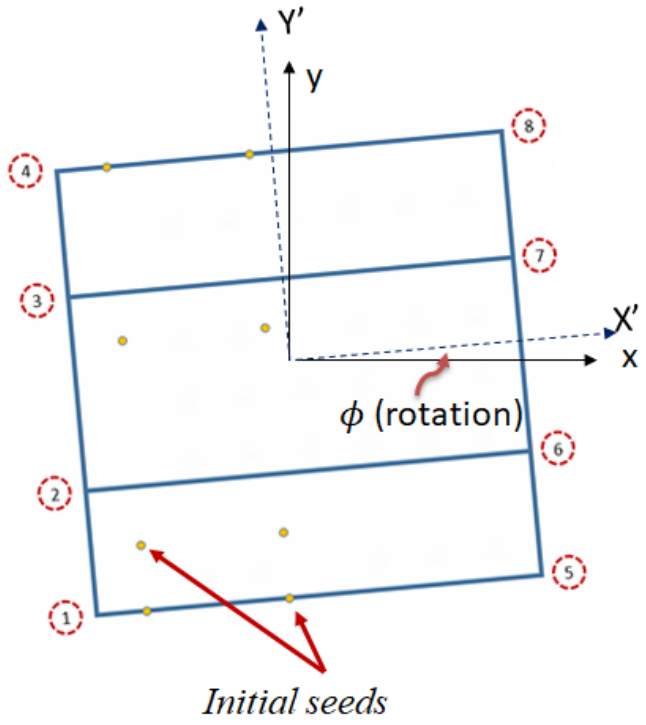

Figure 3.3: Initial seeds and Manufacturing global mesh

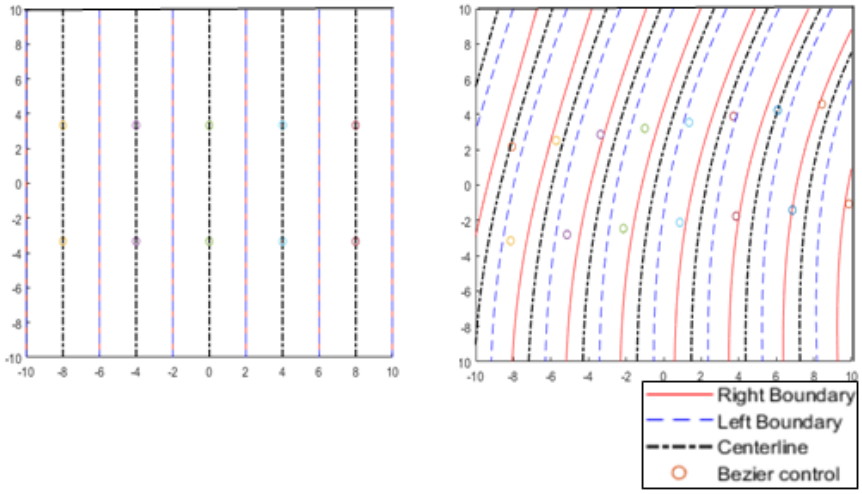

Figure 3.4: Varying steered fiber courses in a design

3.3 Mehanical Modeling

3.3.1 Finite element models using pixelated mesh

A python based code is written to create a grid of pixelated finite element mesh of composite shell type S4 elements in the commercial finite element software, Abaqus.

In the current model, a 200×200 grid is created, with 40401 nodes, with 3 translational and 2 rotational degrees of freedom at each node. The code has the capability to identify for each element on each independent ply in the stack, the courses that pass through the element centroid. Every element is thus assigned a laminate stack up. This algorithm is explained as follows.

For each independent ply in the stack, the optimizer provides nodal shifts and these are used to create Bézier splines to represent centerlines of each course. The normal direction at each point in the spline is calculated using analytical expressions, and the left and right course boundaries are generated by including a manufacturing parameter of 4 in width per course. A closed polygon is then created for each course, that comprises of the left and right course boundaries and the boundaries of the physical plate that it cuts through. These closed polygons are then overlaid on top of the physical design space under consideration. These closed polygons may overlap (creating the overlap locations), or have locations that are not covered by any of these polygons (creating gap locations), or barely touch at their respective boundaries (course butt joints). For each element, on each ply, the algorithm identifies if it lies within one or many of these closed polygons (corresponding to the respective courses), and if it identifies any of the courses, it is then added to the stacking sequence of that composite shell element. It is then assigned a thickness and an angle as explained below.

If at a given element centroid location, only one course is identified, then it is assigned the thickness of a single ply, for which a nominal 0.0075 in is used as provided by the manufacturer. If multiple courses are identified, each of them are assigned 91% thickness. This assumption is based on a previous study conducted on effects of gaps and overlaps on the mechanical strength of composite specimens [*Nguyen*

et al. (2019a),*Nguyen et al.* (2019b)], which established that thickness of overlap regions will not be multiples of the single ply thickness but a distribution that varies depending on factors such as ply location in the stacking, compaction pressure etc (Figure 3.5). Further, to assign the angle, the algorithm searches for the closest point in the centerline of the course(s) to the element centroid under consideration and provides the angle corresponding that point for each layer in the stack up.

The FEM model was verified for accuracy and convergence by comparing with the analytical solutions for specially orthotropic $[0]_4$, $[90]_4$ and $[0/90]_S$ layups. The model predicted the buckling loads for these cases within 2% accuracy.

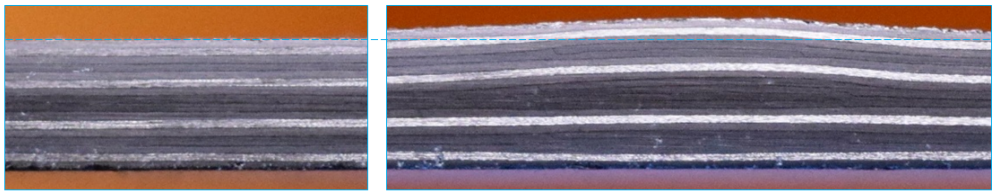

Figure 3.5: Typical thickness variation due to overlaps- (a) Pristine lyup with no overlaps (b) Locations with multiple aligned overlaps

3.3.2 Buckling Analysis

Figure 3.6 illustrates an infinitesimal area chosen from a RAFP plate and how the different layers are stacked up. The plate is modeled using the assumptions of Kirchhoff-Love plate theory. The force and moment resultants in the infinitesimal plate element are also illustrated. For each finite element, the corresponding stacking sequence at each centroid location (integration point) is obtained as explained in the above algorithm, and the constitutive relations between force and moment resultants (N and M), and the strains and curvatures (ϵ and χ) are computed using Classical

Lamination Theory (CLT). The stacking sequence is with respect to a global coordinate system that is aligned with the structure, therefore, this sequence changes from point to point within the plate, as a function of the fiber paths within each layer.

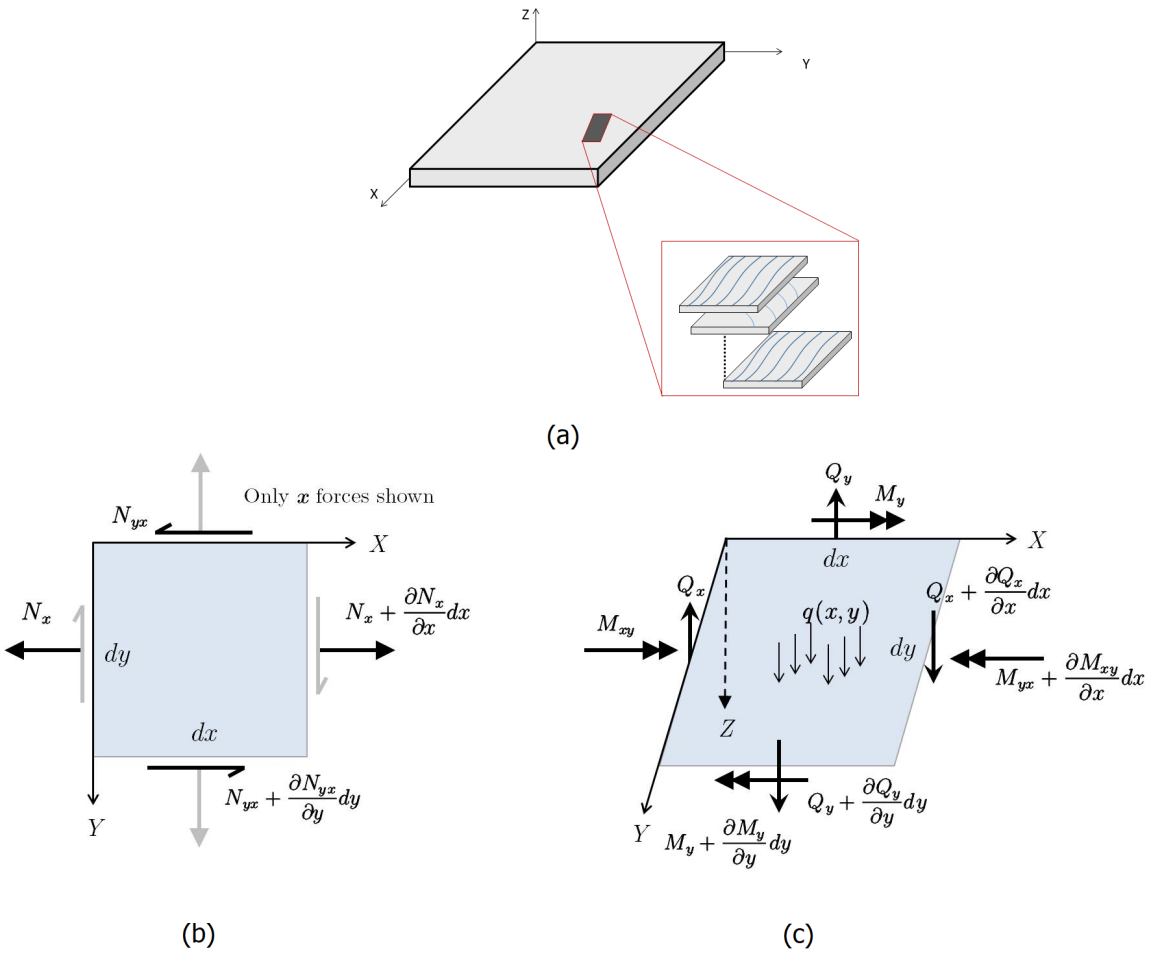

Figure 3.6: (a) Illustration showing an infinitesimally small area of the plate, (b) Force resultants and (c) Moment resultants *Reddy* (2003)

$$\begin{Bmatrix} N \\ M \end{Bmatrix} = \begin{bmatrix} A & B \\ B & D \end{bmatrix} \begin{Bmatrix} \epsilon^0 \\ \chi \end{Bmatrix} \tag{3.4}$$

where,

$$\begin{aligned} &A \text{ - Extensional stiffness matrix} \\ &B \text{ - Coupling (extensional-bending) stiffness matrix} \\ &D \text{ - Bending stiffness matrix} \end{aligned} \tag{3.5}$$

$$\begin{aligned} A_{ij} &= \sum_{k=1}^{n} \bar{Q}_{ij}^{k}(h_k - h_{k-1}) \\ B_{ij} &= \frac{1}{2}\sum_{k=1}^{n} \bar{Q}_{ij}^{k}(h_k^2 - h_{k-1}^2) \\ D_{ij} &= \frac{1}{3}\sum_{k=1}^{n} \bar{Q}_{ij}^{k}(h_k^3 - h_{k-1}^3) \end{aligned} \tag{3.6}$$

The geometrically nonlinear Von-Karman strains, ϵ and curvatures χ are,

$$\begin{aligned} \epsilon_x &= \frac{\partial u_0}{\partial x} - z\frac{\partial^2 w}{\partial x^2} + \frac{1}{2}\left(\frac{\partial w}{\partial x}\right)^2 \\ \epsilon_y &= \frac{\partial v_0}{\partial y} - z\frac{\partial^2 w}{\partial y^2} + \frac{1}{2}\left(\frac{\partial w}{\partial y}\right)^2 \\ \epsilon_{xy} &= \frac{\partial u_0}{\partial y} + \frac{\partial v_0}{\partial x} - 2z\frac{\partial^2 w}{\partial x \partial y} + \frac{\partial w}{\partial x}\frac{\partial w}{\partial y} \end{aligned} \tag{3.7}$$

$$\begin{Bmatrix} \chi_x \\ \chi_y \\ \chi_{xy} \end{Bmatrix} = \begin{Bmatrix} -\frac{\partial^2 w_0(x,y)}{\partial x^2} \\ -\frac{\partial^2 w_0(x,y)}{\partial y^2} \\ -2\frac{\partial^2 w_0(x,y)}{\partial x \ \partial y} \end{Bmatrix} \tag{3.8}$$

Assuming $[B] = 0$ for a symmetric layup, the bending and extensional stiffness contributes to the assembled stiffness matrices $[K]$ and $[G]$,where K is the global stiffness matrix and G is the geometric stiffness matrix due to the effect of membrane forces. The finite element procedure results in an eigenvalue problem of the form

$$\Big[K - \lambda_i G\Big]\,\Phi_i = 0 \tag{3.9}$$

Where, λ_i is the i^{th} eigen value and Φ_i is the corresponding eigen mode. For critical

buckling load, the lowest eigen value is sought.

3.4 Optimization Set-up and Surrogate Models

There are 13 optimization variables per independent ply as discussed before, thus the stacking of a four ply symmetric laminate would require 26 independent optimization variables. Since using GA to compute the fitness function in each iteration would be computationally expensive, a surrogate modeling technique is proposed.

3.4.1 Sampling and Artificial Neural Network Model

Latin Hypercube Sampling, a stratified sampling technique is used to create 4200 distributed samples to span the entire design space. For this, an initial sampling is done on a linear $[0, 1]^{26}$ space and then each optimization variable (each row of the sampled initial $[X(4200, 26)]$ matrix) is mapped one on one to its design limits using a linear map with the corresponding upper and lower bounds. MATLAB ®is used for surrogate modeling. It has a machine learning and deep learning toolbox with an efficient GUI based application for using Artificial Neural Networks (ANNs).

These 4200 samples are then used to evaluate the objective functions in each case. The corresponding output matrices Y (critical buckling load, mass and global transverse stiffness) are obtained using the aforementioned FE model. The samples and the output matrices are the inputs for the MATLAB ®application. 70% data is used for training, 15% for validation and 15% for testing. 10 hidden layers are used and a Bayesian Regularization algorithm which is inbuilt in the ANN application is used for training the dataset.

3.4.2 Case I

Once the samples are created and mapped to the physical design space, the pixelated FEA code detailed above is used to calculate the buckling load N_0, total mass m and transverse global stiffness K_Y for each design. An output matrix $Y[4200, 3]$ is then populated using these outputs [*Wang and Shan* (2007)]. Then ANN fitting on the MATLAB ®toolbox is used to create a surrogate model for the data set relating the inputs [X] to the outputs [Y]. A flow chart of the optimization- surrogate modeling technique for Case I is described in Figure 3.7. Multi-objective Genetic Algorithm (GA) is then applied on the meta model to obtain a Pareto front of feasible solutions. The designs that maximizes buckling load among these feasible solutions are chosen by applying the condition that mass gain, $\Delta m \leq 10\%$, and gain in transverse stiffness, $\Delta K_Y \leq 10\%$ when compared to that of a 0° UD laminate of four plies.

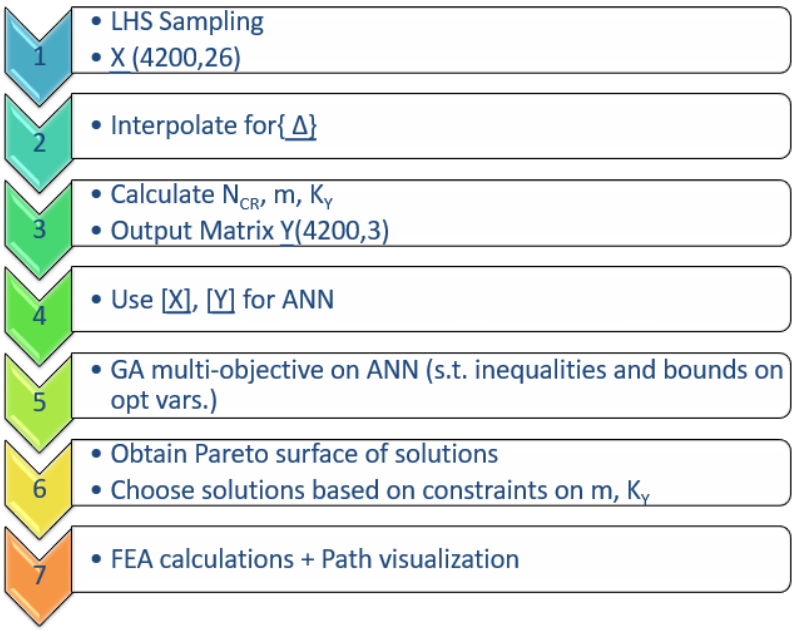

Figure 3.7: Flowchart for optimization methodology using surrogate model (ANN) and global optimization module for case I

3.4.3 Case II

Following the case I explained above, once the 4200 samples in the physical design space are created and mapped, the FEA model is run iteratively to populate an output matrix $Y[4200, 2]$ of critical buckling loads and total mass for each of the samples[*Wang and Shan* (2007)]. The ANN fitting application from Matlab ®toolbox is used to create a metamodel. Multi-objective Genetic Algorithm (GA) is then applied on the meta model to obtain a Pareto front of feasible solutions and the best among them are chosen by considering a constraint on mass gain, $\Delta m \leq 10\%$. The regression values (Figure 3.8.) demonstrates a good fit for both the objectives using ANN for case II samples (see Figure 3.9).

3.4.4 Fitness Function

Mathematical representation of the optimization problems are as follows.
For case I,

$$\begin{aligned} \min_{X} \quad & (-N_{CR}, -K_Y, m) \\ \text{subject to} \quad & X_L \leq X \leq X_U \end{aligned}$$

For case II

$$\begin{aligned} \min_{X} \quad & (-N_{CR}, m) \\ \text{subject to} \quad & X_L \leq X \leq X_U \end{aligned}$$

where N_{CR} is the critical buckling load , K_Y is the transverse global stiffness, m is the total mass of the panel and, x_L and x_U are the bounds of the design space.

3.5 Results

Multi-objective genetic algorithm functionality of Matlab ®optimization toolbox was utilized to run the optimization problem on the surrogate model. In general, for both the loading cases, a Pareto front of feasible solutions is obtained (Figures 3.10, 3.14). The most feasible among the optimal solutions are then picked from the Pareto front by applying constraints on mass m and/or K_Y.

3.5.1 Loading Case I

Three designs were identified from the Pareto surface by applying the constraints $\Delta m \leq 10\%$. Note that in loading case I, an additional constraint $\Delta K_Y \leq 10\%$, is also applied on the Pareto surface to choose the feasible solutions.

3.5.1.1 Design 1

The first design chosen from the Pareto front shows a 42% increase in critical buckling load with a total increase in the mass of only 9.5% and increase in K_Y by 7%. The increase in mass is contributed in part by the creation of overlaps between adjacent courses and also due to more length of each course within the plate, which happens due to steering on a curved path as opposed to straight UD, 0°, fibers. However, these overlap regions are potentially useful in raising the buckling load due to local stiffening. Table 3.2 details the design indicators of Design 1 compared to the benchmark problem. Explicit fiber paths, thickness profile and critical buckling mode are shown in Figure 3.11.

Table 3.2: Design indicators for Design 1

	Steered	0°	%increase
N_0(lb/in)	0.8129	0.5709	42%
$P_0(lb)$	16.26	11.42	42%
m	0.6265	0.5720	9.5%
K_Y	3.3x10^4	3.08x10^4	7%

Table 3.3: Design indicators for Design 2

	Steered	0°	%increase
N_0(lb/in)	0.7820	0.5709	37%
$P_0(lb)$	15.64	11.42	37%
m	0.6347	0.5720	10%
K_Y	3.34x10^4	3.08x10^4	8%

3.5.1.2 Design 2

The next design shows a 37% increase in critical buckling load with a total increase in the mass of 10% and increase in K_Y by 8%. Table 3.3 details the design indicators of Design 2 compared to the benchmark problem. Explicit fiber paths, thickness profile and critical buckling mode are shown in Figure 3.12.

3.5.1.3 Design 3

The next design shows a 36% increase in critical buckling load with a total increase in the mass of 9% and increase in K_Y by 6%. Table 3.4 details the design indicators of Design 2 compared to the benchmark problem. Explicit fiber paths, thickness profile and critical buckling mode are shown in Figure 3.13.

Table 3.4: Design indicators for Design 3

	Steered	0°	%increase
N_0(lb/in)	0.7768	0.5709	36%
$P_0(lb)$	15.64	11.42	37%
m	0.6245	0.5720	9%
K_Y	3.29x10^4	3.08x10^4	6%

Table 3.5: Design indicators for Design 1

	Steered	0°	%increase
N_0(lb/in)	0.2638	0.194	36%
$P_0(lb)$	5.27	3.88	36%
m	0.6063	0.5720	6%

3.5.2 Loading Case II

Three designs were identified from the Pareto surface by applying the constraints $\Delta m \leq 10\%$, alone. In case of bi-axial loading, transverse stiffness was not considered as a parameter as it was expected to have higher transverse stiffness due to some plies having orientations not aligned to a single loading direction along the X- axis.

3.5.2.1 Design 1

The first design chosen from the Pareto front shows a 36% increase in critical buckling load with a total increase in the mass of only 6%. Table 3.5 details the design indicators of Design 1 compared to the benchmark problem. Explicit fiber paths, thickness profile and critical buckling mode are shown in Figure 3.15.

3.5.2.2 Design 2

The next design shows a 37% increase in critical buckling load with a total increase in the mass of only 5%. Table 3.6 details the design indicators of Design 2 compared to the benchmark problem. Explicit fiber paths, thickness profile and critical buckling mode are shown in Figure 3.16.

3.5.2.3 Design 3

The next design shows a 41% increase in critical buckling load with a total increase in the mass of only 7%. Table 3.7 details the design indicators of Design 3 compared to

Table 3.6: Design indicators for Design 2

	Steered	0°	%increase
N_0(lb/in)	0.2658	0.194	37%
$P_0(lb)$	5.31	3.88	37%
m	0.6006	0.5720	5%

Table 3.7: Design indicators for Design 3

	Steered	0°	%increase
N_0(lb/in)	0.2718	0.194	41%
$P_0(lb)$	5.43	3.88	41%
m	0.6120	0.5720	7%

the benchmark problem. Explicit fiber paths, thickness profile and critical buckling mode are shown in Figure 3.17.

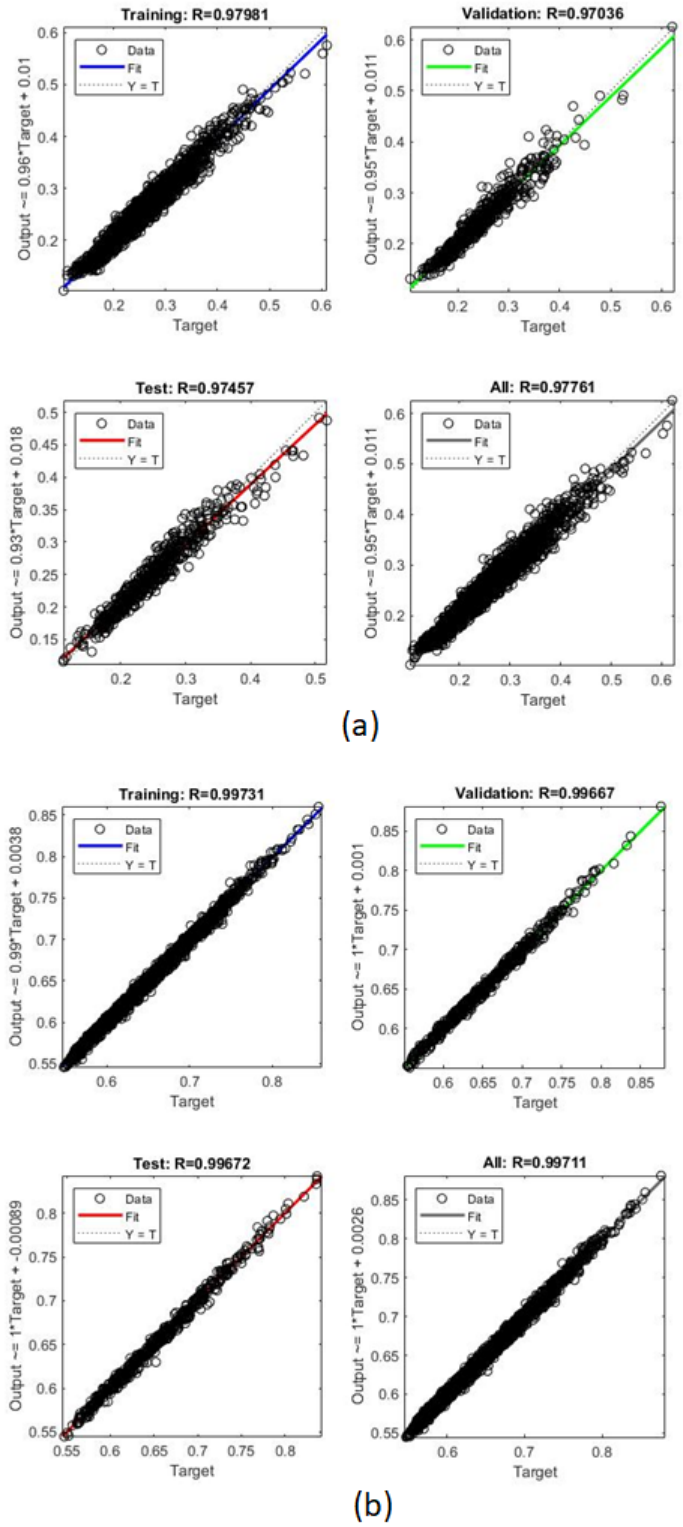

Figure 3.8: Regression values for the ANN fit for case II (a) Critical buckling load (b) Total mass

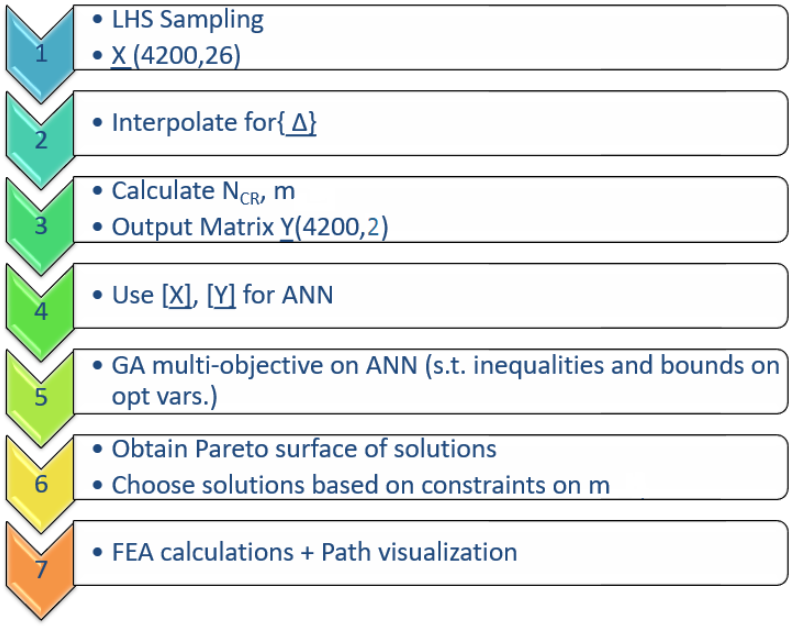

Figure 3.9: Flowchart for optimization methodology using surrogate model (ANN) and Global optimization module for case II

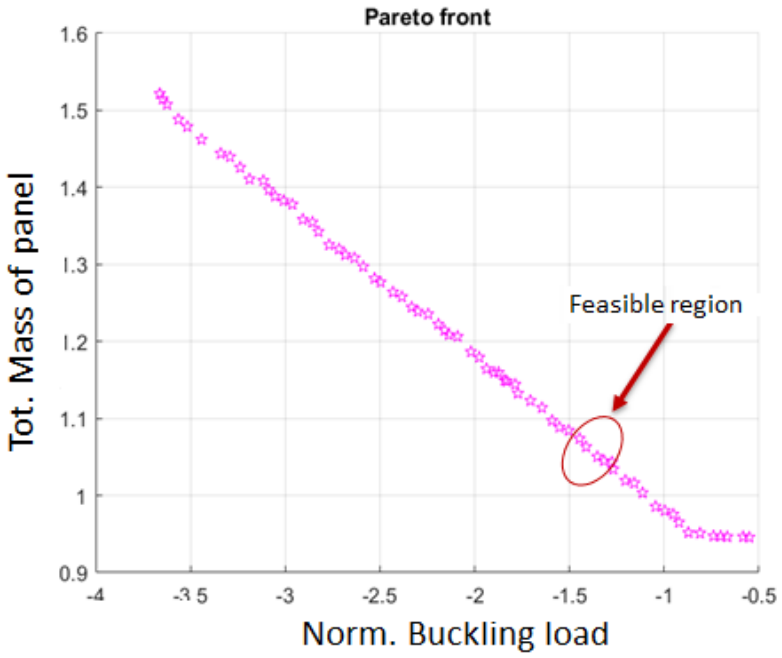

Figure 3.10: Pareto front of optimal solutions to maximize critical buckling load and minimize the mass. The third axis of the surface is K_Y and is hidden in the plot

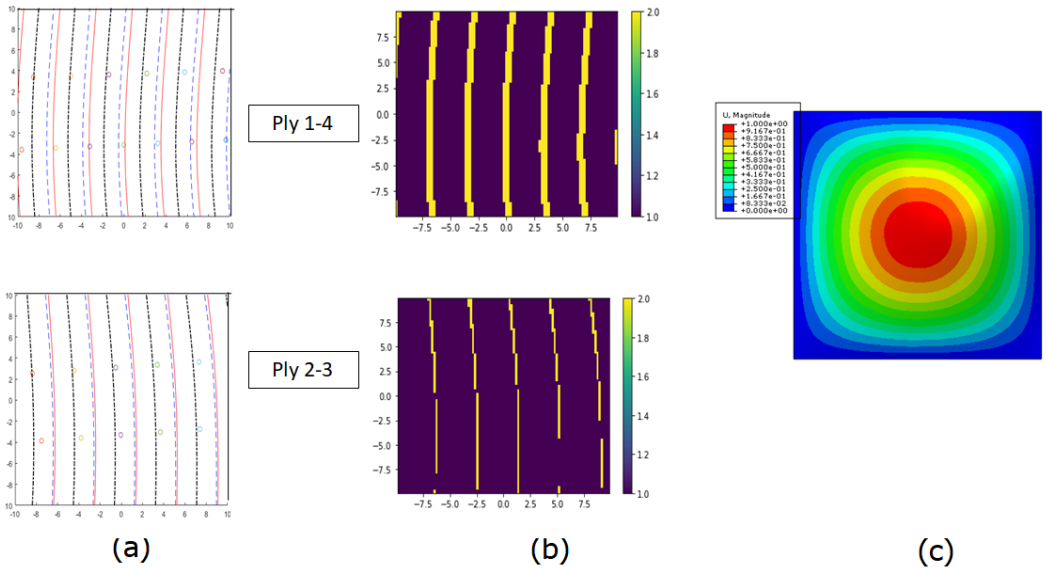

Figure 3.11: Loading case I, Design 1: (a) Fiber paths visualized for both set of independent plies (b) Thickness profile within the plies (c) Critical buckling mode

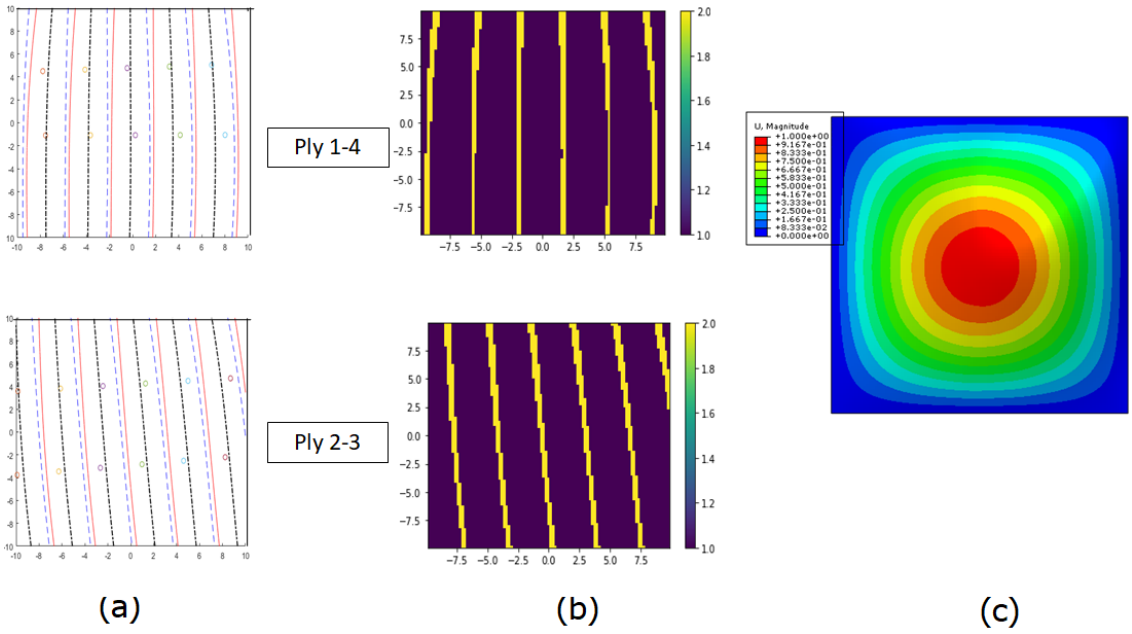

Figure 3.12: Loading case I, Design 2: (a) Fiber paths visualized for both set of independent plies (b) Thickness profile within the plies (c) Critical buckling mode

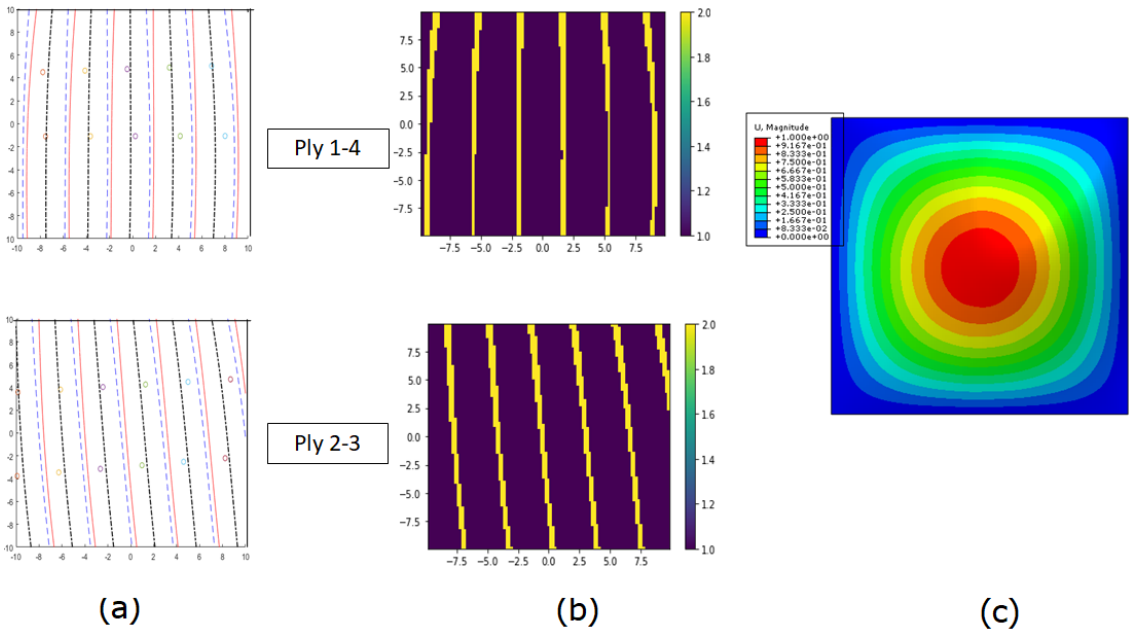

Figure 3.13: Loading case I, Design 3: (a) Fiber paths visualized for both set of independent plies (b) Thickness profile within the plies (c) Critical buckling mode

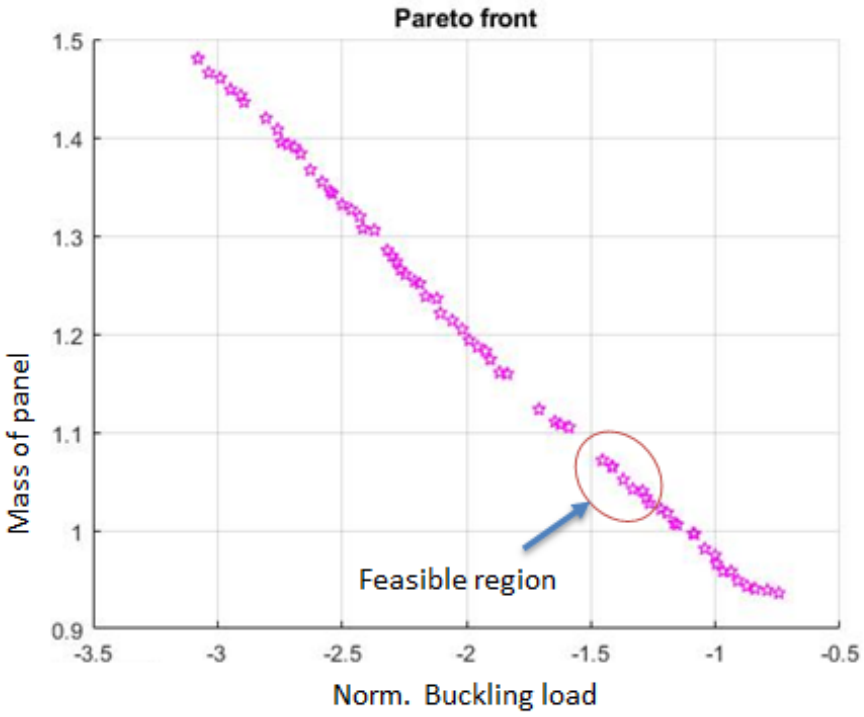

Figure 3.14: Pareto front of optimal solutions to maximize critical buckling load and minimize the mass

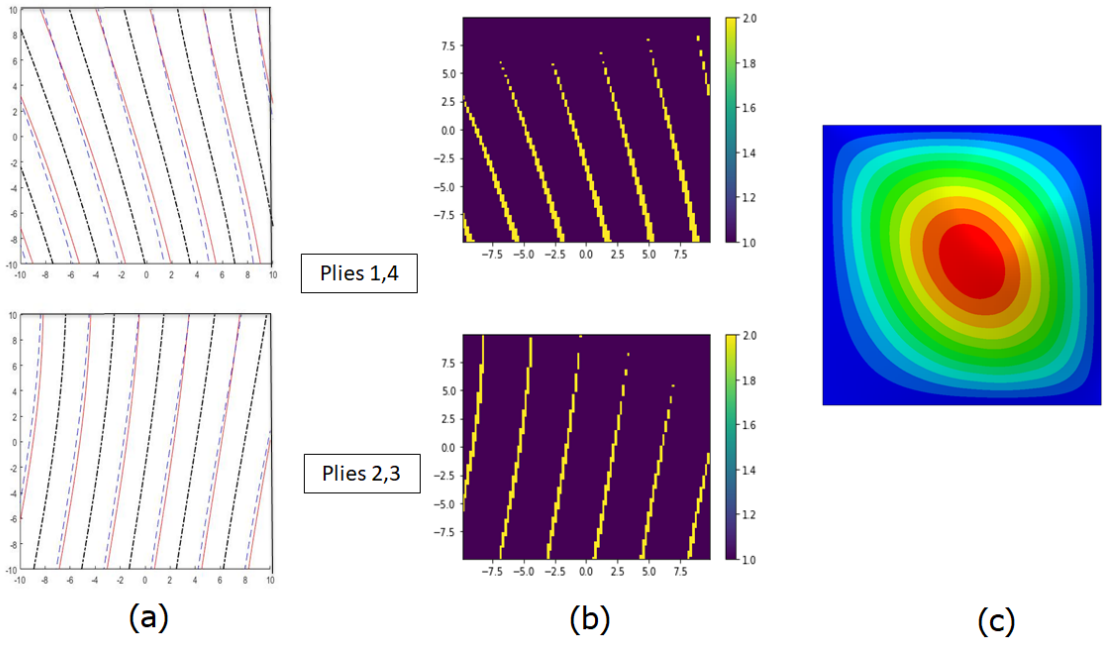

Figure 3.15: Loading case II, Design 1: (a) Fiber paths visualized for both set of independent plies (b) Thickness profile within the plies (c) Critical buckling mode

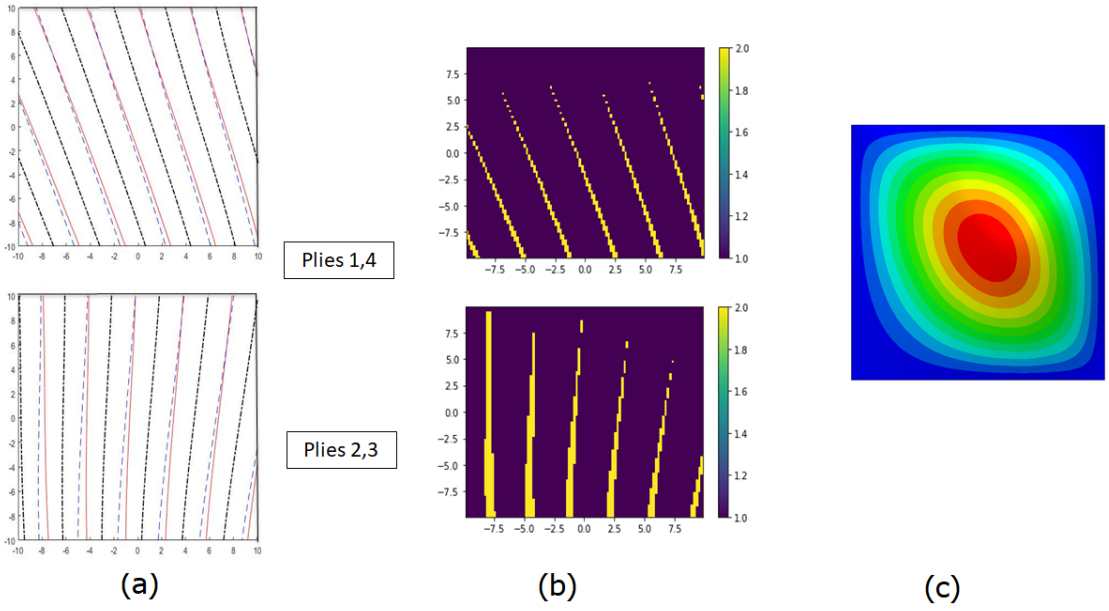

Figure 3.16: Loading case II, Design 2: (a) Fiber paths visualized for both set of independent plies (b) Thickness profile within the plies (c) Critical buckling mode

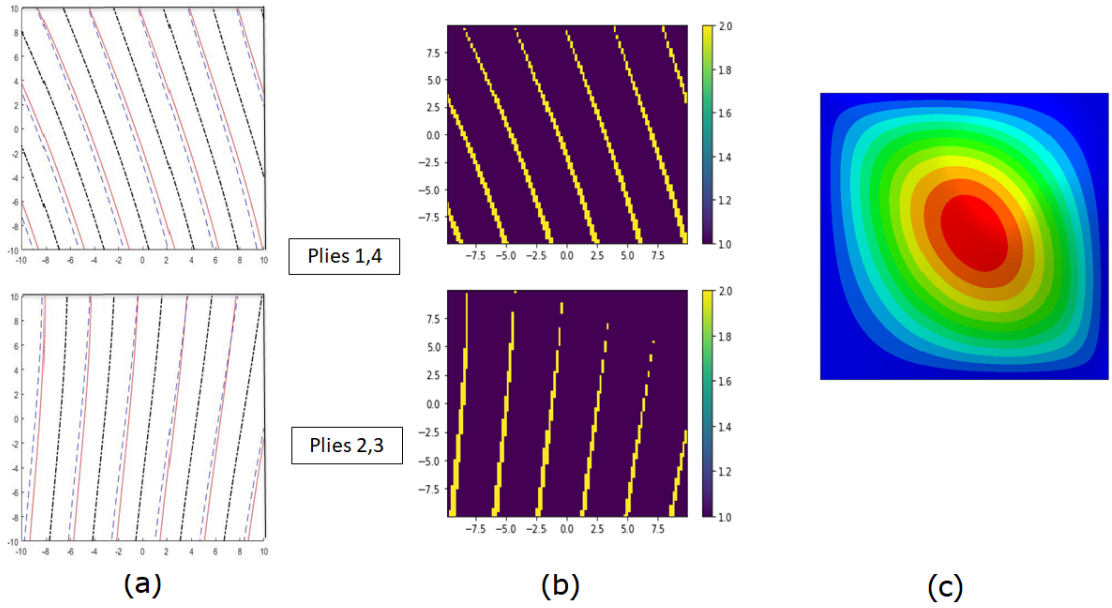

Figure 3.17: Loading case II, Design 3: (a) Fiber paths visualized for both set of independent plies (b) Thickness profile with in the plies (c) Critical buckling mode

CHAPTER IV

Manufacturing and Experimental Validation

In the previous chapter, the detailed algorithm and implementation of a surrogate model based optimization in conjunction with multi-objective Genetic Algorithm (GA) was introduced. Since the multi-objective optimization predicts a *Pareto Front* of feasible solutions, three designs were chosen based on the criteria that the total gain in mass be less than 10%, the decrease in global stiffness capped at 10% and more than 25% increase in buckling load compared to a unidirectional laminate.

4.1 Manufacturing Considerations

These designs were then manufactured by *Electroimpact Inc.* of Mukilteo, WA. A few changes in the designs were made- firstly, in place of a 4 layer laminate $[\theta_1/\theta_2]_S$, an eight layer laminate design was chosen with the same steered fiber angles, θ_1 and θ_2 but with the lay-up $[(\theta_1/\theta_2)_2]_S$. Finite Element calculations were performed to establish that the relative gains in buckling load and mass remained the same for the updated design.

Secondly, an additional constraint was identified while manufacturing, that the first layer being steered causes significant loss of adhesion of the tacky material

thereby causing significant peel off of the fiber tows from the *caul plate*. Thus, a 0° layer was added as the first layer, and to further maintain global symmetry, a 0° layer was added as the last ply, thus making the layup $[0/(\theta_1/\theta_2)_2]_S$.

4.2 Vacuum Bagging and Curing

During the process of curing, the panels are to be vacuum sealed. Thus, prior to being placed in the autoclave, each of the panels are individually vacuum bagged. A schematic of the vacuum bag assembly is as shown in Figure 4.1

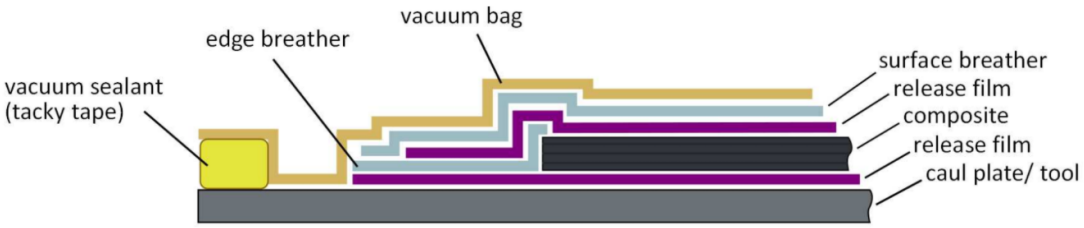

Figure 4.1: Schematic of the vacuum bag assembly to be placed in the autoclave for curing [*Nguyen et al.* (2019a)].

The layup is performed on a thick aluminum plate (*caul plate*). Before any tows are placed, the plate is coated with two to three coats of mold release agent at 5 - 8 minutes interval to ensure easy removal of the parts, post-curing. Once the layup is completed, the vacuum bagging can commence. Firstly, an edge breather material is placed along the boundaries of the part. This is usually a thin strip of woven glass fiber fabric, and ensures a channel for excess resin to flow during the curing process. Further, an additional layer of porous curing film is placed on top of this assembly to ensure easy removal of the part after curing. A breather/bleeder drape is then placed, which would ensure uniform application of pressure on the surface, and also lets any trapped gases to escape. This entire assembly is then covered with a vacuum bag.

This nylon bag is attached to the sides of the plate using a sealant tape/tacky tape. Care must be given to ensure that the all the edges are properly sealed, additional kinks shall be provided to account for the bag being stretched by the vacuum port.

Vacuum port is connected using a perforation on the bagging. Any wrinkles or bubbles should be removed at this stage and a vacuum must be held prior to moving the part into the autoclave. A 28" Hg vacuum is applied, and the assembly is ready for the autoclave if it loses no more than 2" Hg after the vacuum pump is turned off. In the autoclave, a vacuum is held initially. The applied heat and pressure leads to the consolidation of the plies.

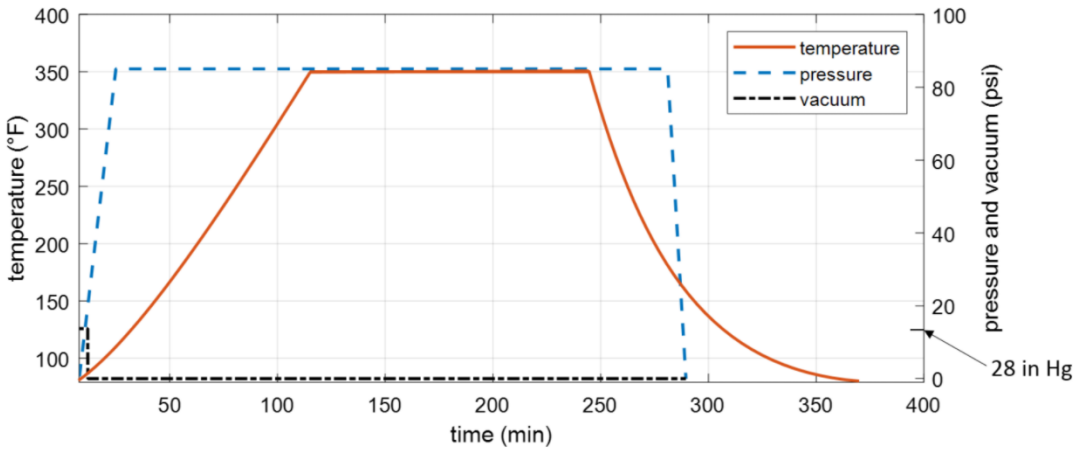

Figure 4.2: Pressure, Temperature and Vacuum during the curing process[*Nguyen et al.* (2019a)]

Cure cycle involves applying high pressure and temperature for a period of time, as shown in Figure 4.2. The pressure is held at 85 psi whereas the temperature gradually rises to 350° F and is held for two hours during the curing process during which the viscosity of the resin decreases to fill any gaps in the lay-up, and the polymeric chains in the resin form cross-links. The pressure and temperature are gradually removed

and the parts cool down to ambient temperature of 70° F.

4.3 Computation of Curvature

The panels were designed flat, though the regions of overlaps act as co-cured stiffeners, causing local unsymmetry. This local unsymmetry causes the panels to have a small initial curvature post-cure. A co-ordinate Measuring Machine (CMM) was used for the same. Firstly, as mentioned in Chapter I, the AFP machine requires an additional 4-5 inches at the beginning and end of the lay-up to ensure sufficient tackiness of the tows, as well as to maintain the required orientations. Thus the manufactured panels are larger than the desired size and the 20 in $\times$20 in square plates are cut-out from these larger as-manufactured panels using water-jet cutting.

A CMM is used to quantify the effect of the curvature of the 20 in $\times$20 in cut panel. CMM is a laser probe attached to a 5-axis robotic arm. To measure the co-ordinates, the plates are vertically rested on an aluminum frame. The laser probe is then used to manually scan both sides of the panels to obtain point cloud data of the individual panels. The origin of the co-ordinate system is the base of the robotic arm.

4.3.1 Processing of point cloud data

The front and back surfaces of each panel is scanned, resulting in a point cloud data that has millions of entries for each panel. Since the CMM cannot distinguish between the panel and the frame it is resting on, a two step data clean up process is initiated. The data is rotated to align with the global axes of the system. A coarse clean up is then performed by removing any out of plane displacement that is larger that the thickness of the panel. For a fine clean up, the near edges of the panels and any noise around them are eliminated. This results in a slightly smaller panel than

the physical plate. This process is shown in in Figure 4.3.

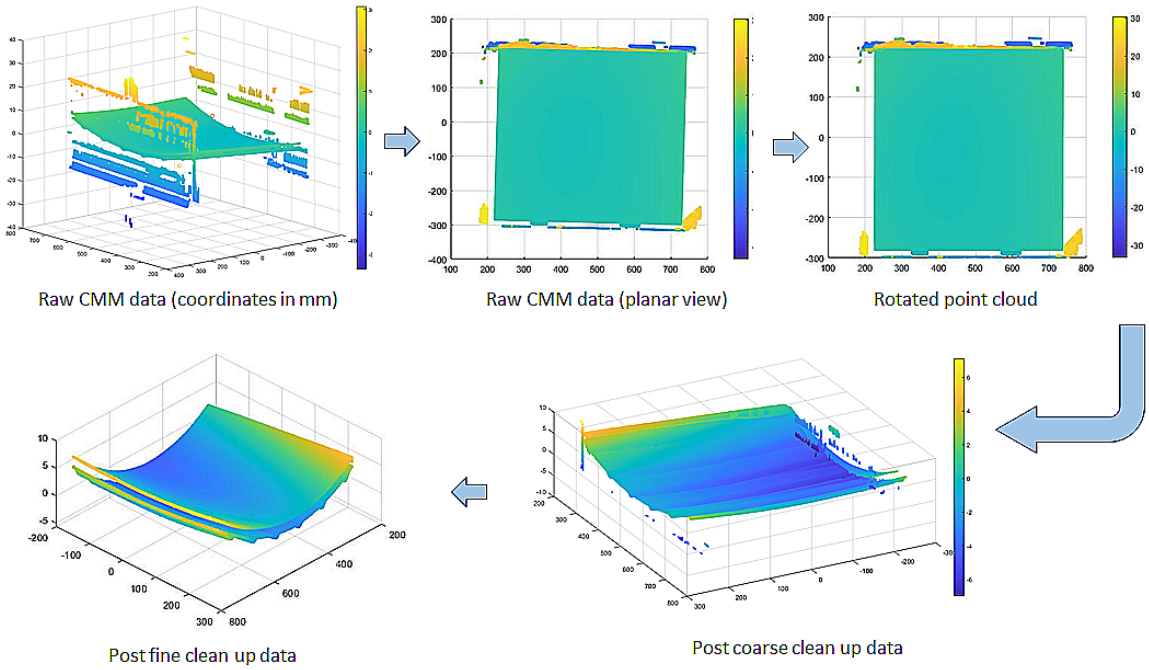

Figure 4.3: Different stages of cleaning raw CMM data to obtain panel curvature

4.3.2 Separation of surfaces

Since the point cloud data set is large, computations on it are slower. To separate out the top and bottom surfaces of the panels, the following algorithm is used. A least squares fit is obtained for the point cloud data. Since the bottom surface is the tool side while laying up and curing, it is smooth. The bagging surface (top) thus has varying thicknesses due to overlaps. This fitted surface intersects the top surface. A cubic polynomial is used to fit the surfaces, and can be expressed as,

$$f(x,y) = p_{00}+p_{10}x+p_{01}y+p_{20}x^2+p_{11}xy+p_{02}y^2+p_{30}x^3+p_{21}x^2y+p_{12}xy^2+p_{03}y^3 \quad (4.1)$$

This polynomial can be offset by a constant z_0, a fraction of the laminate thickness, which creates a demarcation between the two surfaces

$$f(x,y) = p_{00} + z_0 + p_{10}x + p_{01}y + p_{20}x^2 + p_{11}xy + p_{02}y^2 + p_{30}x^3 + p_{21}x^2y + p_{12}xy^2 + p_{03}y^3 \tag{4.2}$$

For each (x,y,z) in the point cloud, corresponding $f(x,y)$ is calculated and the following conditional statement is applied to separate the two surfaces,

$$\begin{cases} If \quad f(x,y) \leq z(x,y) \implies \text{Bottom surface} \\ If \quad f(x,y) \geq z(x,y) \implies \text{Top surface} \end{cases} \tag{4.3}$$

A schematic of the procedure is shown in Figure 4.4

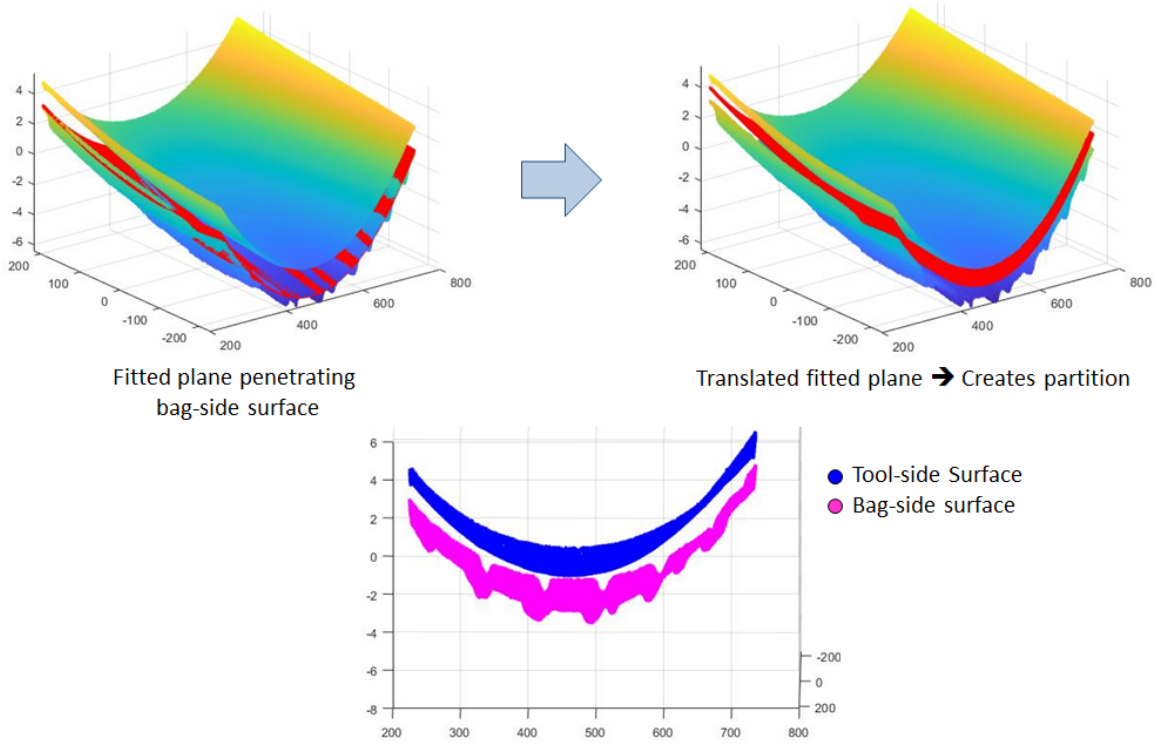

Figure 4.4: Partitioning the top and bottom surface from the point cloud data

4.4 Optical Microscopy studies on thickness variations

As mentioned previously, the manufacturer has a constraint of approximately 4-5 inches of tape to be laid before and after the design area to provide additional tension to the tapes while laying up. Thus the manufactured panels were 30 in $\times$30 in in dimension, from which the center portion of 20 in $\times$20 in dimensions were cut-out using water jet cutting. To identify the effect of overlap locations on the thickness variations within the panel, an optical microscopy study was conducted. This involved cutting 8 in $\times$1 in coupons from the overhang location of each of the nine manufactured panels as described in the Figure 4.5. Each coupon was cutout to have at least two overlaps within the length. It is to be noted that since the fiber courses had the capability to vary individually, the width of the overlap locations are not constant. This provided four possible overlap locations per coupon, two on each side, as explained in the Figure 4.5. Overlaps #1 and #2 are located 1in inside the edges of the overhang portion, and overlaps #3 and #4 are located 2in inside the overhang portion. Figure 4.6 shows the microscopy images and the four overlaps in panel #1 of each of the three designs.

An open-source MATLAB®program, GRABIT is used to analyze these images by extracting the thickness data. GRABIT has a GUI interface that lets the user load an image and calibrate the axis by providing a scale and the co-ordinate data with respect to the origin of each point that is clicked by the user is then saved by the program. This information can then be used to calculate the thickness of each layer at selected points. A total of 104 overlaps were analyzed and a scatter plot of the measured thickness is provided in Figure 4.7. The average thickness of all the measured overlaps were calculated to be 0.0069 in as compared to a nominal thickness of 0.0075 in of the pristine material, approximately 92%.

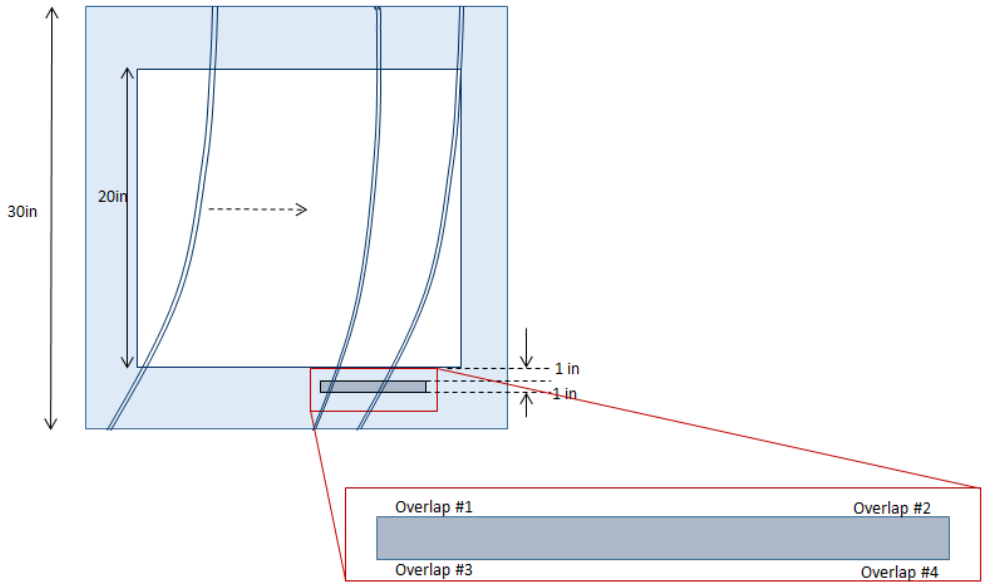

Figure 4.5: Location of microscopy specimen within the manufactured panels

Figure 4.6: Microscopy images of overlap locations in Panel of each design

4.5 Experimental Set up for in-plane compression tests

4.5.1 Fixture Design

A fixture is designed to conduct the in-plane compression tests of the manufactured panels, resembling a standard compression after impact (CAI) test fixture as described in *ASTM D7137/D7137M* (2017). A uni-axial test is performed for which

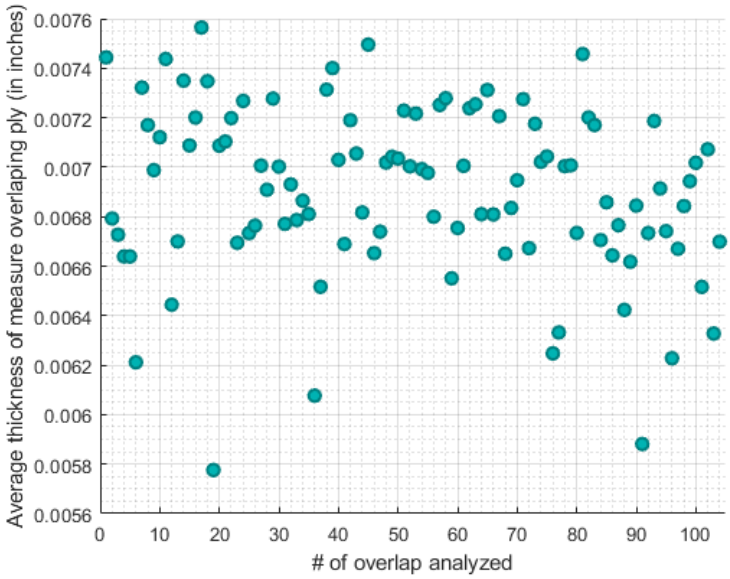

Figure 4.7: Scatter plot of measured thickness at overlap locations

the plate is installed in a multi- piece fixture with encastré loading edges and firmly fixed in between knife supports on the transverse edges. The optimization studies for in- plane compression were performed on design cases with simply supported boundary conditions on all sides, but the in- plane compression testing was conducted using clamped loading edges with encastré boundaries. Hence the tested panels are not necessarily optimal for those loading conditions. However, finite element models of the experiment and corresponding straight fiber paths were used to establish that these steered fiber paths were still superior in compressive response compared to straight fiber panels.

The modification to the standard CAI test fixture is that the loading edges on the top and bottom are now fully encastréd using steel putty to resemble an ideally clamped boundary condition. The fixtures for the loading edges are made out of 1.5 in thick Aluminum 6061 bars, with a slot 0.75 in deep milled out of one surface. The information from the curvature study is used to compute the approximate radius of curvature of the panels at the loading edges. The average radius of curvature for all

9 manufactured panels was calculated to be approximately 390 in. Thus the slot is curved with a radius of 390 in as shown in the Figure 4.8. In addition, four threaded holes are tap drilled on the four corners to install aligning rods during the curing of the putty to ensure the plates are held vertically and centered by attaching to the corresponding corners of the top fixture (Figure 4.9). These aligner rods are used only during the process of hardening of the putty and is removed during the compression testing of the specimen.

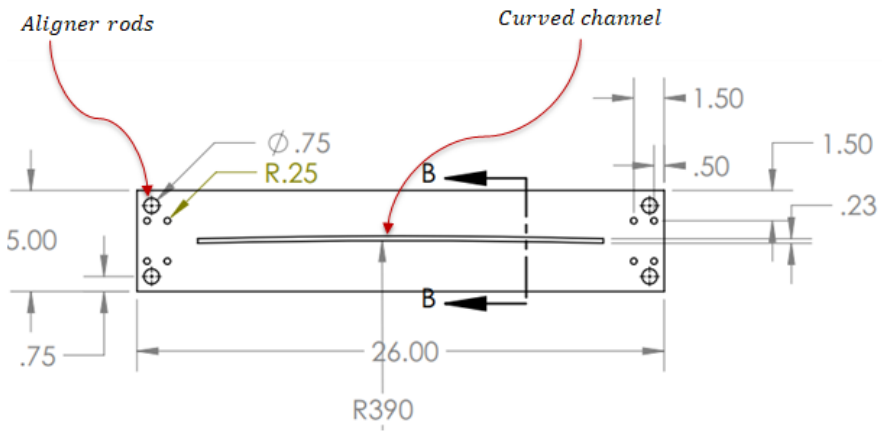

Figure 4.8: Details of the bottom fixture. Milled curved channel with R= 390in for sliding in the test specimen. Tap drills for aligner rods to ensure vertical centering of the test specimen. Tap drills for attaching L- clamps for side fixtures

The bottom fixture also has tap drilled holes to attach an L- clamp that would be used to install the knife support for the transverse edges similar to a standard CAI fixture. The knife supports ensure that there is no out of plane displacement along the edges, but allows for rotations, resembling an ideal simply supported boundary condition. An image of the assembled fixture is shown in Figure 4.10.

To begin the process of installing the putty, the L clamps are assembled on the bottom fixture and the knife supports are loosely attached. The curved channel in

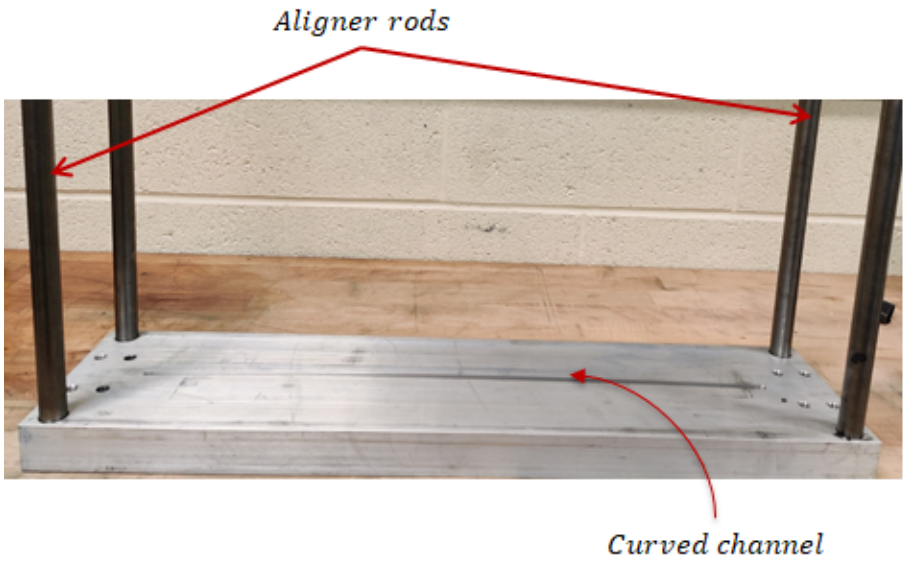

Figure 4.9: Bottom fixture showing curved channel and attached aligner rods

the bottom fixture is filled with a viscous putty mixture by combining the polymer and hardener. The test specimen is slowly lowered into the channel and any excess overflow of the putty is scraped off, ensuring a smooth contact. The knife supports are tightened to ensure the alignment, followed by the four aligner rods. The top fixture is then lowered to ensure the assembly is centered and vertical. The putty is allowed to harden for 24 hours. The top fixture and the side supports are then removed. The assembly is then flipped and the top fixture is placed on top of steel blocks of 6 in height. This is to allow for the aligner rods to suspend when the flipped specimen is lowered. The process is repeated by filling the channel with the putty mixture, followed by lowering the specimen along with the bottom loading edge which is now firmly attached to the specimen. Any excess putty is scraped off ensuring smooth contact. The aligner rods help to center and align the specimen. A nut is tightened on the aligner rods to ensure the specimen is fully immersed, after which the putty is allowed to cure and harden for 24 hours. Once the two fixtures are firmly attached to the specimen, the aligner rods are removed.

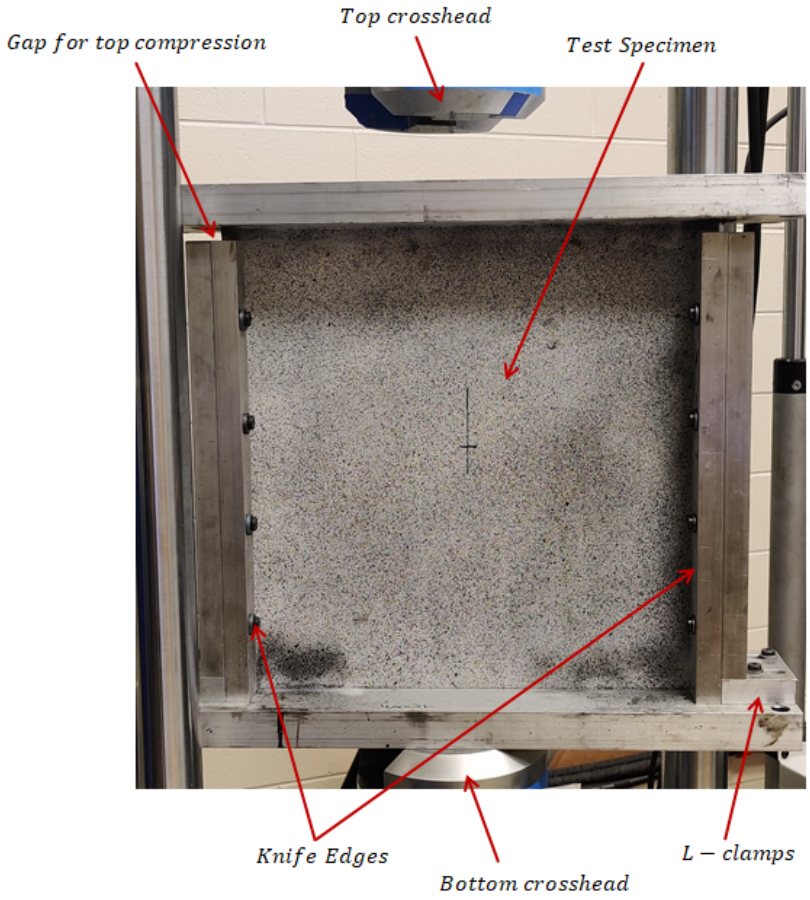

Figure 4.10: Experimental fixture showing the end supports and machine cross heads

4.5.2 Specimen and camera set-up

To assemble the final test specimen, the L clamps are tightly attached to the bottom fixture. The four knife supports are then attached to the L- clamps firmly. Any gaps in contact of the knife supports are corrected by placing 0.004in aluminum shims until a firm contact is ensured. Once the side supports are ensured, a 0.5in unsupported end remains as shown in Figure 4.10, which allows for the end shortening during the compression, similar to a standard CAI fixture.

The specimens are then speckled randomly with black and white paint on both

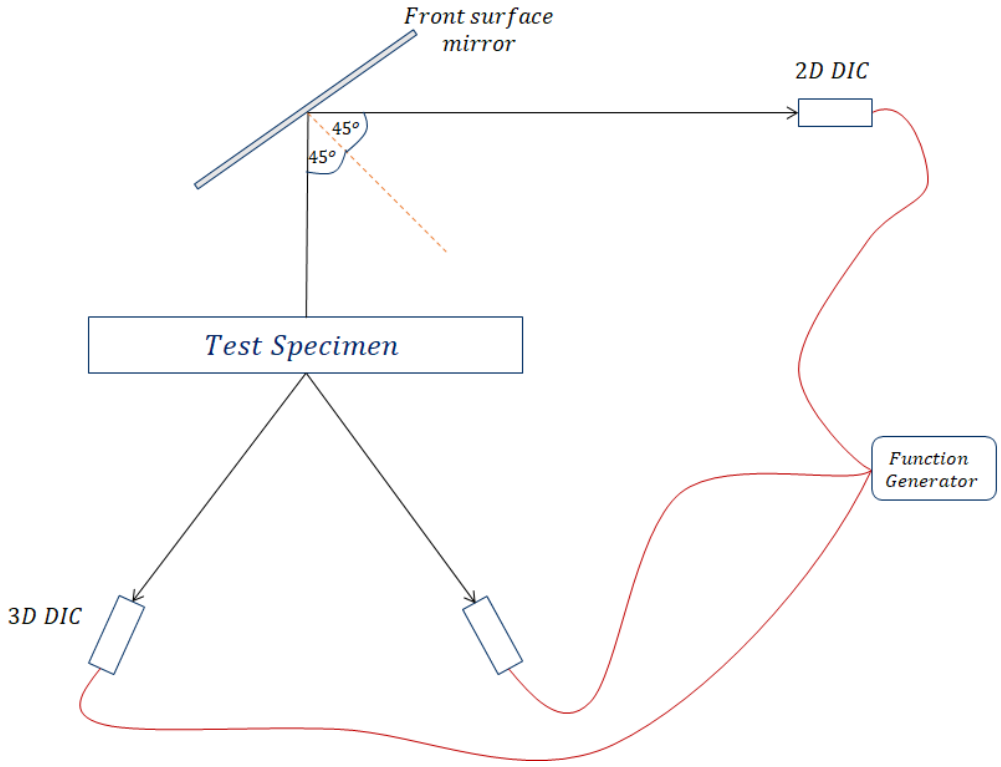

Figure 4.11: Schematic of set-up of DIC cameras, along with front surface mirror

surfaces to aid in Digital Image Correlation (DIC) for obtaining the in-plane and out-of-plane displacement data while under compressive loading. Two point grey (FLIR) Grasshopper2 cameras are used on the front surface for 3D DIC measurements. These cameras are calibrated using standard calibration technique using a 300 mm $\times$240 mm calibration board. A single grasshopper camera is used for 2D DIC measurements on the back surface. To ensure sufficient distance to capture the full area of the specimen by the 2D DIC camera, a 20 in $\times$20 in front surface mirror is used at an angle of 45° to bend the light rays. A function generator is used to synchronize the three cameras so as to take the images at the same time stamp. A schematic of the test set-up is shown in Figure 4.11.

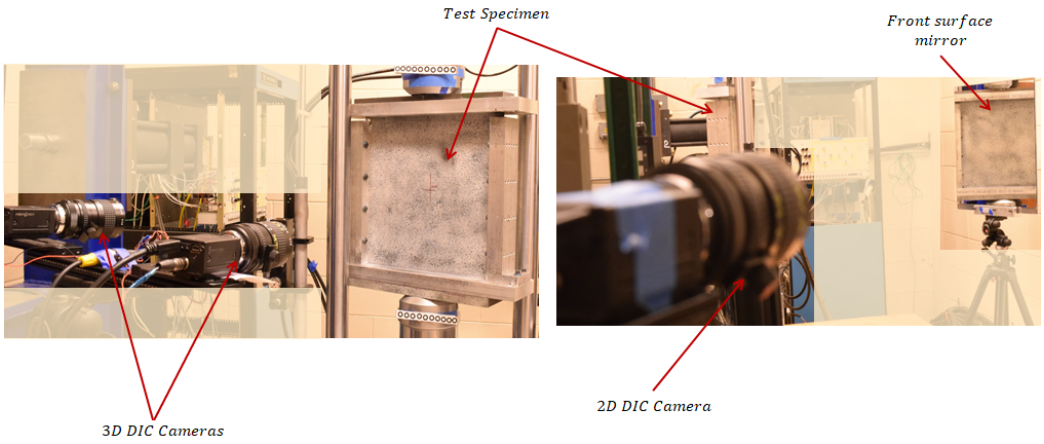

Figure 4.12: Experimental set up showing test specimen, front surface mirror and 2D and 3D DIC cameras

4.5.3 Computing load point displacement

Buckling is a stability problem. If the structure is perfectly flat without any geometric imperfections in terms of surface variations or load eccentricity, the structure is expected to buckle at which point it moves from one stable flat equilibrium state to another non-flat state. In reality the structure is neither perfect, due to manufacturing imperfections and presence of thickness variations on one surface, nor is the loading perfectly centered. Thus, the structure starts to respond with movement away from a flat state immediately as the load is applied. Since the panel is thin, with a nominal thickness of 0.075 in, it is important to identify that the front and back surface will have different in-plane vertical displacements due to the bending of the structure as the load is applied. Using DIC to obtain displacement on both surfaces (front and back), mid-plane displacement could thus be computed as the average of the two values.

To obtain the displacement at the front surface, displacement of the top and bottom of the front surface is computed in the shaded area shown in the Figure 4.13.

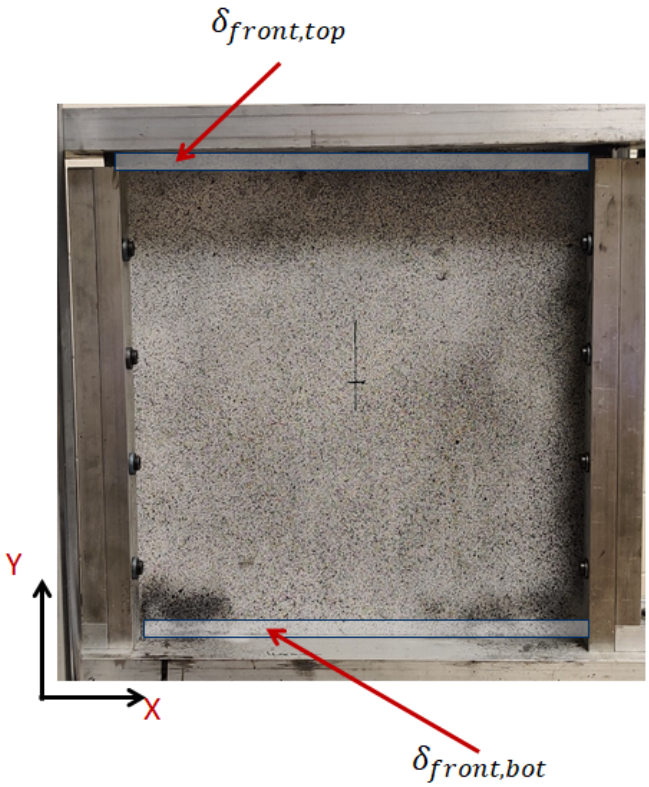

Figure 4.13: Average displacement of the top and bottom of the front surface is computed across the shaded areas.

The distribution of the vertical displacement across the shaded areas on the top and bottom in Figure 4.13 for the testing of Design #1 Panel #1 is shown in Figure 4.14. Since the variation is fairly uniform, the average values across the shaded areas are used. The average vertical displacement v_y over the shaded areas can be expressed as shown in Equations 4.4- 4.7.

$$\delta_{front,bottom} = \frac{1}{A} \iint_A v_y^{front,bottom}(x,y)dA \tag{4.4}$$

$$\delta_{front,top} = \frac{1}{A} \iint_A v_y^{front,top}(x,y)dA \tag{4.5}$$

$$\delta_{back,bottom} = \frac{1}{A} \iint_A v_y^{back,bottom}(x,y)dA \tag{4.6}$$

$$\delta_{back,top} = \frac{1}{A} \iint_A v_y^{back,top}(x,y)dA \tag{4.7}$$

To get the load point displacements, the following calculations are performed.

$$\delta_{front} = \delta_{front,bottom} - \delta_{front,top} \tag{4.8}$$

$$\delta_{back} = \delta_{back,bottom} - \delta_{back,top} \tag{4.9}$$

$$\delta_{avg} = \frac{\delta_{front} + \delta_{back}}{2} \tag{4.10}$$

The variation of load point displacements for Design #1 Panel #1, averaged over the top and bottom regions as presented in Equation 4.8 and Equation 4.9 respectively is shown in Figure 4.15. The variation of average mid-plane displacement in Equation 4.10 is also shown.

4.6 Experimental Results

A Shorewestern 302 Series two column floor standing axial frame, with a load cell capacity of 35 kips is used for the compression testing. The load cell is calibrated and used to record the load data every 10 seconds. The displacement data is obtained using DIC as mentioned in section 4.5.3, computed using Equation 4.8, Equation 4.9 and Equation 4.10. A timer is set up to ensure the loading and image recording to

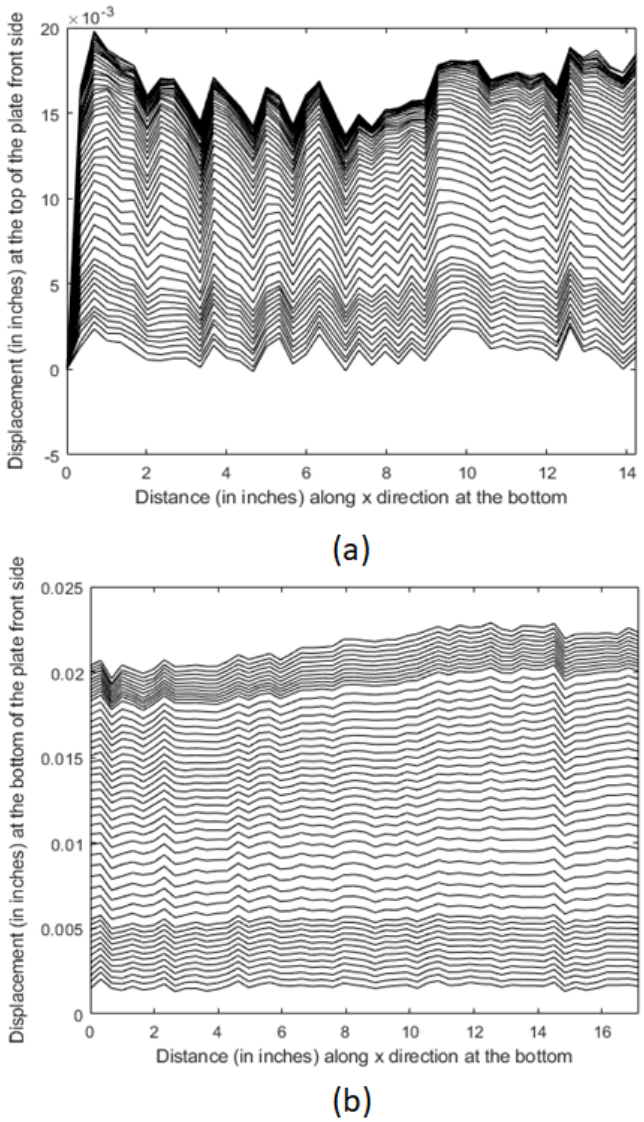

Figure 4.14: Testing of Design #1 Panel #1 at time $t = 100$ seconds (a) Variation of vertical displacement along the top shaded region on the front surface (b) Variation of vertical displacement along the bottom shaded region on the front surface

begin simultaneously. A MATLAB ®script is then used to ensure that the load data and displacement data are interpolated to the same time scale.

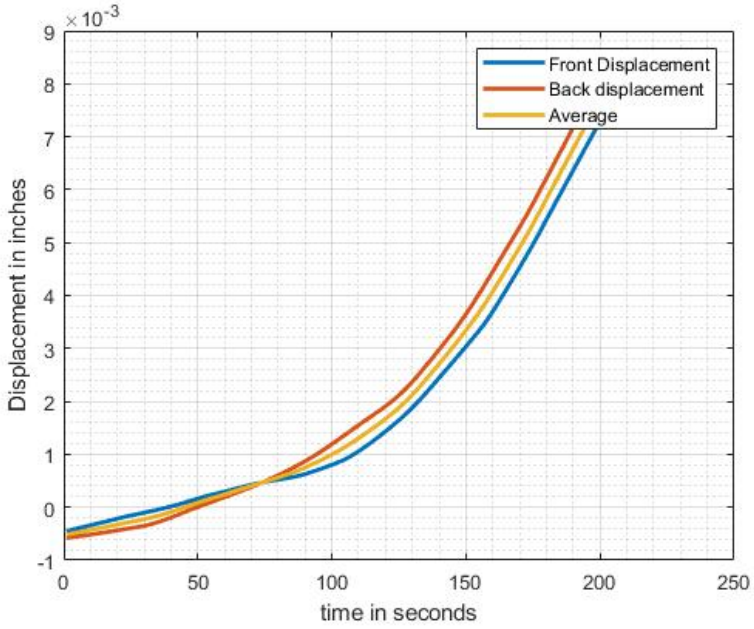

Figure 4.15: Testing of Design #1 Panel #1: variation of load point displacement on the front and back surfaces along with the average computed mid plane displacement

4.6.1 Computing Transition Load

As explained in section 4.5.3, due to imperfections in the structure and eccentricity of loading, the structure starts to respond on application of loading. The load v/s load point displacement behavior of the structure is expected to be bi-linear. An average transition load for the response is obtained by drawing tangents to these linear curves, and the point of intersection of the two tangents is considered the transition load, corresponding to the buckling load of a perfect structure. The following sections details the experimental results for each of the three designs.

4.6.2 Design #1

The load v/s load- point displacement of Panels #1, #2 and #3 of Design #1 is shown in Figure 4.16, Figure 4.17 and Figure 4.18 respectively. The initial and

Table 4.1: Initial stiffness ($in10^6 lb/in$) and Transition Loads (in lbs) for Design #1

#	Initial Stiffness ($in10^6 lb/in$)	Transition Loads (in lbs)
$Panel\#1$	1.17	2100
$Panel\#2$	1.28	2100
$Panel\#3$	1.25	2000

post-buckling stiffnesses are indicated, along with the computed transition loads. Table 4.1 tabulates the initial stiffness and transition load of all three panels.

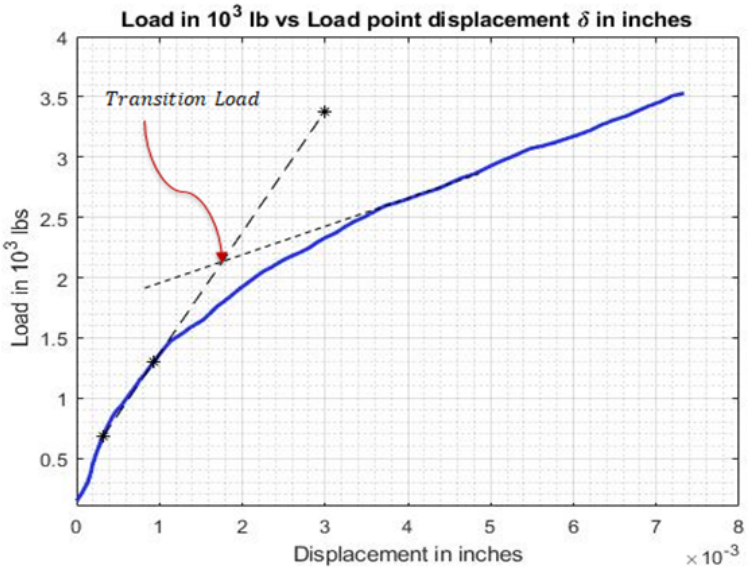

Figure 4.16: Load (in $10^3 lbs$) v/s load point displacement (in inches) for Design #1 Panel #1

A summary of load v/s out-of-plane displacement at the mid point is shown in Figure 4.19.

4.6.3 Design #2

The load v/s load- point displacement of Panels #1, #2 and #3 of Design #2 is shown in Figure 4.20, Figure 4.21 and Figure 4.22 respectively. Among the three specimens, Panel #2 was tested until material failure. The initial and post-buckling stiffnesses are indicated, along with the computed transition loads. Table 4.2 tabu-

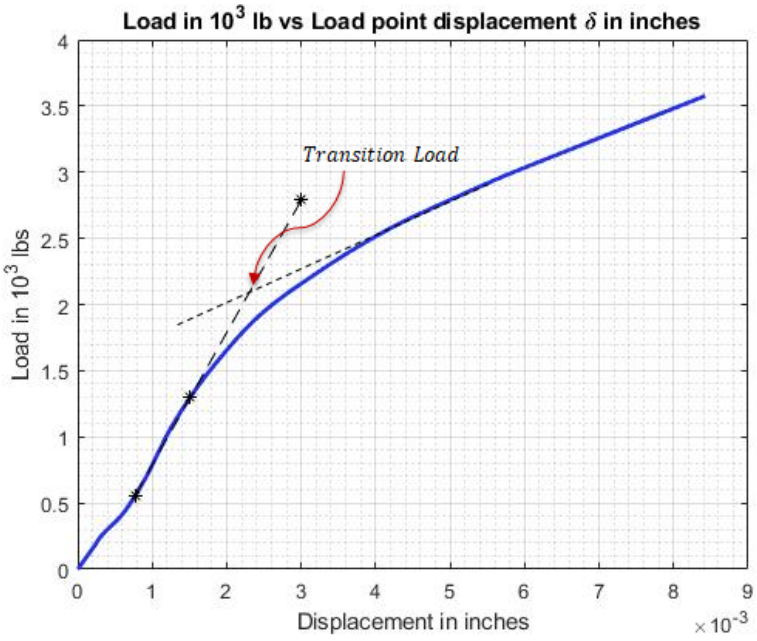

Figure 4.17: Load (in $10^3 lbs$) v/s load point displacement (in inches) for Design #1 Panel #2

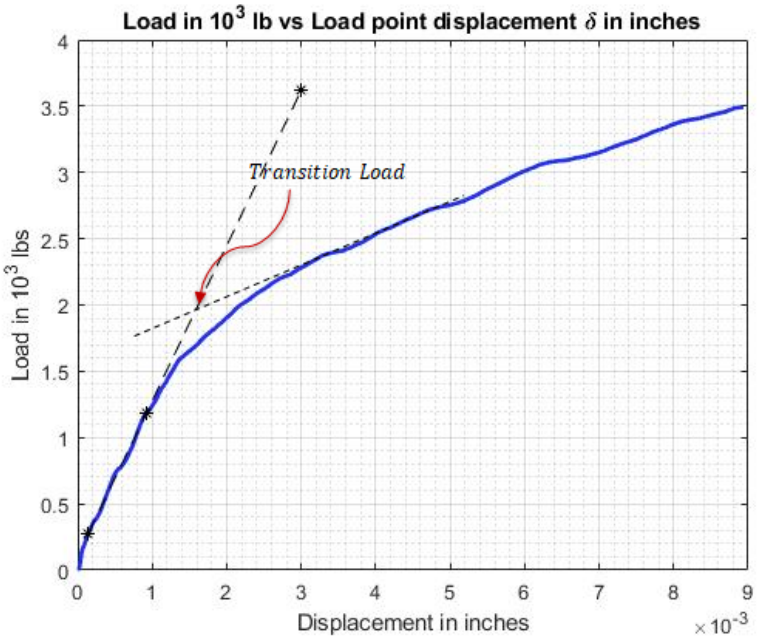

Figure 4.18: Load (in $10^3 lbs$) v/s load point displacement (in inches) for Design #1 Panel #3

lates the initial stiffness and transition load of all three panels.

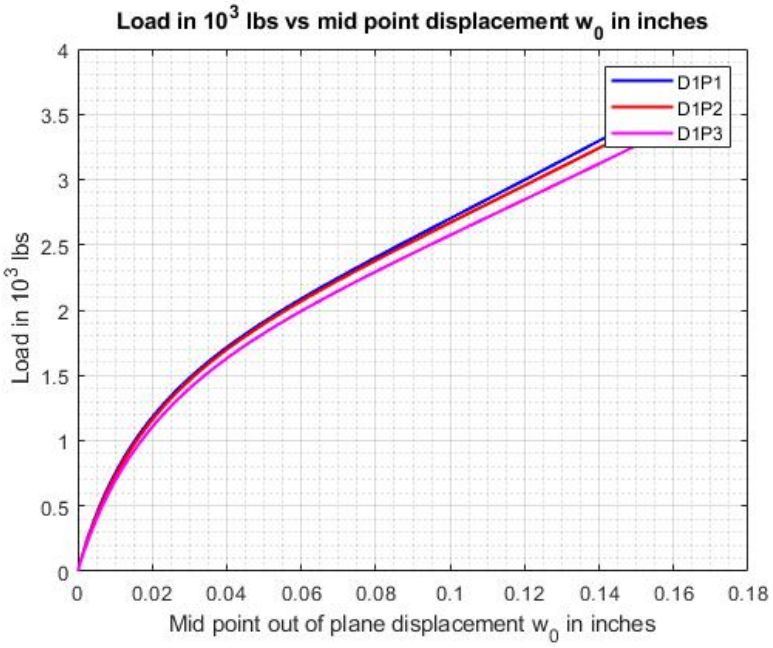

Figure 4.19: Load (in $10^3 lbs$) v/s mid point out-of-plane displacement (in inches) for Design #1

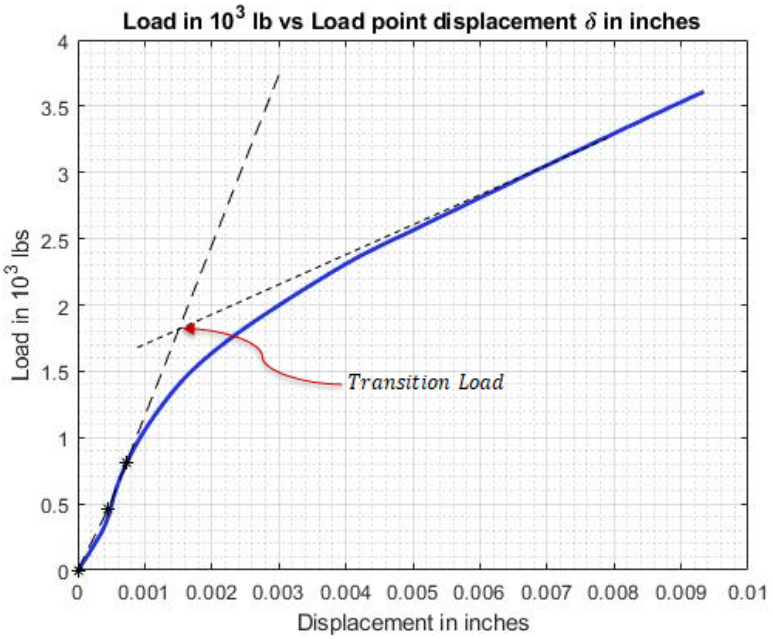

Figure 4.20: Load (in $10^3 lbs$) v/s load point displacement (in inches) for Design #2 Panel #1

A summary of load v/s out-of-plane displacement at the mid point is shown in Figure 4.23.

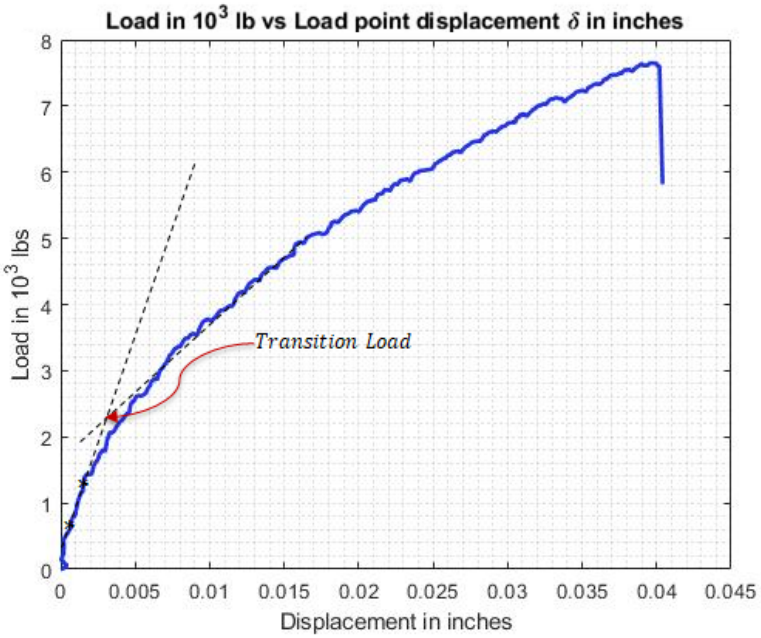

Figure 4.21: Load (in $10^3 lbs$) v/s load point displacement (in inches) for Design #2 Panel #2

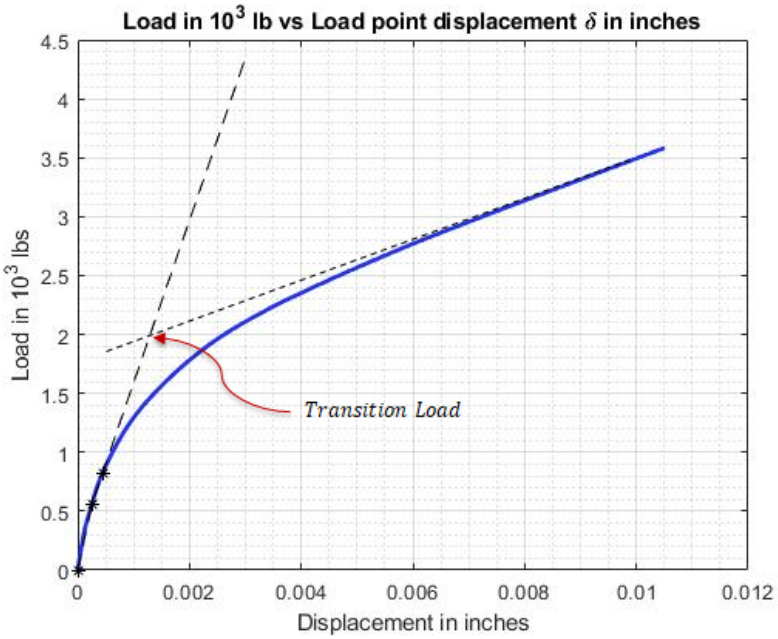

Figure 4.22: Load (in $10^3 lbs$) v/s load point displacement (in inches) for Design #2 Panel #3

4.6.4 Design #3

The load v/s load- point displacement of Panels #1, #2 and #3 of Design #3 is shown in Figure 4.24, Figure 4.25 and Figure 4.26 respectively. The initial and

Table 4.2: Initial stiffness ($in10^6 lb/in$) and Transition Loads (in lbs) for Design #2

#	Initial Stiffness ($in10^6 lb/in$)	Transition Loads (in lbs)
$Panel\#1$	1.12	1800
$Panel\#2$	1.31	2150
$Panel\#3$	1.23	2000

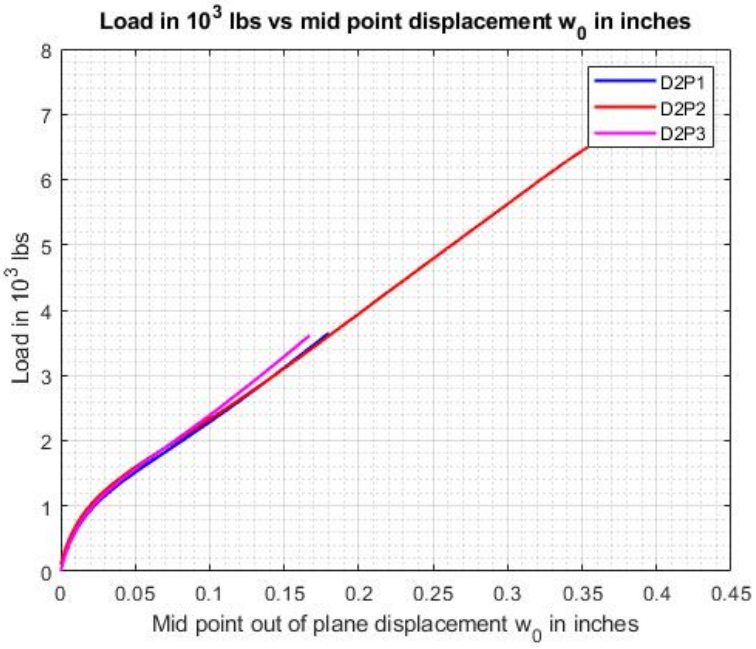

Figure 4.23: Load (in $10^3 lbs$) v/s mid point out-of-plane displacement (in inches) for Design #2

post-buckling stiffnesses are indicated, along with the computed transition loads. Table 4.3 tabulates the initial stiffness and transition load of all three panels.

A summary of load v/s out-of-plane displacement at the mid point is shown in Figure 4.27.

Table 4.3: Initial stiffness ($in10^6 lb/in$) and Transition Loads (in lbs) for Design #3

#	Initial Stiffness ($in10^6 lb/in$)	Transition Loads (in lbs)
$Panel\#1$	1.18	1750
$Panel\#2$	1.16	1900
$Panel\#3$	1.08	1800

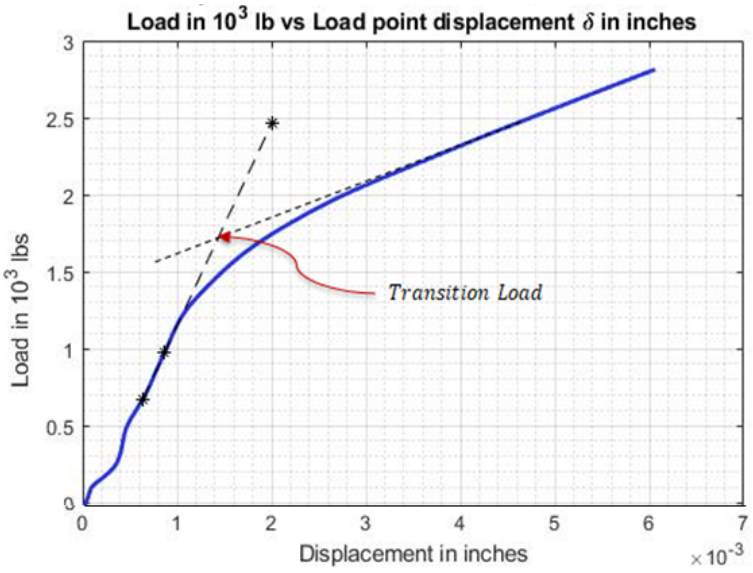

Figure 4.24: Load (in $10^3 lbs$) v/s load point displacement (in inches) for Design #3 Panel #1

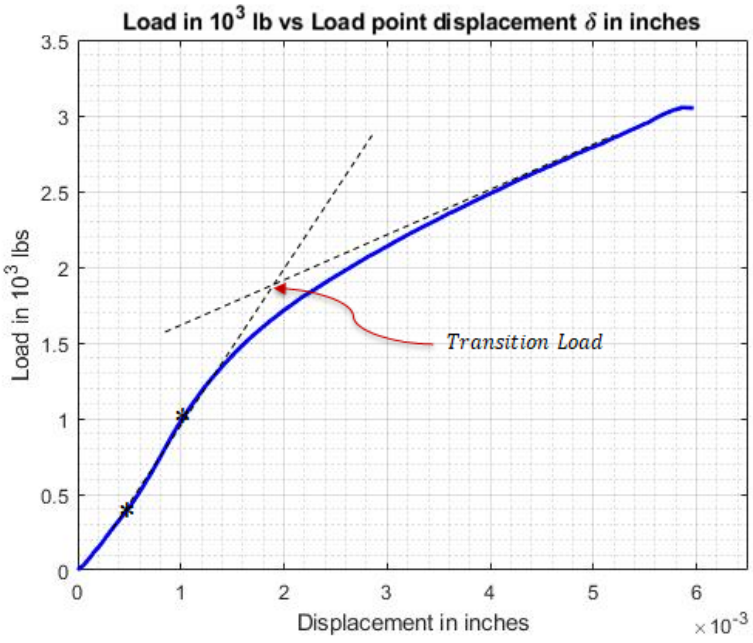

Figure 4.25: Load (in $10^3 lbs$) v/s load point displacement (in inches) for Design #3 Panel #2

4.7 Summary of Test Results

Three specimens of each of the three designs were tested to observe the load v/s load point displacement response under in-plane compression. The average transition

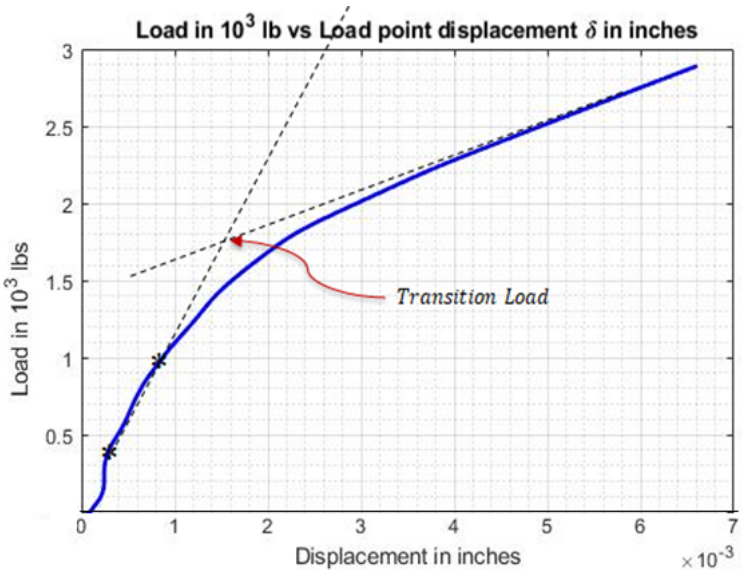

Figure 4.26: Load (in $10^3 lbs$) v/s load point displacement (in inches) for Design #3 Panel #3

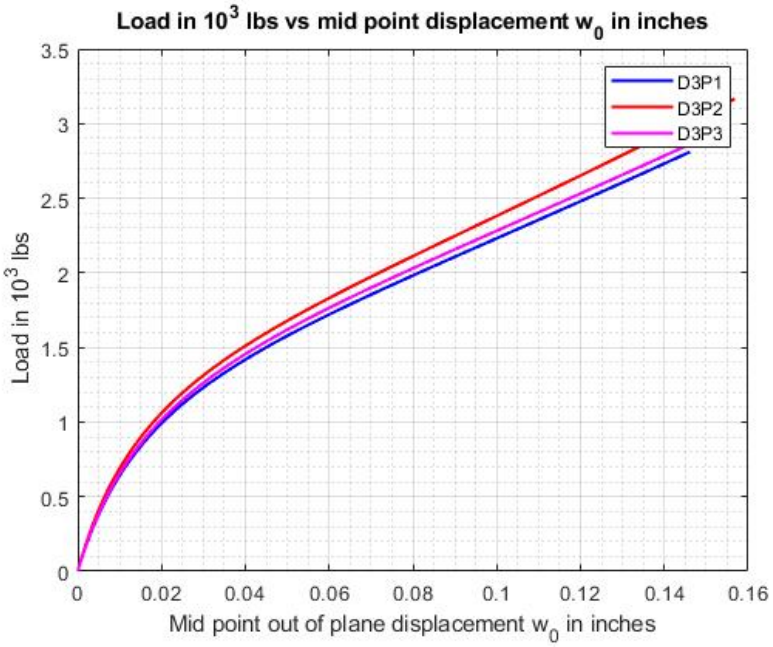

Figure 4.27: Load (in $10^3 lbs$) v/s mid point out-of-plane displacement (in inches) for Design #3

load for Design #1, Design #2 and Design #3 are 2067 lbs, 1983 lbs and 1817 lbs respectively. For the sake of brevity, one sample of each design was loaded to failure. The failure load of Design #1 Panel #1 was 9130 lbs, the failure load of Design #2

Panel #2 was 7650 lbs and, the failure load of Design #3 Panel #2 was 8820 lbs. The load v/s load point displacements of all three specimens of each of the designs and their corresponding failure loads are shown in Figure 4.28, Figure 4.29 and Figure 4.30.

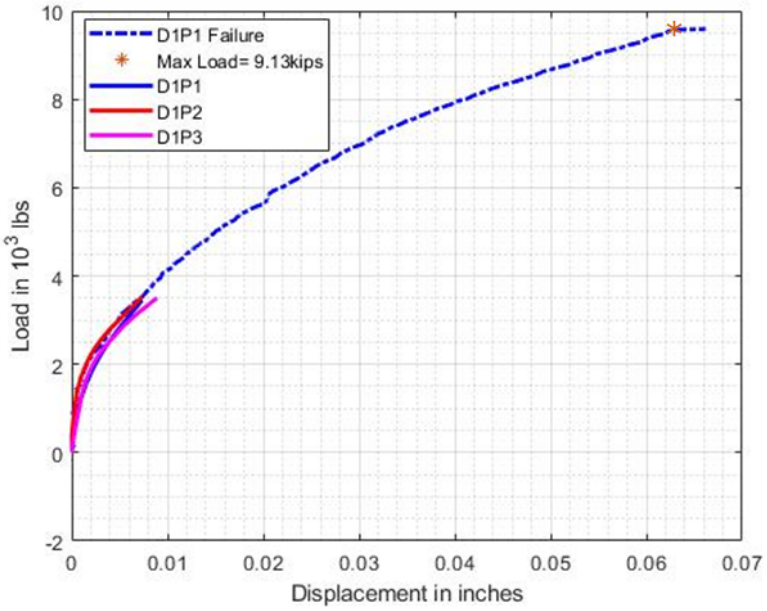

Figure 4.28: Summary of load (in $10^3 lbs$) v/s load point displacement (in inches) for Design #1

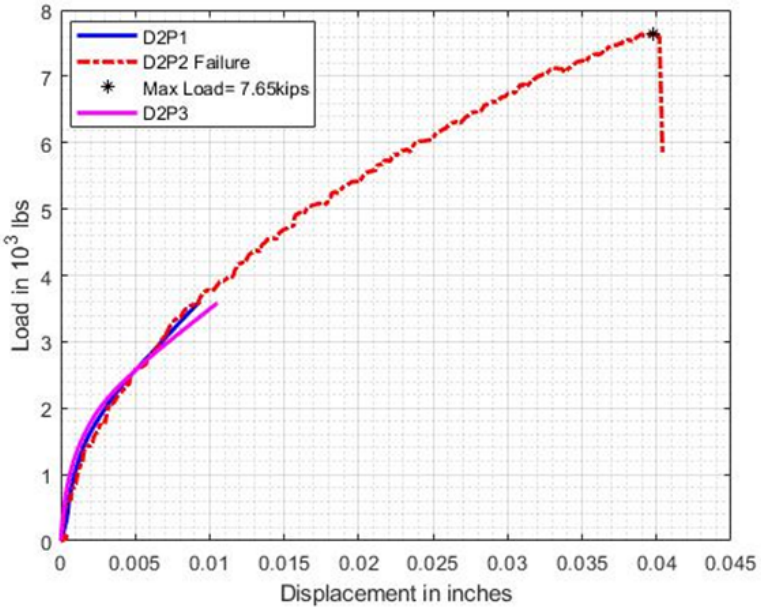

Figure 4.29: Summary of load (in $10^3 lbs$) v/s load point displacement (in inches) for Design #2

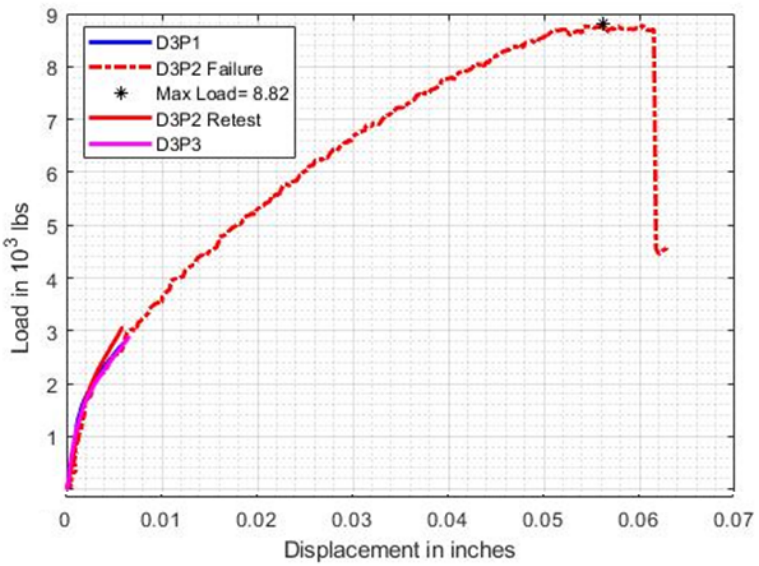

Figure 4.30: Summary of load (in $10^3 lbs$) v/s load point displacement (in inches) for Design #3

CHAPTER V

Computational Models for Response of Optimal Manufactured Plates Under In-plane Compression

A computational framework for predicting the behavior of *"as- manufactured"* panels with optimum distribution of the steered fibers was developed. This closely follows the pixelated Finite Element (FE) model that was developed for calculating the buckling loads and global stiffness during the optimization set up. The general schematic of loads and boundary conditions is shown in Figure 5.1

5.1 Updated Pixelated FE model

A python based code is written to create a pixelated FE mesh of size 20 in $\times$ 20 in with a 200 $\times$ 200 grid. This creates 20000 elements with 40401 nodes, each having three translational and two rotational degrees of freedom. The elements are first created for a flat plate. Using the information from Equation 4.3, the top and bottom surfaces are separated from the CMM data and an average least squares surface fit for the *"as- measured"* bottom surface is obtained as shown in Equation 5.1. The coefficients for least squares surface fit for Design #1 Panel # are also summarized.

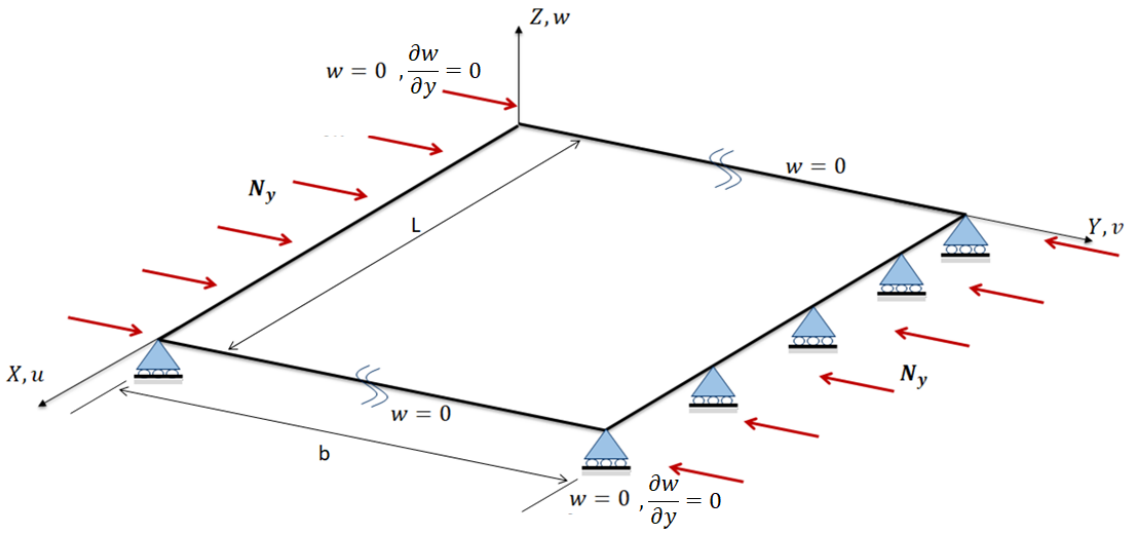

Figure 5.1: Schematic diagram showing Loading and Boundary condition

$$z(x,y) = p_{00}+p_{10}x+p_{01}y+p_{20}x^2+p_{11}xy+p_{02}y^2+p_{30}x^3+p_{21}x^2y+p_{12}xy^2+p_{03}y^3 \quad (5.1)$$

where,

$$p_{00} = 12.61 \quad p_{10} = -0.06987$$
$$p_{01} = -0.003525 \quad p_{20} = 6.553 \times 10^{-05}$$
$$p_{11} = 6.086 \times 10^{-05} \quad p_{02} = 2.431 \times 10^{-05}$$
$$p_{30} = 1.52 \times 10^{-08} \quad p_{21} = -6.84 \times 10^{-08}$$
$$p_{12} = -2.809 \times 10^{-08} \quad p_{03} = -2.125 \times 10^{-09}$$

The z co-ordinates of each node is then corrected by the surface fit of the bottom surface using Equation 5.1. This now creates a curved surface with a discrete mesh of composite shell elements of type S4 in Abaqus. Further, the centroid of each element is also computed. The element connectivity matrix remains the same for each of the

FE model as only nodal co-ordinates are changed using the computed curvature. Following the discussions in section 3.3.1, the creation of the FE model is implemented in a similar fashion. The algorithm is as summarized.

The data for curved fiber lay-up used to program the machine is available as course centerlines. This centerline data consists of 5000 discrete points as fed into the machine. These discrete data points are used to create left and right course boundaries by computing the local fiber angle at each discrete point as,

$$tan \quad \alpha(x_n, y_n) = \frac{y_{n+1} - y_n}{x_{n+1} - x_n} \tag{5.2}$$

This is used to compute the normal direction β at each location as $\beta = \alpha + \frac{\pi}{2}$. A course width of $d = 4$ in is used for manufacture, thereby obtaining left boundary $(x_{L,n}, y_{L,n})$ and right boundary $(x_{R,n}, y_{R,n})$ as,

$$\begin{aligned} x_{L,n} &= x_n - \frac{d}{2} \times sin\beta \\ y_{L,n} &= y_n + \frac{d}{2} \times cos\beta \end{aligned} \tag{5.3}$$

$$\begin{aligned} x_{R,n} &= x_n + \frac{d}{2} \times sin\beta \\ y_{R,n} &= y_n - \frac{d}{2} \times cos\beta \end{aligned} \tag{5.4}$$

The left and right course boundaries are then used to create a closed polygon to represent each of the individual courses. Using this information, each element in the assembly is assigned a laminate stack up. For this, the closed polygons representing each independent ply is first overlaid on top of the FE mesh created. As explained before, these closed polygons may overlap with each other creating course overlaps,

or have locations that are not covered by any of these polygons thereby creating gap locations. For each element in each ply, the algorithm identifies whether the centroid lies within one, none or multiple courses. Once the course(s)/ gaps are identified, it is then added to the laminate stack up of each composite shell element.

To assign the thickness and angle for each ply in the composite shell element, firstly the course(s) at the element is identified as described above. If, at a given centroid location, only one course is identified then that layer is assigned the nominal thickness of a single ply 0.0075 in as provided by the manufacturer. If multiple courses are identified, each layer in the stack up for that ply, at the overlap location, is assigned 92% of the nominal thickness as computed in the microscopy study established in section 4.4. This is because, the thickness of overlap regions will not be multiples of the single ply thickness but a distribution that varies depending on factors such as ply location in the stacking, compaction pressure while curing etc. To assign the fiber angle for each ply, the algorithm searches for the nearest point to the cetroid among the centerline data provided to the RAFP machine, and assigns the angle corresponding to that point as computed using Equation 5.2.

For each panel that was tested, the corresponding CMM data was used to obtain the nodal points, and the machine input data is used to create the section information for composite shell sections in Abaqus. Further a mid-plane offset is allowed in the FE model so as to consider the shell section to be defined with respect to the bottom surface. This is to account for the fact that the actual manufactured panel has a smooth bottom (tool) surface, where as the variations of thickness due to overlaps and gaps are present only on the top (bagging) surface.

A static non-linear geometric analysis is then set up for an end loading of 0.01 in

in uniform end compression. The boundary conditions are illustrated in Figure 5.1. The loading edges are encastré and thereby,

At y=0, y=b

$$\begin{aligned} w &= 0 \\ \frac{\partial w}{\partial y} &= 0 \end{aligned} \tag{5.5}$$

The transverse edges are supported by knife supports and are modeled as idealized simply support conditions in the out of plane direction, thereby,

At x=0, x=L

$$w = 0 \tag{5.6}$$

5.2 Results

5.2.1 Design #1

The load v/s load- point displacement plots of both numerical and experimental results for Panels #1, #2 and #3 of Design #1 is shown in Figure 5.2, Figure 5.3 and Figure 5.4 respectively. The initial and post-buckling stiffnesses are indicated for the numerical results, along with the corresponding transition loads. The comparison of results for Design #1, panels #1, panel #2 and panel #3 is summarized in Table 5.1.

5.2.2 Design #2

The load v/s load- point displacement plots of both numerical and experimental results for Panels #1, #2 and #3 of Design #2 is shown in Figure 5.5, Figure 5.6 and Figure 5.7 respectively. The initial and post-buckling stiffnesses are indicated for the numerical results, along with the corresponding transition loads. The comparison of

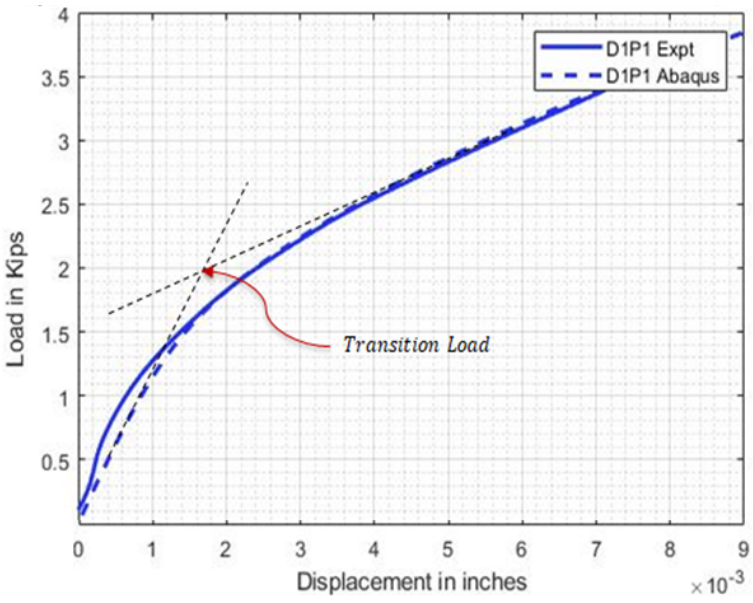

Figure 5.2: Load (in $10^3 lbs$) v/s load point displacement (in inches) for Design #1 Panel #1- Experimental and Numerical Results

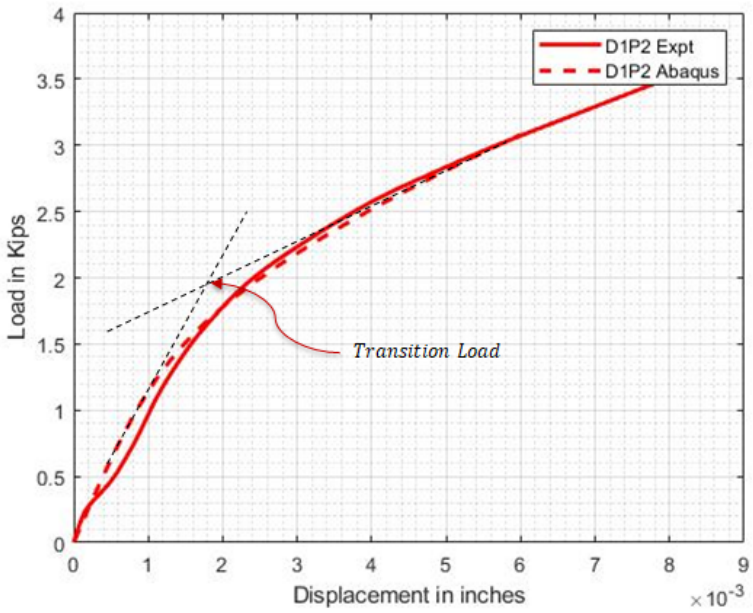

Figure 5.3: Load (in $10^3 lbs$) v/s load point displacement (in inches) for Design #1 Panel #2- Experimental and Numerical Results

results for Design #2, panels #1, panel #2 and panel #3 is summarized in Table 5.2.

Table 5.1: Comparison of initial stiffness ($in10^6 lb/in$) and Transition Loads (in lbs) for Design #1

#	Initial Stiffness ($in10^6 lb/in$)	% error	Transition Loads (in lbs)	% error
$Panel\#1Experiment$	1.17		2100	
$Panel\#1FEA$	1.10	5.9%	2000	4.8%
$Panel\#2Experiment$	1.28		2100	
$Panel\#2FEA$	1.22	4.7%	2000	4.8%
$Panel\#3Experiment$	1.25		2000	
$Panel\#3FEA$	1.27	1.6%	1900	5%

Table 5.2: Comparison of initial stiffness ($in10^6 lb/in$) and Transition Loads (in lbs) for Design #2

#	Initial Stiffness ($in10^6 lb/in$)	% error	Transition Loads (in lbs)	% error
$Panel\#1Experiment$	1.12		1800	
$Panel\#1FEA$	1.10	1.7%	1850	2.7%
$Panel\#2Experiment$	1.31		2150	
$Panel\#2FEA$	1.33	1.5%	2100	2.3%
$Panel\#3Experiment$	1.23		2000	
$Panel\#3FEA$	1.16	5.7%	1950	2.5%

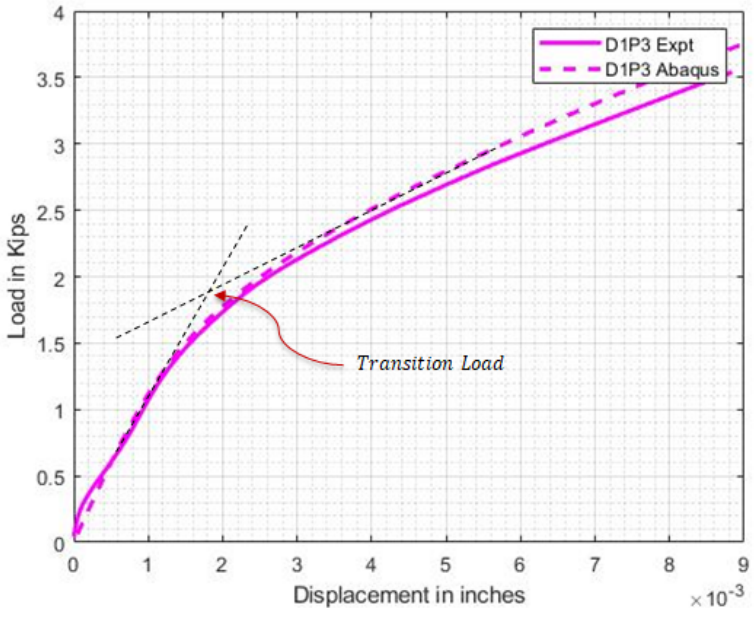

Figure 5.4: Load (in $10^3 lbs$) v/s load point displacement (in inches) for Design #1 Panel #3- Experimental and Numerical Results

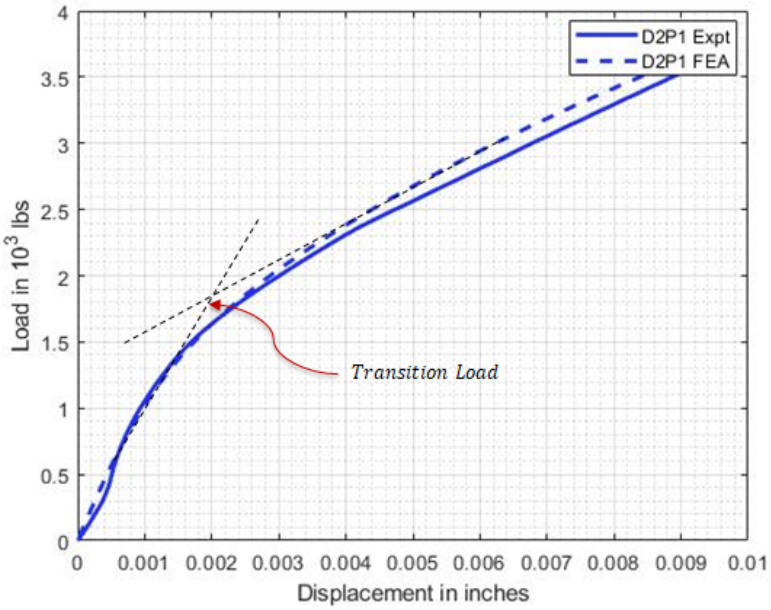

Figure 5.5: Load (in $10^3 lbs$) v/s load point displacement (in inches) for Design #2 Panel #1- Experimental and Numerical Results

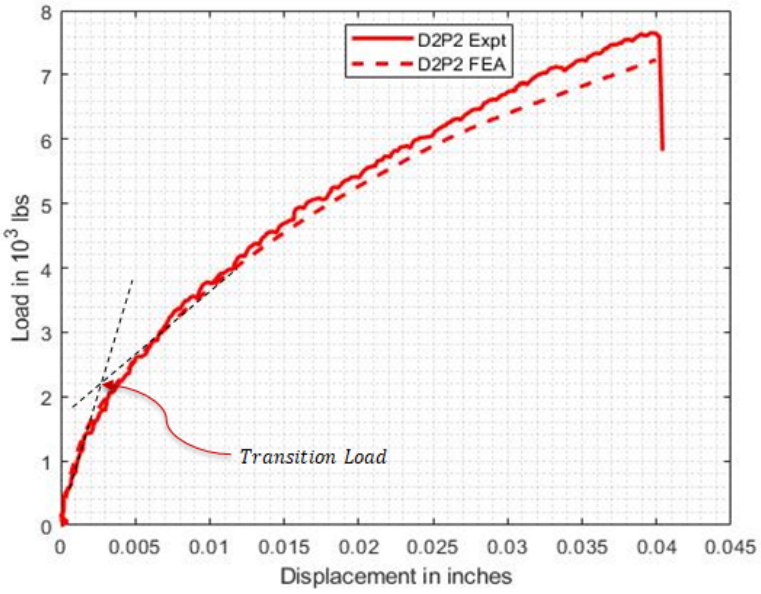

Figure 5.6: Load (in $10^3 lbs$) v/s load point displacement (in inches) for Design #2 Panel #2- Experimental and Numerical Results

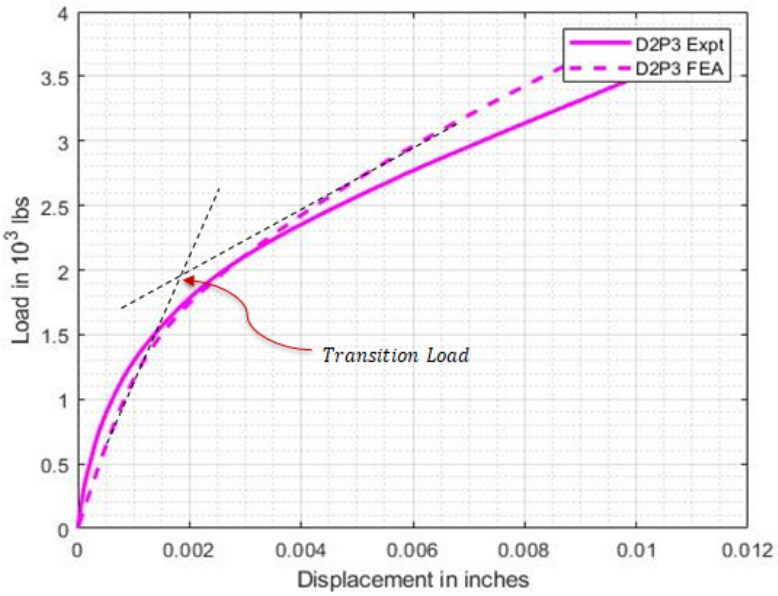

Figure 5.7: Load (in $10^3 lbs$) v/s load point displacement (in inches) for Design #2 Panel #3- Experimental and Numerical Results

5.2.3 Design #3

The load v/s load- point displacement plots of both numerical and experimental results for Panels #1, #2 and #3 of Design #3 is shown in Figure 5.8, Figure 5.9 and Figure 5.10 respectively. The initial and post-buckling stiffnesses are indicated for the numerical results, along with the corresponding transition loads. The comparison of results for Design #2, panels #1, panel #2 and panel #3 is summarized in Table 5.3.

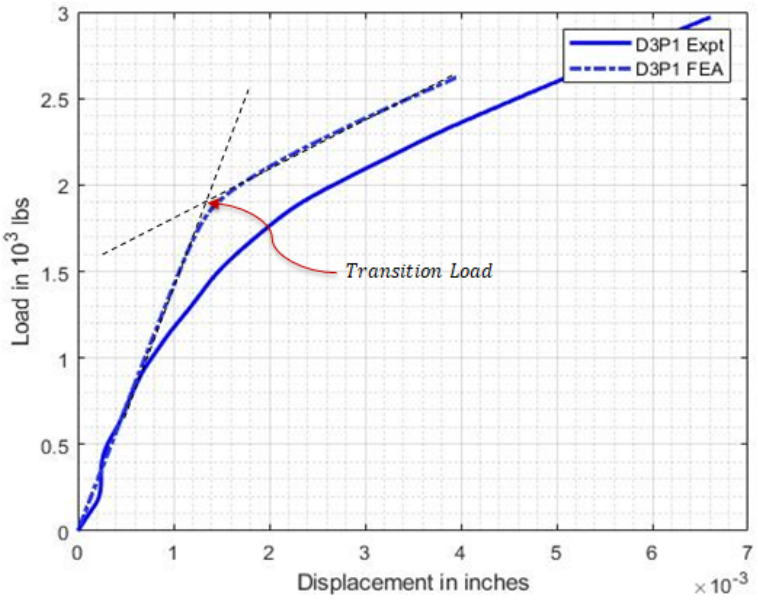

Figure 5.8: Load (in $10^3 lbs$) v/s load point displacement (in inches) for Design #3 Panel #1- Experimental and Numerical Results

5.3 Relaxation of loading edge Boundary Conditions

As observed from Table 5.3, the numerical simulations for Design #3, panel #1 and panel #3 are not in as good agreement as with the panel #2, with the experimental results. A reasonable assumption in this case could be the uncertainty in the enforced boundary conditions. Even though the edges that are potted with the steel

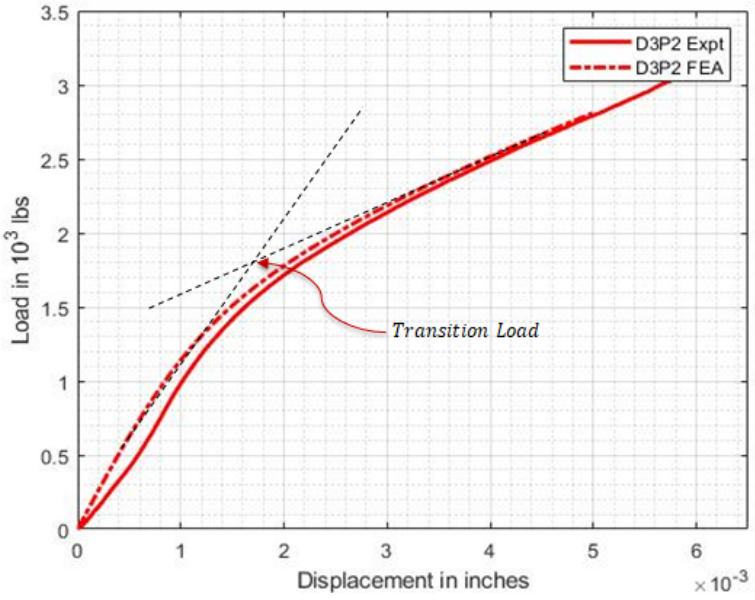

Figure 5.9: Load (in $10^3 lbs$) v/s load point displacement (in inches) for Design #3 Panel #2- Experimental and Numerical Results

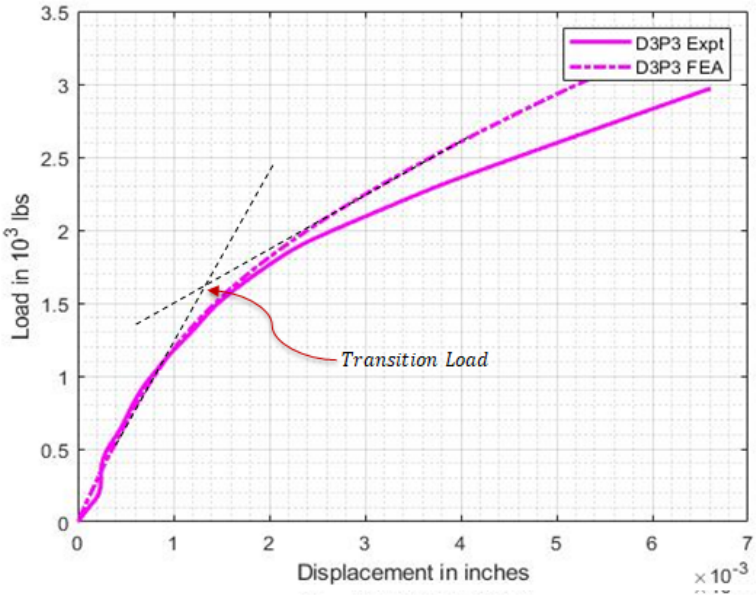

Figure 5.10: Load (in $10^3 lbs$) v/s load point displacement (in inches) for Design #3 Panel #3- Experimental and Numerical Results

Table 5.3: Comparison of initial stiffness ($in10^6 lb/in$) and Transition Loads (in lbs) for Design #3

#	Initial Stiffness ($in10^6 lb/in$)	% error	Transition Loads (in lbs)	% error
$Panel\#1Experiment$	1.18		1750	
$Panel\#1FEA$	1.33	12.7%	1900	8.6%
$Panel\#2Experiment$	1.16		1900	
$Panel\#2FEA$	1.12	3.4%	1800	5.3%
$Panel\#3Experiment$	1.08		1800	
$Panel\#3FEA$	1.10	1.85%	1600	11.1%

putty resembles an encastred boundary condition, voids or incomplete filling of the cavity might lead to formation of pockets of no contact between the specimen and the putty. Effect of these voids vary from specimen to specimen and might not be severe in most cases. The effect of such voids can be captured by relaxing the boundary conditions along the loading edges. The boundary conditions as illustrated in Figure 5.1 are now altered as shown in Figure 5.11. Instead of the assumption $w = 0$ at $y = 0$, $y = b$, a set of linear springs with a stiffness K are attached in the out-of-plane direction. Thus, the boundary condition $w = 0$ is replaced by $V_y = K.w(x, y = 0)$ and $V_y = K.w(x, y = b)$. Similarly, a set of rotational springs of stiffness K_θ are attached in the rotation along the y axis, such that the boundary condition $\frac{\partial w}{\partial x} = 0$ is now replaced by $M_y = K_\theta \frac{\partial w}{\partial x}$ at y=0,b.

The uncertainty in the boundary conditions can be captured by calibrating values of spring stiffnesses K and K_θ for individual cases until there is satisfactory matching of the numerical and experimental results.

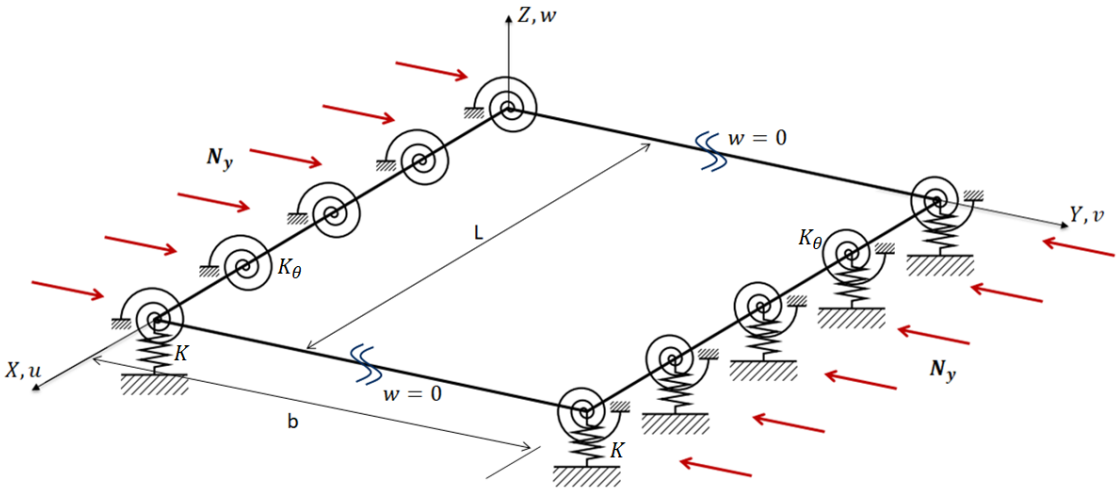

Figure 5.11: Schematic diagram showing modified Boundary Conditions along the loading edges to account for the relaxation of encastred condition due to voids in the putty region

Table 5.4: Comparison of initial stiffness ($in10^6 lb/in$) and Transition Loads (in lbs) for Design #3 using updated numerical models with relaxed loading edge boundary conditions

#	Initial Stiffness ($in10^6 lb/in$)	% error	Transition Loads (in lbs)	% error
$Panel\#1 Experiment$	1.18		1750	
$Panel\#1 FEA$	1.19	0.85%	1700	2.9%
$Panel\#3 Experiment$	1.08		1800	
$Panel\#3 FEA$	1.05	2.8%	1800	–

5.3.1 Updated numerical results for Design #3 Panel #1 and Panel #3

The load v/s load-point displacement plots for the numerical models with relaxed boundary conditions, compared to experimental results for Panels #1 and #3 of Design #3 is shown in Figure 5.12 and Figure 5.13 respectively. The initial and post-buckling stiffnesses are indicated for the numerical results, along with the corresponding transition loads. The comparison of results for Design #2, panels #1 and panel #3 is summarized in Table 5.4. The calibrated spring stiffness for each case is presented in Table 5.5 and Table 5.6

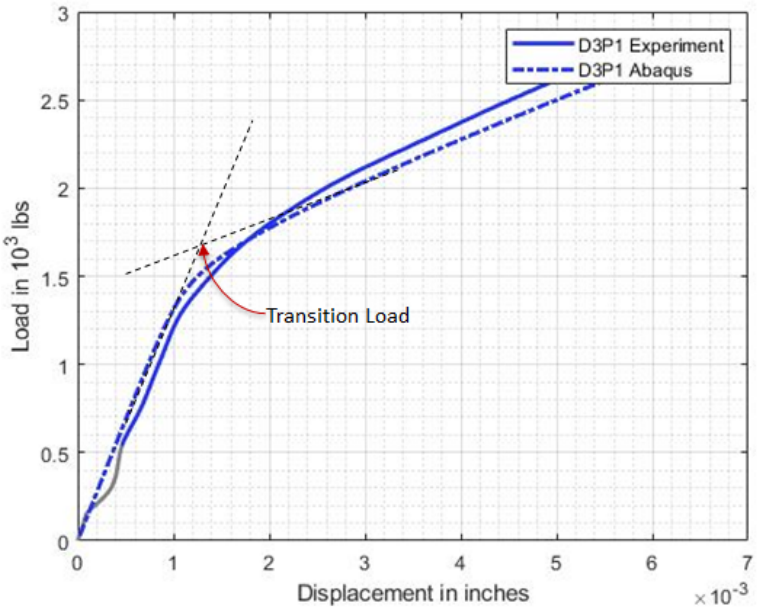

Figure 5.12: Load (in $10^3 lbs$) v/s load point displacement (in inches) for Design #3 Panel #1- Experimental and updated Numerical Results

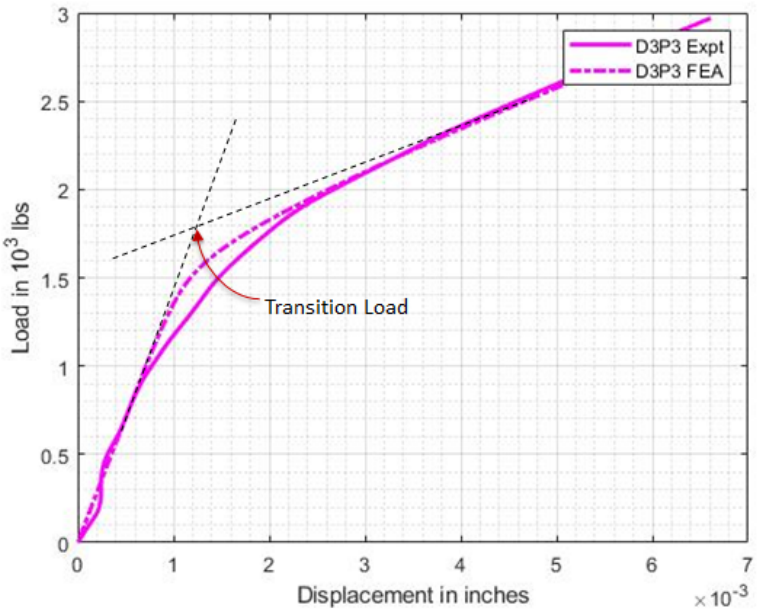

Figure 5.13: Load (in $10^3 lbs$) v/s load point displacement (in inches) for Design #3 Panel #3- Experimental and updated Numerical Results

Table 5.5: Calibrated linear and rotational spring stiffnesses for Design #3 Panel #1

Spring Stiffness	Value
Linear Spring, K	9200 lb/in
Rotational Spring K_θ	900 lb in/rad

Table 5.6: Calibrated linear and rotational spring stiffnesses for Design #3 Panel #3

Spring Stiffness	Value
Linear Spring, K	7800 lb/in
Rotational Spring K_θ	800 lb in/rad

5.4 Equivalent Straight Fiber Comparison

To validate the results of the experimental and numerical simulation against improvement of buckling/ transition load of an initially slightly curved panel with an equivalent straight fiber path, a simple optimization study is presented. This is necessary to have a sensible comparison of the manufactured 10 ply laminates against the best possible straight fiber paths that would maximize the critical buckling loads/transition loads.

Two such lay-ups are considered.

$$\text{Completely Free: } [0/(\theta_1/\theta_2)_2]_S$$

$$\text{Double-Double: } [0/(\pm\theta_1/\pm\theta_2)]_S$$

where, $-90^o \leq \theta_i \leq 90^o$.

The layups presented above are inspired from a new class of straight fiber laminates referred to as Double-Double (DD) which are usually of the lay-up $[\pm\theta_1/\pm\theta_2]_N$, and their combinations, where N could either be repeats of the fixed pattern $[\pm\theta_1/\pm\theta_2]$ or repeats with mid-plane symmetry. The prior work of the author published in *Vijay-*

achandran and Waas (2021) on DD class of laminates and their benefits compared to traditional quasi-isotropic laminates is presented in Appendix B, where more details of the DD lay-ups are provided.

An optimization problem is set up to maximize the buckling load of the two lay-ups discussed above. The angles represent the straight fiber angles of each layer. Hence, these θ_i's become the optimization variables. The bounds on the fiber angles are $-90^o \leq \theta_i \leq 90^o$. The mathematical representation of the optimization problem is given in Equation 5.7

$$\begin{aligned} \min_{X} \quad & (-N_{CR}) \\ \text{subject to} \quad & -90^\circ \leq \theta_i \leq 90^\circ \end{aligned} \tag{5.7}$$

where N_{CR} is the critical buckling load , θ_i, $(i = 1, 2)$ are the fiber angles.

To enable the recursive calculation of buckling load for a perfect structure during the optimization process, the python scripting feature of Abaqus is utilized. The curvature of Design #2 Panel#1 is chosen for the optimization. The nodes, element connectivity, material properties and load steps remain the same for each run of the optimizer. The panel is modeled as a perfect structure without any imperfections or eccentricity in the loading, therefore a linear buckling analysis can be performed. The aforementioned python scripting using Abaqus ensures that in each iteration of the optimization process, the corresponding angles/ optimization variables is passed to the code which writes an input file for the section details for an assembly of Abaqus Composite Shell S4 elements. A flowchart of the workflow during optimization is presented in Figure 5.14.

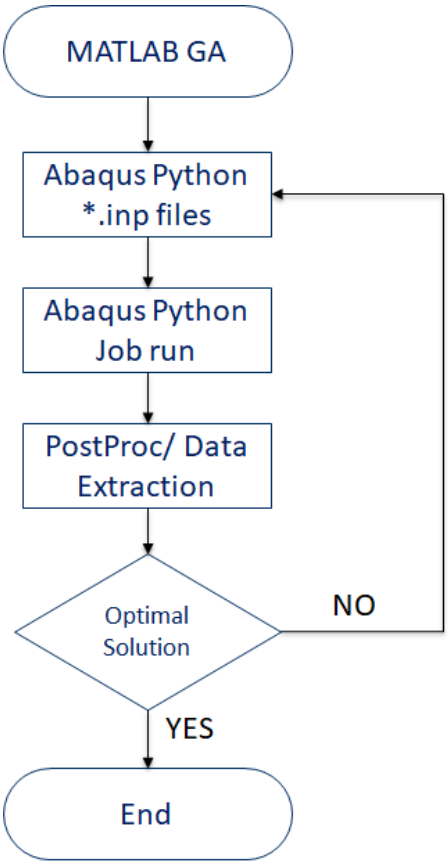

Figure 5.14: Flowchart of the optimization set-up

5.4.1 Computing Transition Loads

The optimal angles for a corresponding straight fiber lay-up in an initially slightly curved panel with no imperfections or eccentricity of loading is described in Table 5.7.

To obtain the transition loads for the two cases, the perfect, slightly curved panels are seeded with an initial geometric imperfection whose shape corresponds to a com-

Table 5.7: Optimal angles for equivalent straight fiber lay-up for an initially curved panel

#	Angles
CF: $[0/(\theta_1/\theta_2)_2]_S$	52°, 61°
DD: $[0/(\pm\theta_1/\pm\theta_2)]_S$	34°, −71°

bination of the first three mode shapes corresponding to the first three buckling loads of the perfect curved panel. Therefore, the lowest three eigen modes of the perfect structure is obtained from a linear buckling analysis is saved. This is then seeded on to the structure with significantly lower weights as magnitude (less than 1% of the thickness of the panel). The linear combination of the Eigen modes is assumed to mimic imperfections seen in the structures due to manufacturing. To obtain transition loads, a static non-linear geometric analysis is conducted. Load is applied as end shortening with the applied boundary conditions shows in Figure 5.15.

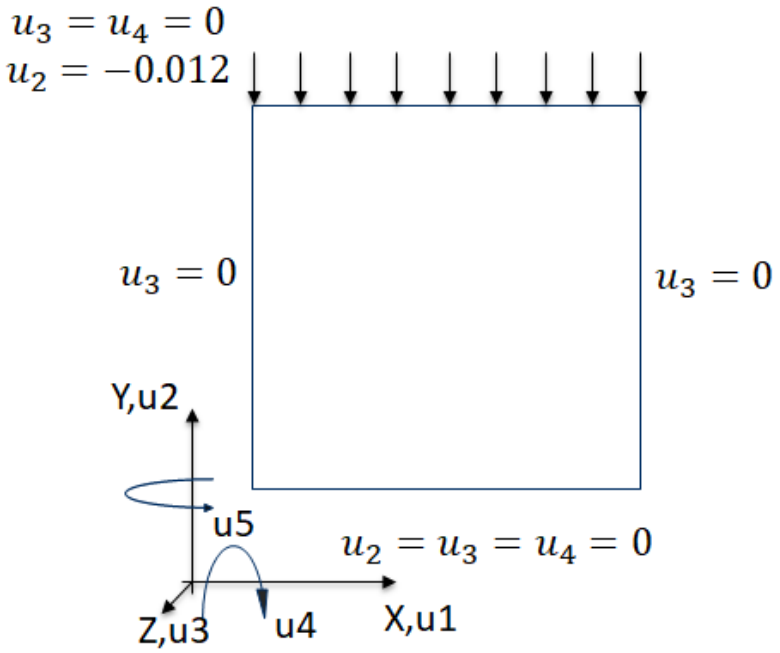

Figure 5.15: Boundary conditions for the static, geometric non-linear analysis

The load v/s load-point displacement for the two optimal cases are presented in Figure 5.16 and Figure 5.17. The computed transition load is tabulated in Table 5.8. In Table 5.8, the corresponding first three buckling loads of the perfect panel are also shown. The average transition load obtained from experimental testing of the optimally steered, RAFP manufactured panels are 2067 lbs, 1983 lbs and 1817 lbs

Table 5.8: Optimal layups and transition loads for equivalent straight fiber lay-up for an initially curved panel with imperfections

#	Lay-up	1^{st} eigen value	2^{nd} eigen value	3^{rd} eigen value	Transition Load (lbs)
CF:	$[0/(52°/61°)_2]_S$	1815	2208	2602	1600
DD:	$[0/(\pm 34°/\pm -71°)]_S$	1928	2412	2712	1650

for designs #1, #2 and #3 respectively. These are 25%, 20% and 10% higher than the corresponding straight fiber slightly curved panels that maximizes the transition load. Hence it could be concluded that steering the fibers contribute significantly to the improvement in buckling loads.

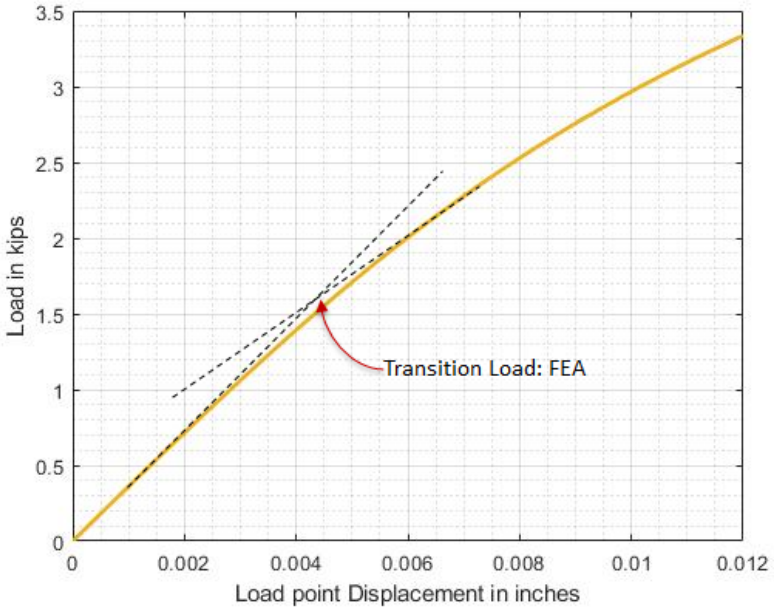

Figure 5.16: Load vs load-point displacement for completely free case

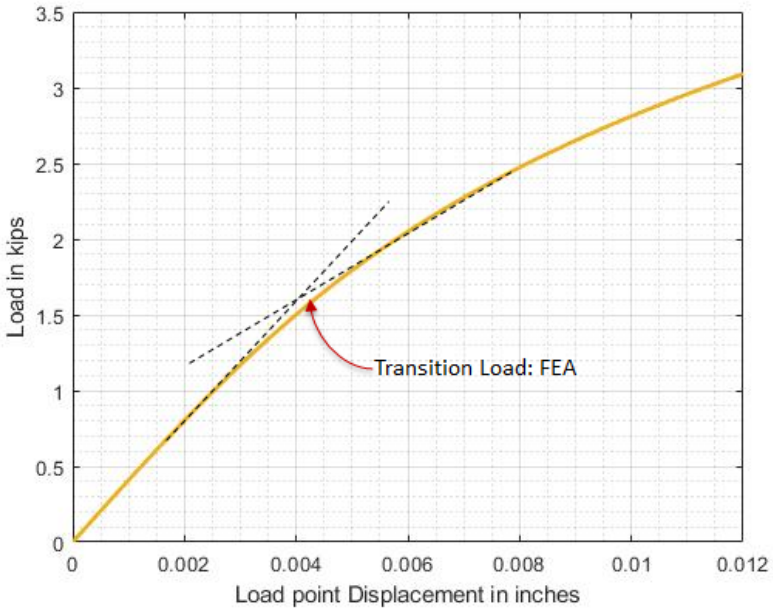

Figure 5.17: Load vs load-point displacement for DD case

CHAPTER VI

Minimizing Stress Concentrations Around Cutouts in Flat Laminated Plates Using Steered Fibers

Plate like components with cutouts are common in aerospace structures. There are many applications for such structures including, most commonly, windows in fuselage structure, as well as the less visible access ports for mechanical and electrical systems as well as lightening holes to reduce the total mass of the structure by removing material that does not carry any loads. Cutouts are used in interior hull of the fuselage as well as wing spars and ribs for providing access to control lines and for routine structural inspections.

Effect of cutouts in infinite plates under remote tensile loading is a classical problem in Elasticity. It is well known that the presence of a cutout acts as a stress raiser and causes significant stress concentrations (SC) around the cutout. An isotropic infinite plate with a central circular cutout under remote uni-axial in-plane tensile loading has a stress state that causes a stress concentration factor (SCF) of 3 around the cutout *Kirsch* (1898). This means that, the presence of the cutout alone causes three times the applied axial remote stress, at the location of the stress concentration.

A significant interest in the design problem of cutouts in aircraft structures arose

after multiple crashes of the De Havilland Comet aircraft in 1953-54 [*Cohen et al.* (1955)]. These jets were introduced to much fan fare as the world's first commercial jetliner. The early hull losses of these aircraft were due to the presence of rectangular windows with sharp corners that acted as stress raisers, causing eventual failure due to fatigue. The concept of a neutral hole was first introduced by Mansfield around the same time *Mansfield* (1953). Mansfield proposed to restore the stiffness around the cutout in a flat plate so that the cut structure has a stress state resembling that of the uncut structure, or in other words, the structure is unaware of the presence of a cutout.

With the increased use of composite materials in aerospace structures, effect of stress raisers became of utmost importance. The coupling effect of normal and shear strains and bending and twisting can cause significant increase in the SCF around cutouts in CFRP laminates. The idea of neutral holes was revisited in *Senocak and Waas* (1992) and, *Senocak and Waas* (1993), by proposing to nullify the effect of SCF around cutouts in orthotropic composite laminates. The study considered the bending- stretching coupling to design the shape of the cutouts as well as stiffeners around them to minimize the SCF. These studies minimized the stress concentration by adding material to the original structure (stiffeners around the cutout).

One of the first proposed study on using steered fiber paths for composite laminates dealt with the study of plates with cutouts [*Hyer and Lee* (1991)] as discussed in Chapter 2. As discussed earlier, the advent of AFP has made it easier for considering realizable steered fiber paths to minimize SCF around cutouts.

The work presented here is motivated by the idea of steering the fibers in a cut structure, so that without adding any material, the possibility of reducing the stress concentration around a cutout is re-examined. The hypothesis is that local stiff-

ness tailoring can lead to favorable internal stress states that reduce stress gradients, thereby minimizing stress concentration. Therefore, optimizing the spatially varying fiber courses in a 10-ply laminate of the lay-up $[0/(\theta_1/\theta_2)_2]_S$ where $\theta_1 = \theta_1(x, y)$ and $\theta_2 = \theta_2(x, y)$ is considered. The zero plies in the stack up is to ensure tackiness during the lay-up process as identified as a constraint in Chapter 4. Further, manufacturing parameters like course width and radius of curvature is explicitly included, as well the effect of manufacturing signatures like gaps and overlaps. An extension of the algorithm discussed in Chapter 3 is proposed to create a numerical model.

6.1 Problem Statement

A rectangular flat panel of size 24 in $\times$ 72 in is considered with a centrally placed elliptical cutout. The major axis of the cutout is aligned along the longer dimension of the plate and is of length 18 in, with a minor axis dimension of 11 in. These values represent the exact dimensions of a window to window repeated section of a Boeing 787 aircraft, except that the curvature of the fuselage is not considered for this study. A uni-axial displacement load is considered as shown (see Figure 6.1). The plate is simply supported along the shorter edges. RAFP compliant Toray T800/3900S material system is used for the analysis. The properties are provided in Table 6.1

The aim of the study here is to obtain optimal steered fiber paths that are allowed to vary spatially so as to minimize the stress concentrations around the cutout under the uni-axial loading that is applied. Due to symmetry of loading and geometry, only a quarter of the plate needs to be analyzed by imposing symmetry boundary conditions at $x = 0$ and $y = 0$. The symmetry conditions are shown in Figure 6.2

Table 6.1: Material Properties of T800/3900B

Property	Value	Unit
E_{11}	21.5	Msi
E_{22}	1.23	Msi
ν_{12}	0.329	
G_{12}	0.571	Msi

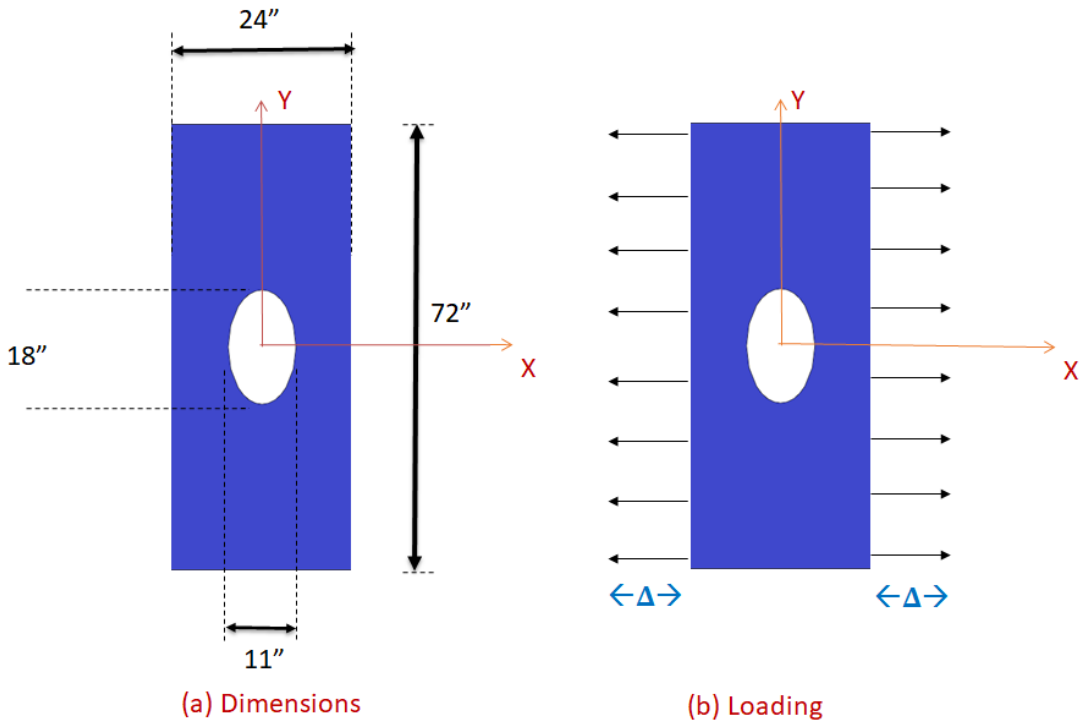

Figure 6.1: (a) Dimensions of the plate , (b)Uni-axial tensile loading

6.2 Manufacturing Considerations

In manufacturing a plate with a hole, there could be two possible manufacturing methods as shown in Figure 6.3 and Figure 6.4. Either there could be continuous placement of courses while manufacturing and then cut the part out at the location of the cut-out. Alternatively, fibers can be placed around the location of the cut-out [*Vijayachandran et al.* (2017)].

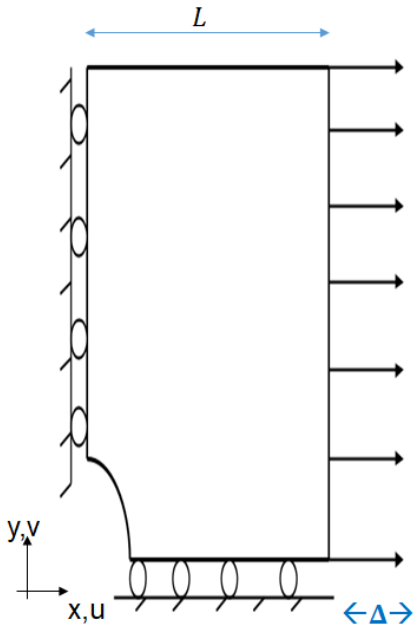

Figure 6.2: Symmetry boundary conditions

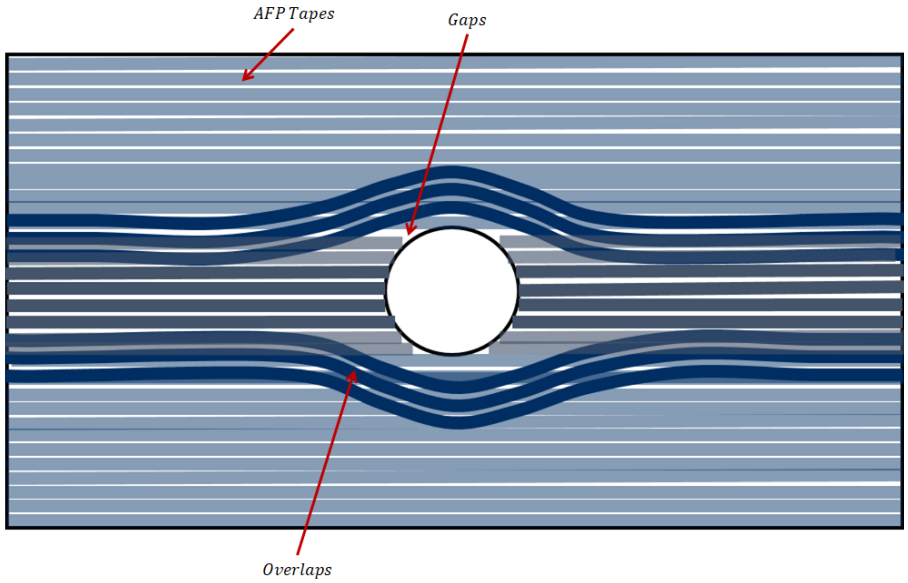

Figure 6.3: Schematics of tow placement around a cut-out location

6.2.1 Modeling Fiber Paths

A parametric representation using Bézier curves is used for modeling fiber paths. By using Bézier curves, fiber continuity is ensured, and manufacturing parameters like course width and minimum radius of curvature constraints shall be directly im-

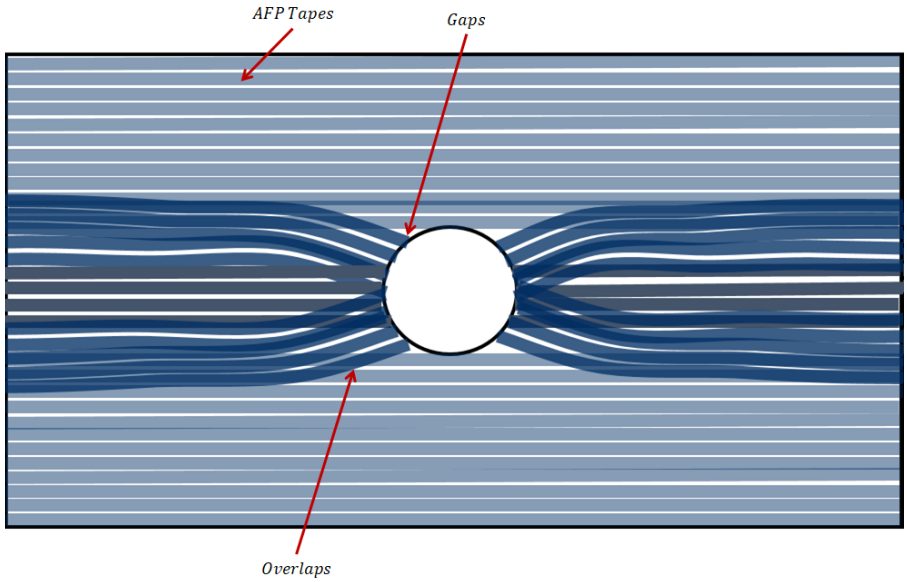

Figure 6.4: Schematics of tow placement ending at a cut-out location

plemented [*Vijayachandran et al.* (2017)]. Using a parametric function to represent the tows, number of optimization variables to represent each path is also reduced. The general form the curves are as shown.

$$B(n,t) = \Sigma_{i=0}^{n} \binom{n}{i} C_i (1-t)^{n-i} t^i, \forall \quad 0 \leq t \leq 1 \tag{6.1}$$

Where $n = O+1$ if O is the order of the curve, C_i represents the co-ordinate of the i^{th} point on the curve. Specifically, cubic splines are used for modeling the fiber paths, and shall be expressed as,

$$x(t) = x_1(1-t)^3 + 3x_2t(1-t)^2 + 3x_3t^2(1-t) + x_4t^3, \forall \quad 0 \leq t \leq 1 \tag{6.2}$$

$$y(t) = y_1(1-t)^3 + 3y_2t(1-t)^2 + 3y_3t^2(1-t) + y_4t^3, \forall \quad 0 \leq t \leq 1 \tag{6.3}$$

Where x_i and y_i $(i = 1, 2, 3, 4)$ are the co-ordinates of the control points.

6.2.2 Parametrization of fiber paths

As discussed earlier, cubic Bezier splines are used to represent the centerlines of the fiberpaths, thereby having 4 control points per course centerline, resulting in 8 co-ordinates per course as optimization variables. The concept of "global manufacturing mesh" as described in Chapter 3 is used to represent the optimization variables for the problem, there by significantly simplifying the design space. This introduces an interpolation scheme which in turn represents each control of the control points of all the curves to lie of four different "locus curves". As explained in Chapter 3, the manufacturing mesh is completely independent of any structural analysis calculations using FEA, and is merely an interpolation scheme aimed as simplifying the representation of optimization variables.

The interpolation scheme using the manufacturing mesh is used to change the "nodal shifts" at the nodes of the manufacturing mesh for each iteration of the optimization process so as to obtain updated control points, there by changing the design of the steered paths. To this extend, firstly as design space is established. Given the center of the elliptical cutout in the quarter plate is at the center, the farthest point is at a distance $\sqrt{(12^2 + 36^2)}$, approximated to 40 inches. To allow for full coverage of the fibers, a, 80 in $\times$ 80 in design space is considered, split into three coarse manufacturing mesh elements as shown in Figure 6.5. Once again, the larger design space is purely intended for allowing the steered courses to fill the space of the quarter plate, in an actual manufacturing, only the course details within the actual plate matters, subject to the manufacturing constraint of adding 4-5 inches of material at the beginning and end of the course lay-up.

To fill the space, a total of 20 courses of width 4in each is placed along the vertical direction as shown in Figure 6.6. These straight fiber unidirectional (UD) paths

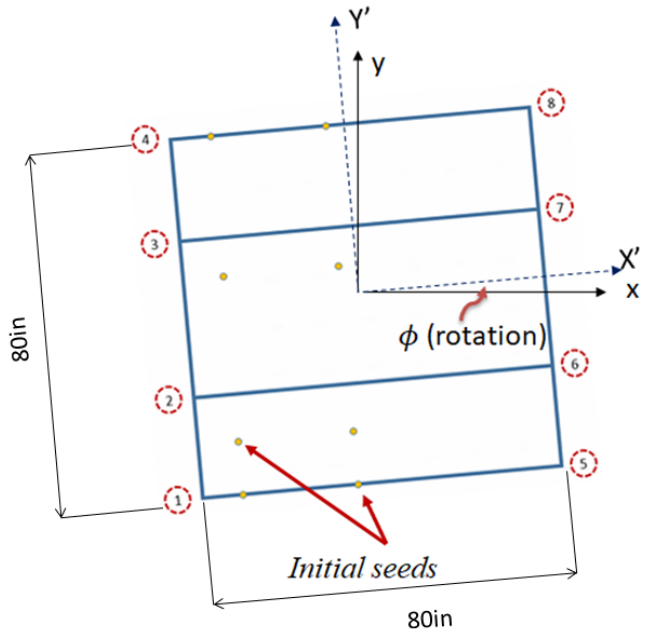

Figure 6.5: Initial seeds and Manufacturing global mesh for an $80in \times 80in$ design space

ensure full coverage of the design space and allows for no gaps or overlaps. These initial control points of UD paths are called "initial seeds" that represent the control points of B´ezier splines that are now collinear.

The nodal values of the manufacturing mesh as the nodal shift distances δ_x and δ_y. To incorporate the assumption that the machine is to start and end at the bottom and top edges of the manufacturing mesh, the δ_y at these nodes 1, 4, 5, 8 are set to be zero. Furhter, both δ_x and δ_y at nodes 2, 3, 6, 7 are varied as shown in Figure 6.5.

This means, there is a total of 12 design variables/ optimization variables (DV) for each independent ply. Further, to allow for additional degree of freedom, the manufacturing mesh can also be rotated with respect to the $x-y$ co-ordinate system by an angle ϕ as shown in Figure 6.5, making that an additional DV for steering the courses. Thus, having two independent plies in the design $[0/(\theta_1/\theta_2)_2]_S$, there are 26

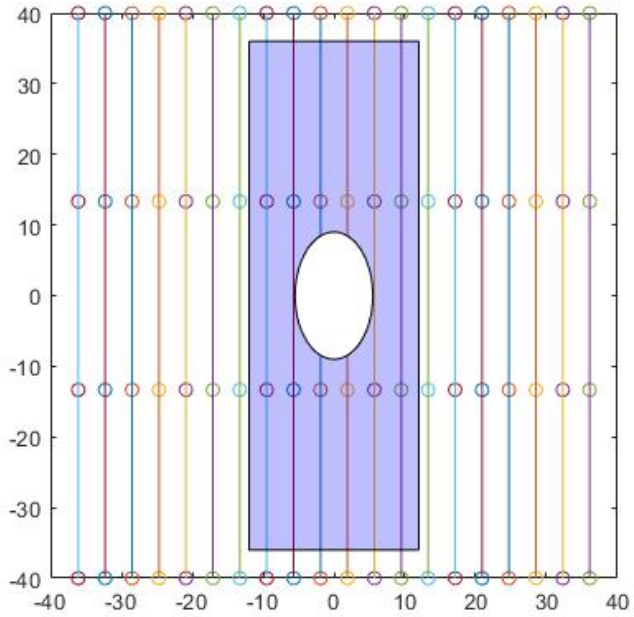

Figure 6.6: Centerlines of initial paths showing initial seeds superimposed over the actual panel

DVs, namely, 12 nodal variables and one angle of rotation per ply.

The values of nodal shifts can be used as optimization variables for varying the design in each iteration. The values of nodal shifts shall be interpolated to the initial seeds and the coordinates of the seeds shall be moved to $(x_i + \Delta x_i, y_i + \Delta y_i)$ to obtain the updated Bezier control points for the centerline of each course. Here (x_i, y_i) are the initial co-ordinates of the seed 'i' and $\Delta(x_i, y_i)$ is the shift interpolated from the nodal values. The initial seeding points (shown for two courses in Figure 6.5) of all the cubic splines lie within the three elements and are collinear. The nodal variables at the manufacturing mesh nodes are then interpolated to the initial seed locations to get new designs in each iteration as explained. An example of how the initial seeds are shifted to derive new steered fiber paths, is illustrated in Figure 6.7.

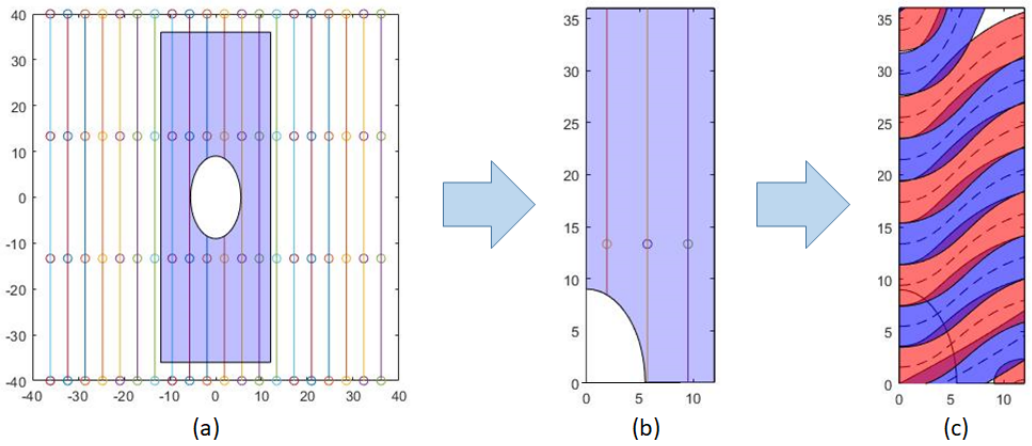

Figure 6.7: Varying steered fiber courses in a design (a) Initial seeds (b) Initial seeds and UD fibers in the actual panel area (c) Paths steered by varying the initial seeds with interpolated shift distances.

6.3 Finite element model

A MATLAB®based code is written to create a structured quadrilateral finite element mesh of shell type S4R elements in Abaqus (Figure 6.8) . To proceed, the code then identifies for each element, on each independent ply in the stack, number of courses that passes through the element centroid. The algorithm is explained as follows.

For each independent ply in the stack, the optimizer as explained in the previous section creates Bézier splines to represent center-lines of each course. The manufacturing parameter of course width w is used to create left and right boundaries of each of the courses. A closed polygon is created using the course boundaries and the edges of the physical plate. The number of closed polygons obtained would thus be N_s , which is the number of splines. These closed polygons are then superimposed on the finite element mesh. In doing so, some of the adjacent closed polygons may overlap (creating the overlap locations), or there may be empty spaces not covered by any of these polygons (thereby creating gap locations). At the centroid of each

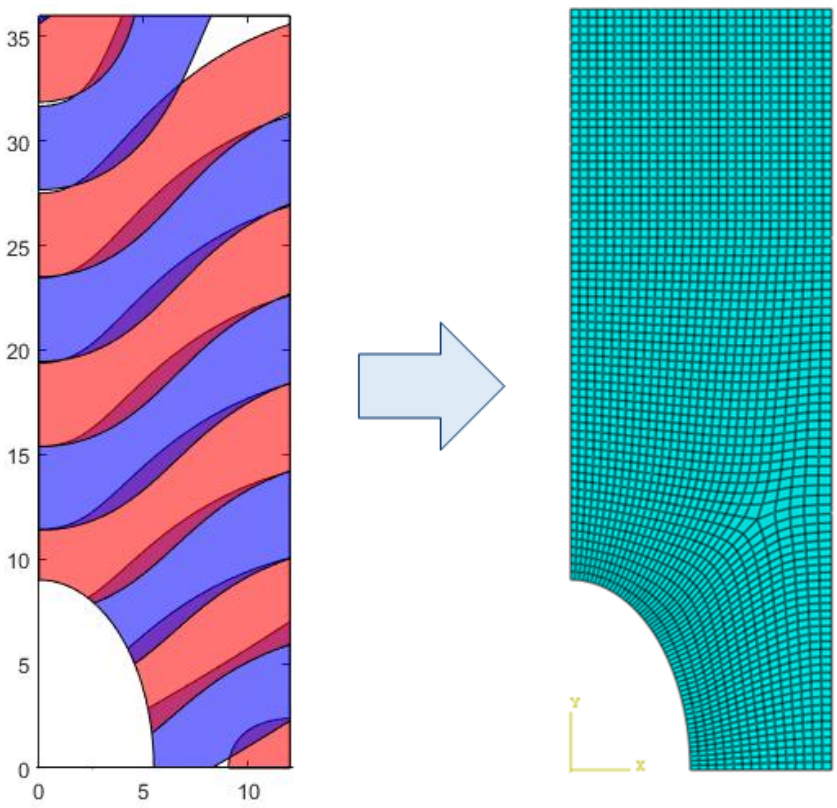

Figure 6.8: Structured quadrilateral mesh

element, the algorithm identifies if it lies with in one or more closed polygons. If so, the corresponding course is added to the stack up of that element. If not, pristine matrix properties are assigned.

In identifying the stackup, if only one course is identified at an element centroid, a single ply of nominal thickness 0.0075 in is added. To assign the angle, the algorithm searches for the point on the center-line of the corresponding course that is closest to the centroidal location, and assigns the angle at that point. If multiple courses are identified, each of them are assigned 92% thickness. This is based on previous experimental studies presented in Chapter 4, which identified that thickness of overlap regions will not be multiples of the single ply thickness but a distribution. Angles for each layer is assigned as explained above. Further a mid-plane offset is allowed in the FE model so as to consider the shell section to be defined with respect to the bottom surface. This is to account for the fact that the actual manufactured panel has a

smooth bottom (tool) surface, where as the variations of thickness due to overlaps and gaps are present only on the top (bagging) surface.

The FE model is verified for the case of a UD composite under uniaxial loading by comparing to a standard Abaqus simulation using composite shell elements.

6.4 Optimization Set-up and Surrogate Models

Mathematical representation of the optimization problem is as follows.

$$\begin{aligned} \min_{X} \quad & (K_T = \frac{SCF}{SCF_{QI}}) \\ \text{subject to} \quad & X_L \leq X \leq X_U \end{aligned} \tag{6.4}$$

where SCF_{QI} is the Stress concentration factor of the standard Quasi-isotropic laminate of $[0/\pm 45/90]_S$, SCF is the Stress concentration factor of the design and, x_L and x_U are the bounds of the design space.

There are 13 optimization variables for each independent ply, as explained above, thus having two independent plies in the optimal stack up, there is a total of 26 optimization variables. To minimize the computational expense of running FE simulations during every iteration of the global optimization run, the use of a surrogate model is proposed. A MATLAB ®based Radial Basis Function (RBF) Neural Network is used to implement the same. RBF is a 3 layer feed forward neural network with one hidden layer and one output layer. The hidden layer performs a non linear transform of the input and the output layer is a limier combiner used to map the non-linear weights into the output or target space. The hidden layer consists of the neurons that uses the RBF (ϕ_i) as the activation functions. The most commonly used

RBFs are

$$\begin{aligned}
\text{Gaussian:} \quad & \phi(r) = e^{\frac{-r^2}{2\sigma^2}}, \text{where} \quad \sigma > 0 \\
\text{Generalized multi Quadratic Function:} \quad & \phi(r) = (r^2 + \sigma^2)^{\beta}, \text{where} \quad \sigma, \beta > 0 \\
\text{Generalized inverse multi Quadratic Function:} \quad & \phi(r) = (r^2 + \sigma^2)^{-\alpha}, \text{where} \quad \sigma, \alpha > 0 \\
\text{Thin plate splines:} \quad & \phi(r) = r^2 ln(r)
\end{aligned} \tag{6.5}$$

Within the MATLAB ®framework, orthogonal least squares (OLS) algorithm is used to assign the weights for the activation functions.

6.4.1 Sampling and Radial Basis Neural Function Network Model

The sampling for setting up the Radial basis Function Neural Network is performed using Sobol. Sobol is a stratified sampling technique that ensures that the samples are distributed over the entire design space and is considered marginally robust than Latin Hypercube Sampling (LHS) used in the previous study. For the initial sampling, a normalized design space is used $[0, 1]^{26}$ and then each optimization variable (each row of samples in $[X(4200, 26)]$ matrix) is mapped one on one to the design space using a linear transformation, using the corresponding upper and lower bounds. These 4200 samples are then used to create the FE model and compute the SCF for each design using a static analysis under uniform end loading of 0.1 inches. The computed SCF is then normalized by $SCF_{QI} = 5.6$, which is the Stress concentration factor of the standard Quasi-isotropic laminate $[0/\pm 45/90]_S$. These normalized values are stored as the output matrix $[Y(4200, 1)]$.

A flowchart for the implementation of the RBF based surrogate model in conjunction with the *'ga'* functionality in the MATLAB ®global optimization toolbox is shown in Figure 6.9. While the RBF tool is used to fit the neural network, a visu-

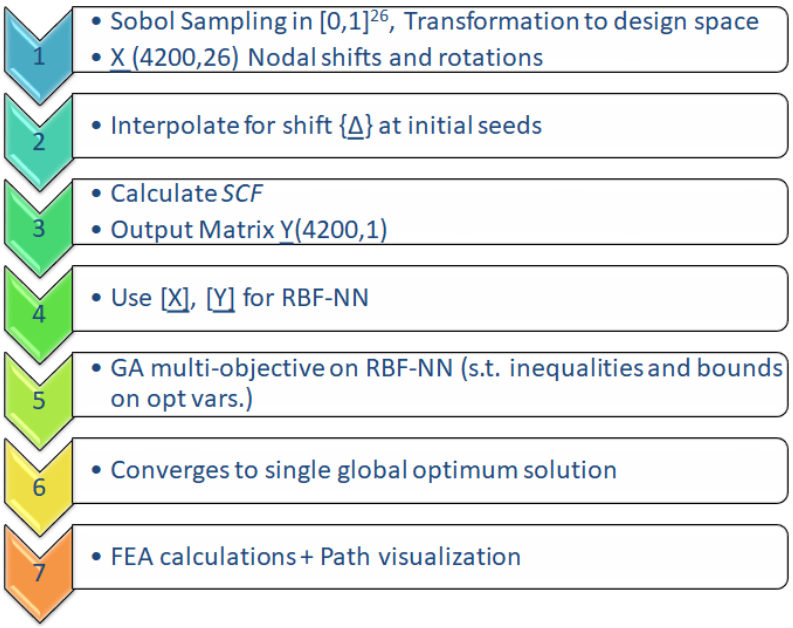

Figure 6.9: Flowchart for optimization methodology using surrogate model (RBF) and Genetic Algorithm

alization of the minimization of error (performance) is shown in Figure 6.10. A plot of targets (computed output values using SCF) v/s final RBF prediction is shown in Figure 6.11 which illustrates that the RBF is predicting a good fit for the data.

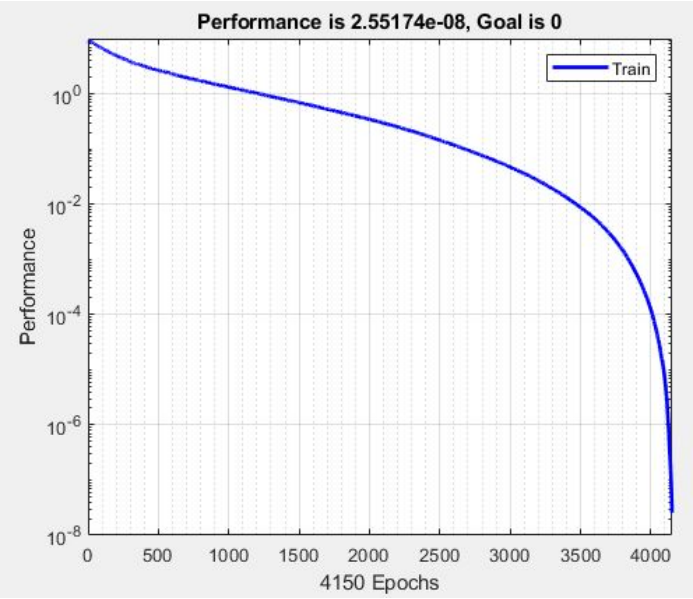

Figure 6.10: The minimization of error during Neural Network fitting using RBF

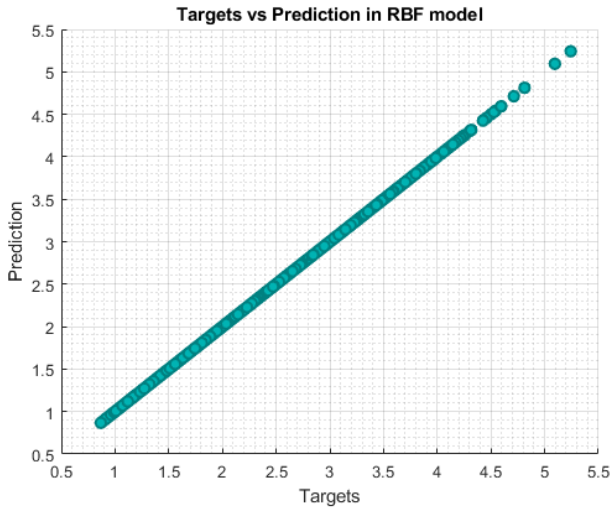

Figure 6.11: A plot of target (computed normalized SCF) v/s prediction using RBF

6.5 Results

The *'ga'* functionality in the MATLAB ®global optimization toolbox is used to run the optimization. The function converges to a single *'global optimum'* which produces a normalized SCF value of 0.679, corresponding to a SCF of 3.8. This is a reduction of 32.1% when compared to SCF value of 5.6 in a Quasi-isotropic $[0/\pm 45/90]_S$. The ply details of the two independent plies is shown in Figure 6.12. It is also to be noted that, though the individual plies might have gap locations, a full coverage of the space is ensured by the other plies in the stackup as shown in Figure 6.13. The variation of stress σ_{11} is shown in Figure 6.14

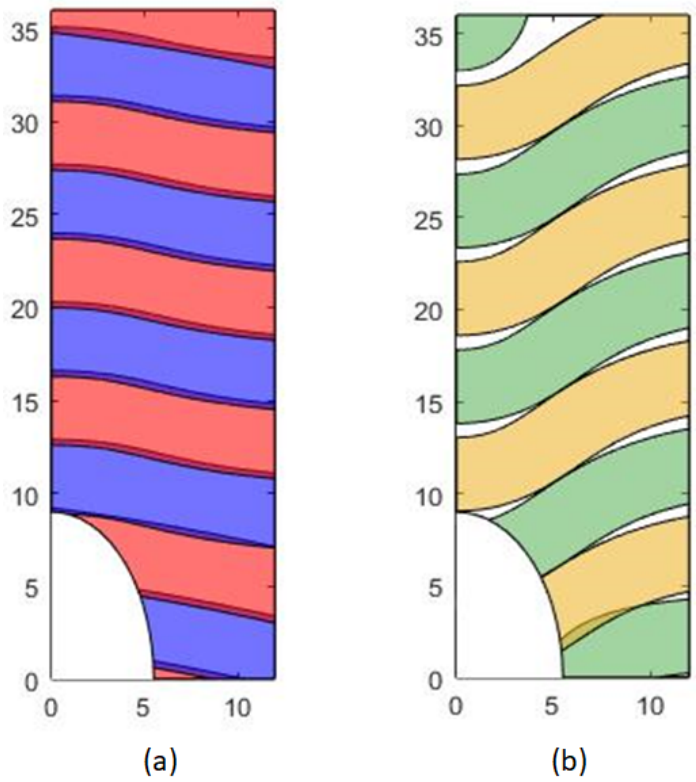

Figure 6.12: Variation of courses (a) Plies 2,4,7,9 (b) Plies 2,5,6,8

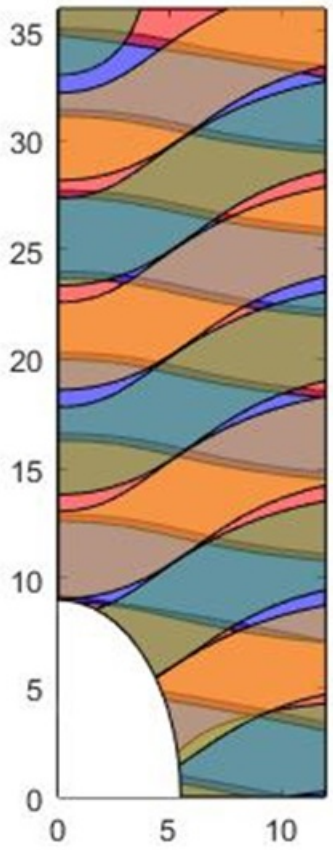

Figure 6.13: Variation of courses (a) Plies 2,4,7,9 (b) Plies 2,5,6,8

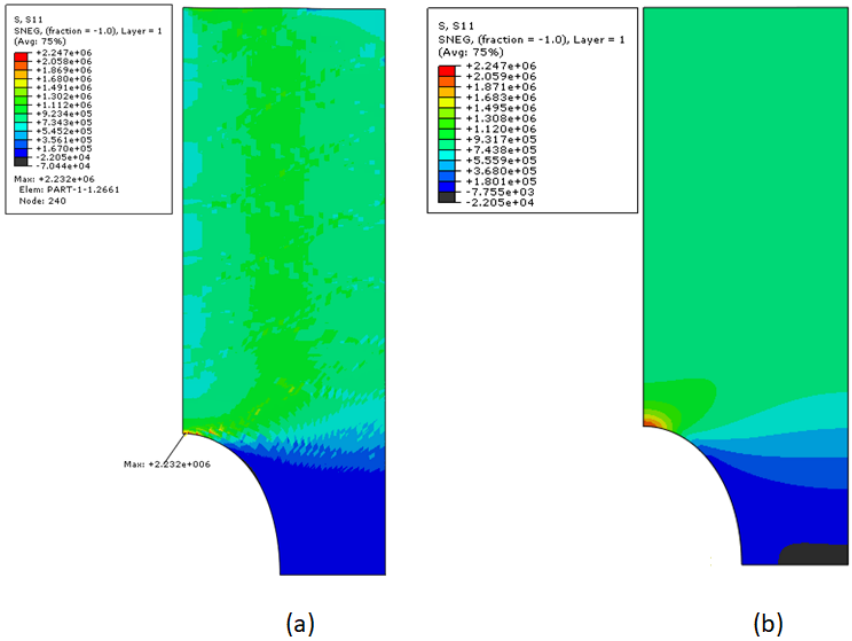

Figure 6.14: Contour of σ_{11} (a) Optimal solution (b) Quasi-isotropic $[0/\pm 45/90]_S$

CHAPTER VII

Conclusions and Future Work

7.1 Summary

Aerospace industry is significantly moving towards using fiber reinforced composites for design of new aircraft. This is evidenced by the fact that more than 80% by volume and 50% by weight in the latest of the commercial aircraft such as Boeing 787 dreamliner and Airbus A350 XWB is made of fiber reinforced composites. With the commercial aviation moving towards more point-to-point long distance flying as opposed to a traditional hub-and-spoke model, the industry is pushing for the development of lighter and narrow body long haul aircraft with increased range and fuel efficiency like the Boeing NMA (New Midsize Aircraft). The high strength to weight ratio of composites not only helps in the development of light weight aircraft but also contributes to significant reduction in the emission of green house gases, making aviation more sustainable. They are also the structural backbone of futuristic zero-emission and all-electric flights.

While many architectures of composite materials are available, such as chopped fiber composites, laminates, 2D and 3D braided composites, twills, woven composites among others, a majority of the aerostructural parts by volume are made of laminated tape composites. Additive manufacturing technologies like Robotic Automated Fiber

Placement (RAFP) and Automated Tape Laying (ATL) has significantly increased the efficiency of manufacturing such composite structures. These methods are faster and more efficient than traditional hand-layup and is well suited for manufacture of large parts with contours. In addition to the ease of manufacturing, RAFP also opens the avenue for structural design of laminates using fiber paths that are curvilinearly steered to optimize specific structural performance indices.

In this thesis, three design cases that are common in structural design are investigated- uni-axial and bi-axial compression of flat plates, and a rectangular flat plate with an elliptical hole under in-plane uni-axial tension. The objective of these numerical studies were to investigate optimal steered fiber paths that would maximize the buckling load in the case of in-plane compression and minimize the stress concentrations around the cut- out in the case of uni-axial tension while incorporating the effects of realistic manufacturing imperfections, referred to as manufacturing signature (MS). The manufacturing parameters like course width, number of tapes and minimum radius of steering etc. are first identified. It is also identified that manufacturing using RAFP and steering of fibers can cause imperfections like overlaps of adjacent courses and gaps between courses. They are collectively called manufacturing signature (MS).

Some of the salient features of this work includes the use of a novel method to represent the centerlines of the course paths using parametric curves called Bézier splines. Such a representation makes it easier to realize the optimization variables while explicitly ensuring that the fiber paths are always continuous. Further, the use of parametric curves also helps to incorporate manufacturing parameters such as course width and steering radius. In this study, each fiber path is designed to be steered independently and is mutually exclusive of how the adjacent course is steered.

A concept of *'global manufacturing mesh'* is introduced which helps to minimize the number of optimization variables. It also ensures that irrespective of the number of courses to model, the number of optimization variables remain the same. Further, by using manufacturing mesh, it ensures that no adjacent courses shall fully overlap or create large gaps. Deviating from prior literature, the effect of MS is explicitly included in this study by modeling the geometric changes in the plies at overlaps and gaps. This helps in the development of realistic and manufacturable designs that are not only optimized for the structural performance but also captures the effect of MS during manufacturing. An optimization workflow is developed that first creates a surrogate model based on Artificial Neural Networks (ANNs) or Radial Basis Function (RBF-NNs) and then use a global optimizer like genetic algorithm to obtain the optimal solution. Such a strategy makes the computations for optimization more efficient.

Once the optimal solutions were obtained, the designs maximizing uni-axial buckling performance were manufactured. Modifications are made for the designs to accommodate additional manufacturing constraint of having a straight fiber first ply, by laying down unidirectional 0^o first and last plies. This constraint was then included in the study to minimize stress concentrations around cut- outs. These panels were analyzed for manufacturing anomalies using non destructive inspection techniques such as CMM, microCT and optical microscopy. Testing fixtures for these panels are designed and they are tested for in-plane uni-axial compression in the laboratory. Numerical models were then developed to include the as- manufactured panels including the laid down fiber paths and the unintended slight curvature of the designs to predict the in-plane compression behavior. The numerical models were then modified to relax boundary conditions in the cases were there was more than 10% error in the computed structural performance indices. These changes are supported by observations during the experimental preparation that the loading edge boundary

conditions may from ideal clamped boundaries.

In addition, two appendices are presented. These explains the mathematical formulation for the pre- buckling and buckling equations of generalized flat laminates. A new class of laminates called DD is also introduced which vary from the traditional quasi- isotropic (QI) designs. It is established that optimized DD lay- ups using straight fibers are possible for specific loading cases and that these are superior than the QI laminates. Further, it is also established that the steering of fiber paths provide better structural performance than DD laminates.

7.2 Future Work

There are multiple directions for future work and continuation of research presented in this thesis. One major focus of interest would be to study the effect of specific course parameters like course width. With the available options, course widths can vary from 1 in to 4 in based on width of the tows and number of spools used in manufacturing. The minimum radius curvature shall also decrease as the course widths are reduced. Further, the sizes of overlaps and gaps shall also reduce with narrower courses. Thus, the optimal solutions for each of the design cases analyzed here will depend on this parameter. As mentioned earlier, the width of the course determines how many courses will be used to completely fill the design space. By using global manufacturing mesh, it is ensured that irrespective of the number of courses in the design, the number of optimization variables per independent ply remains the same.

The panels were designed to be flat in each of the design cases that were discussed. The manufactured panels though, had slight initial curvature. Thermal models in-

corporating the effect of thermal expansion coefficients during the different stages of the curing process will help to predict the final curvature of the parts. Such a model can be used within the optimization framework to neglect designs that will cause curvature beyond a set tolerance.

Further, as discussed in chapter 6, for design of a plate with a cutout, the manufacturing method modeled would place fibers emanating from the cutout. Such fiber paths shall either be cut and restarted at the cutout or they can be continuous, and the hole can be cutout after curing the final part. Similarly, investigating the alternative method of manufacturing by laying the fiber paths arounf the cutout shall produce different optimal design that the ones expected. It will be worthwhile to investigate which of these two methods shall produce better results to minimize stress concentrations.

Finally, failure analysis of steered fiber composites is an aspect lacking in the current literature. Finite element models to predict the failure loads and failure modes of such structures under different loading conditions including in-plane compression and tension, flexural loads and low velocity impact will produce significant contributions to this emerging field of *'Design for Manufacturing'* of RAFP manufactured composites.

APPENDICES

APPENDIX A

Buckling of generally layered laminated plates

Classical laminated plate theory (CLPT), that assumes linear material response, with Kirchoff-Love kinematics, is described in many textbooks related to the mechanics of laminated composite materials and structures [*Jones* (1973), *Reddy* (2003)]. For thin laminates, CLPT provides fairly accurate answers for buckling loads and free vibration frequencies, the latter being accurate for the lowest frequencies. First order shear deformation and high order shear deformation theories become preferred for higher vibration frequency estimates and for thicker laminates. In this note, the notions of buckling loads and transition loads for generally layered laminated plates are revisited.

A.1 Re-visiting Classical Laminate Plate Theory and Equations of Equilibrium

Figure A.1 illustrates the in-plane load and moment resultants in an infinitesimal element of a laminated composite plate. In CLPT, the relationship between Force and Moment resultants (N and M) and the mid-plane strains and curvatures (ϵ and χ) is given by Equation A.1 [*Reddy* (2003)]

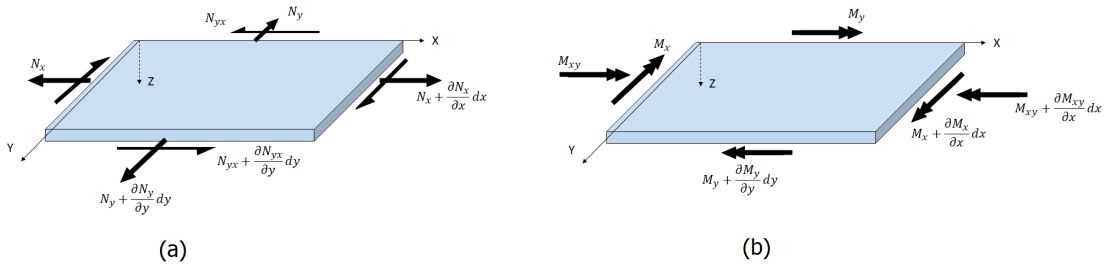

Figure A.1: (a) Force and (b) Moment resultants on an infinitesimal plate element.

$$\begin{Bmatrix} N \\ M \end{Bmatrix} = \begin{bmatrix} A & B \\ B & D \end{bmatrix} \begin{Bmatrix} \epsilon^0 \\ \chi \end{Bmatrix} \tag{A.1}$$

where,

A - Extensional stiffness matrix

B - Coupling (extensional-bending) stiffness matrix

D - Bending stiffness matrix

$$\begin{aligned} A_{ij} &= \sum_{k=1}^{n} \bar{Q}_{ij}^{k}(h_k - h_{k-1}) \\ B_{ij} &= \frac{1}{2}\sum_{k=1}^{n} \bar{Q}_{ij}^{k}(h_k^2 - h_{k-1}^2) \\ D_{ij} &= \frac{1}{3}\sum_{k=1}^{n} \bar{Q}_{ij}^{k}(h_k^3 - h_{k-1}^3) \end{aligned} \tag{A.2}$$

The definition of Von-Karman strains ϵ, and curvatures χ, expressed in terms of the mid-plane displacements, $u_0(x,y), v_0(x,y)$ and $w(x,y)$ is shown in Equation A.3

$$\begin{aligned} \epsilon_x(x,y,z) &= \frac{\partial u_0}{\partial x} - z\frac{\partial^2 w}{\partial x^2} + \frac{1}{2}\left(\frac{\partial w}{\partial x}\right)^2 = \epsilon_x^0 - z\frac{\partial^2 w}{\partial x^2} \\ \epsilon_y(x,y,z) &= \frac{\partial v_0}{\partial y} - z\frac{\partial^2 w}{\partial y^2} + \frac{1}{2}\left(\frac{\partial w}{\partial y}\right)^2 = \epsilon_y^0 - z\frac{\partial^2 w}{\partial y^2} \\ \epsilon_{xy}(x,y,z) &= \frac{\partial u_0}{\partial y} + \frac{\partial v_0}{\partial x} - 2z\frac{\partial^2 w}{\partial x \partial y} + \frac{\partial w}{\partial x}\frac{\partial w}{\partial y} = \epsilon_{xy}^0 - 2z\frac{\partial^2 w}{\partial x \partial y} \end{aligned} \tag{A.3}$$

$$\begin{Bmatrix} \chi_x \\ \chi_y \\ \chi_{xy} \end{Bmatrix} = \begin{Bmatrix} -\frac{\partial^2 w(x,y)}{\partial x^2} \\ -\frac{\partial^2 w(x,y)}{\partial y^2} \\ -2\frac{\partial^2 w(x,y)}{\partial x\ \partial y} \end{Bmatrix} \tag{A.4}$$

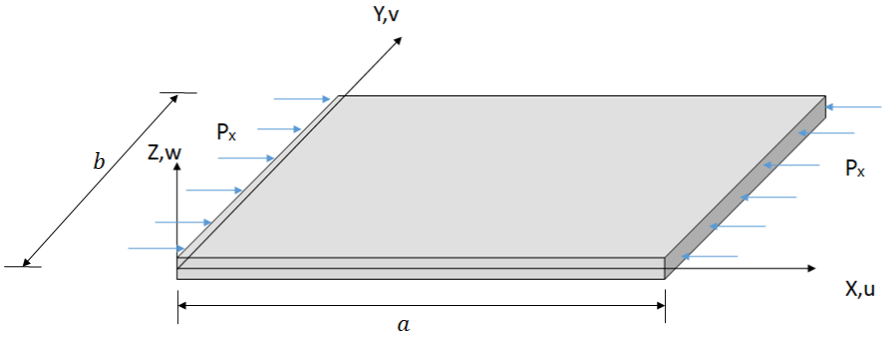

Figure A.2: Co-ordinates used with nomenclature for displacement components and applied uni-axial loading

Figure A.2 illustrates a uni-axially loaded flat plate. The laminate equilibrium equations and the associated variationally consistent boundary conditions can be obtained using variational principles, as shown in *Reddy* (2003), and are then written in the deformed configuration. This means that a general point on the mid-plane of the laminate can have non-zero axial displacements and out of plane displacements. Equation A.5, and Equation A.6, represents the in-plane equations of equilibrium and Equation A.7 represents the out of plane equation for equilibrium [*Reddy* (2003)], expressed in terms of stress and moment resultants.

$$\frac{\partial N_x}{\partial x} + \frac{\partial N_{xy}}{\partial y} = 0 \tag{A.5}$$

$$\frac{\partial N_{xy}}{\partial x} + \frac{\partial N_y}{\partial y} = 0 \tag{A.6}$$

$$N_x \frac{\partial^2 w}{\partial x^2} + 2N_{xy}\frac{\partial^2 w}{\partial x \partial y} + N_y \frac{\partial^2 w}{\partial y^2} + \frac{\partial^2 M_x}{\partial x^2} + 2\frac{\partial^2 M_{xy}}{\partial x \partial y} + \frac{\partial^2 M_y}{\partial y^2} = 0 \tag{A.7}$$

subject to variationally consistent boundary conditions, which for the purpose of this

note, are taken as simply supported on all edges.

At $x = 0$ and $x = a$

$$\begin{aligned} In - plane : N_x = -P_x \quad N_{xy} = 0 \\ Out - of - Plane : w = 0 \qquad M_x = 0 \end{aligned} \tag{A.8}$$

At $y = 0$ and $y = b$

$$\begin{aligned} In - plane : N_y = 0 \quad N_{xy} = 0 \\ Out - of - Plane : w = 0 \quad M_y = 0 \end{aligned} \tag{A.9}$$

A.1.1 Linearization using Adjacent Equilibrium Method

In observing Equation A.7, it is seen that the terms which appear as products of the in-plane resultants N_x, N_y and N_{xy}, and plate curvatures are non-linear, since the in-plane resultants are functions of the spatial partial derivatives of $w(x, y)$. Using the laminated plate constitutive relations, these equations can be expressed in terms of the mid-plane displacements. The resulting displacement equations of equilibrium are fully coupled because $[B_{ij}] \neq 0$.

Therefore, for a general laminate, a trivial solution $w = 0$ does not exist for all values of the applied in-plane loads and satisfying the boundary conditions . To proceed, the concept of a critical buckling load is based on a linear analysis. For this purpose, the governing equations need to be linearized. The procedure that is adopted is one that is commonly used in doing problems in shell theory [*Brush et al.* (1975), *Whitney* (2018)]

Consider the displacement field

$$\begin{aligned} u_0 &= u_0^i + \lambda u_0 \\ v_0 &= v_0^i + \lambda v_0 \\ w &= w^i + \lambda w \end{aligned} \tag{A.10}$$

where 'i' denotes pre-buckling displacements in the initial configuration and λ is an infinitesimally small, dimensionless quantity causing a slight perturbation to the equilibrium position. We seek a critical load that causes this infinitesimal shift in the equilibrium position. Thus, u_0, v_0 and w, appearing in Equation A.10 are the buckling displacements associated with the shift in the equilibrium position from the initial to the buckled.

A.1.2 Linearization of typical strain and curvature terms

Consider components of the mid-plane strains and curvatures as shown in Equation A.11,

$$\begin{aligned} \epsilon_x^0 &= \frac{\partial u_0}{\partial x} + \frac{1}{2}\left(\frac{\partial w}{\partial x}\right)^2 \\ \epsilon_{xy}^0 &= \frac{\partial u_0}{\partial y} + \frac{\partial v_0}{\partial x} + \frac{\partial w}{\partial x}\frac{\partial w}{\partial y} \\ \chi_x &= -\frac{\partial^2 w(x,y)}{\partial x^2} \end{aligned} \tag{A.11}$$

Then, we can express the perturbed strain as in Equation A.12 ,

$$\begin{aligned} \epsilon^0 &= \epsilon^{0i} + \lambda \epsilon^0 \\ \chi &= \chi^i + \lambda \chi \end{aligned} \tag{A.12}$$

Substituting Equation A.10 into Equation A.11 and Equation A.12, we obtain

$$
\begin{aligned}
\epsilon_x^0 &= \frac{\partial}{\partial x}(u_0^i + \lambda u_0) + \frac{1}{2}\left[\frac{\partial}{\partial x}(w^i + \lambda w)\right]^2 \\
\implies \epsilon_x^0 &= \frac{\partial u_0^i}{\partial x} + \lambda\frac{\partial u_0}{\partial x} + \frac{1}{2}\left[(\frac{\partial w^i}{\partial x})^2 + 2\lambda(\frac{\partial w^i}{\partial x}\frac{\partial w}{\partial x}) + \cancel{\lambda^2(\frac{\partial w}{\partial x})^2}^{H.O.T}\right] \\
\implies \epsilon_x^0 &= \underbrace{\left[\frac{\partial u_0^i}{\partial x} + \frac{1}{2}(\frac{\partial w^i}{\partial x})^2\right]}_{\epsilon_x^{0i}} + \lambda\underbrace{\left[\frac{\partial u_0}{\partial x} + (\frac{\partial w^i}{\partial x}\frac{\partial w}{\partial x})\right]}_{\epsilon_x^0}
\end{aligned}
\tag{A.13}
$$

Similarly,

$$
\begin{aligned}
\epsilon_{xy}^0 &= \frac{\partial u_0}{\partial y} + \frac{\partial v_0}{\partial x} + \frac{\partial w}{\partial x}\frac{\partial w}{\partial y} \\
\implies \epsilon_{xy}^0 &= \frac{\partial u_0^i}{\partial y} + \frac{\partial v_0^i}{\partial x} + \lambda\left[\frac{\partial u_0}{\partial y} + \frac{\partial v_0}{\partial x}\right] + \left(\frac{\partial w^i}{\partial x} + \lambda\frac{\partial w}{\partial x}\right)\left(\frac{\partial w^i}{\partial y} + \lambda\frac{\partial w}{\partial y}\right) \\
\implies \epsilon_{xy}^0 &= \underbrace{\left[\frac{\partial u_0^i}{\partial y} + \frac{\partial v_0^i}{\partial x} + (\frac{\partial w^i}{\partial x}\frac{\partial w^i}{\partial y})\right]}_{\epsilon_{xy}^{0i}} + \lambda\underbrace{\left[\frac{\partial u_0}{\partial y} + \frac{\partial v_0}{\partial x} + (\frac{\partial w^i}{\partial x}\frac{\partial w}{\partial y}) + (\frac{\partial w^i}{\partial y}\frac{\partial w}{\partial x})\right]}_{\epsilon_{xy}^0}
\end{aligned}
\tag{A.14}
$$

and,

$$
\begin{aligned}
\chi_x &= -\frac{\partial^2 w(x,y)}{\partial x^2} \\
\implies \chi_x &= -\frac{\partial^2}{\partial x^2}(w^i + \lambda w) \\
\implies \chi_x &= \underbrace{-\frac{\partial^2 w^i}{\partial x^2}}_{\chi_x^i} - \lambda\underbrace{\left[-\frac{\partial^2 w}{\partial x^2}\right]}_{\chi_x}
\end{aligned}
\tag{A.15}
$$

Now, to obtain the linearized form, the plate constitutive description Equation A.1 is used to arrive at,

$$
\begin{aligned}
N &= A\epsilon^{0i} + B\chi^i + \lambda(A\epsilon^0 + B\chi) = N^i + \lambda N \\
M &= B\epsilon^{0i} + D\chi^i + \lambda(B\epsilon^0 + D\chi) = M^i + \lambda M
\end{aligned}
\tag{A.16}
$$

Substituting Equation A.16 to Equation A.5, and separating out the terms with

like powers of λ we can arrive at,

$$\begin{aligned} &\frac{\partial}{\partial x}(N_x^i + \lambda N_x) + \frac{\partial}{\partial y}(N_{xy}^i + \lambda N_{xy}) = 0 \\ \implies &\underbrace{\left[\frac{\partial N_x^i}{\partial x} + \frac{\partial N_{xy}^i}{\partial y}\right]}_{pre-buckling} + \lambda \underbrace{\left[\frac{\partial N_x}{\partial x} + \frac{\partial N_{xy}}{\partial y}\right]}_{buckling} = 0 \end{aligned} \tag{A.17}$$

Similarly, Substituting Equation A.16 in Equation A.6,

$$\begin{aligned} &\frac{\partial}{\partial x}(N_{xy}^i + \lambda N_y) + \frac{\partial}{\partial y}(N_y^i + \lambda N_y) = 0 \\ \implies &\underbrace{\left[\frac{\partial N_{xy}^i}{\partial x} + \frac{\partial N_y^i}{\partial y}\right]}_{pre-buckling} + \lambda \underbrace{\left[\frac{\partial N_{xy}}{\partial x} + \frac{\partial N_y}{\partial y}\right]}_{buckling} = 0 \end{aligned} \tag{A.18}$$

and, substituting Equation A.16 to Equation A.7 then separating out the terms, neglecting H.O.Ts , we can arrive at Equation A.19. Since w^i, N_x^i, N_y^i and N_{xy}^i are obtained from the solution to the initial equilibrium position, Equation A.19 is linear. However, we still need to use the non-linear version of Equation A.7 to determine the initial configuration. At this stage, we make an assumption that linear theory be used to determine the solution corresponding to the initial equilibrium position. Since the initial configuration is determined from linear theory, the terms in Equation A.19 containing initial curvatures can be neglected.

$$\frac{\partial^2}{\partial x^2}(M_x^i + \lambda M_x) + 2\frac{\partial^2}{\partial x \partial y}(M_{xy}^i + \lambda M_{xy}) + \frac{\partial^2}{\partial y^2}(M_y^i + \lambda M_y)$$
$$+(N_x^i + \lambda N_x)\left[\frac{\partial^2}{\partial x^2}(w^i + \lambda w)\right] + (N_{xy}^i + \lambda N_{xy})\left[2\frac{\partial^2}{\partial x \partial y}(w^i + \lambda w)\right] + (N_y^i + \lambda N_y)\left[\frac{\partial^2}{\partial y^2}(w^i + \lambda w)\right] = 0$$

$$\Longrightarrow \underbrace{\left[\frac{\partial^2 M_x^i}{\partial x^2} + 2\frac{\partial^2 M_{xy}^i}{\partial x \partial y} + \frac{\partial^2 M_y^i}{\partial y^2} + N_x^i\frac{\partial^2 w^i}{\partial x^2} + 2N_{xy}^i\frac{\partial^2 w^i}{\partial x \partial y} + N_y^i\frac{\partial^2 w^i}{\partial y^2}\right]}_{pre-buckling} \tag{A.19}$$

$$+\lambda\left[\underbrace{\frac{\partial^2 M_x}{\partial x^2} + 2\frac{\partial^2 M_{xy}}{\partial x \partial y} + \frac{\partial^2 M_y}{\partial y^2} + N_x^i\frac{\partial^2 w}{\partial x^2} + 2N_{xy}^i\frac{\partial^2 w}{\partial x \partial y} + N_y^i\frac{\partial^2 w}{\partial y^2}}_{Buckling}\right]$$

$$+\lambda\left(N_x\frac{\partial^2 w^i}{\partial x^2} + N_{xy}\frac{\partial^2 w^i}{\partial x \partial y} + N_y\frac{\partial^2 w^i}{\partial y^2}\right) \xrightarrow{(\because \chi^i = 0)} + \lambda^2\left[N_x\frac{\partial^2 w}{\partial x^2} + 2N_{xy}\frac{\partial^2 w}{\partial x \partial y} + N_y\frac{\partial^2 w}{\partial y^2}\right] \xrightarrow{} H.O.Ts$$

Thus, Equation A.19becomes

$$\lambda\left(\frac{\partial^2 M_x}{\partial x^2}+2\frac{\partial^2 M_{xy}}{\partial x\partial y}+\frac{\partial^2 M_y}{\partial y^2}+N_x^i\frac{\partial^2 w}{\partial x^2}+2N_{xy}^i\frac{\partial^2 w}{\partial x\partial y}+N_y^i\frac{\partial^2 w}{\partial y^2}\right)=0 \tag{A.20}$$

Then, Equation A.20 together with equations Equation A.17 and Equation A.18 complete the governing equations for the stability (buckling) problem. The pre-buckling problem is governed by the three pre-buckling equations, Equation A.21, Equation A.22 and Equation A.23, as shown below.

$$\frac{\partial N_x^i}{\partial x}+\frac{\partial N_{xy}^i}{\partial y}=0 \tag{A.21}$$

$$\frac{\partial N_{xy}^i}{\partial x}+\frac{\partial N_y^i}{\partial y}=0 \tag{A.22}$$

$$\frac{\partial^2 M_x^i}{\partial x^2}+2\frac{\partial^2 M_{xy}^i}{\partial x\partial y}+\frac{\partial^2 M_y^i}{\partial y^2}+N_x^i\frac{\partial^2 w^i}{\partial x^2}+2N_{xy}^i\frac{\partial^2 w^i}{\partial x\partial y}+N_y^i\frac{\partial^2 w^i}{\partial y^2}=0 \tag{A.23}$$

However, since the initial prebuckling state is assumed to be associated with negligible initial curvatures, Equation A.23 reduces to Equation A.24

$$\frac{\partial^2 M_x^i}{\partial x^2}+2\frac{\partial^2 M_{xy}^i}{\partial x\partial y}+\frac{\partial^2 M_y^i}{\partial y^2}=0 \tag{A.24}$$

In terms of displacements, the buckling equations become,

$$A_{11}\frac{\partial^2 u_0}{\partial x^2} + 2A_{16}\frac{\partial^2 u_0}{\partial x \partial y} + A_{66}\frac{\partial^2 u_0}{\partial y^2} + A_{16}\frac{\partial^2 v_0}{\partial x^2} + (A_{12} + A_{66})\frac{\partial^2 v_0}{\partial x \partial y} + A_{26}\frac{\partial^2 v_0}{\partial y^2} - B_{11}\frac{\partial^3 w}{\partial x^3} - 3B_{16}\frac{\partial^3 w}{\partial x^2 \partial y} - (B_{12} + 2B_{66})\frac{\partial^3 w}{\partial x \partial y^2} - B_{26}\frac{\partial^3 w}{\partial y^3} = 0 \tag{A.25}$$

$$A_{16}\frac{\partial^2 u_0}{\partial x^2} + (A_{12} + A_{66})\frac{\partial^2 u_0}{\partial x \partial y} + A_{26}\frac{\partial^2 u_0}{\partial y^2} + A_{66}\frac{\partial^2 v_0}{\partial x^2} + 2A_{26}\frac{\partial^2 v_0}{\partial x \partial y} + A_{22}\frac{\partial^2 v_0}{\partial y^2} - B_{16}\frac{\partial^3 w}{\partial x^3} - (B_{12} + 2B_{66})\frac{\partial^3 w}{\partial x^2 \partial y} - 3B_{26}\frac{\partial^3 w}{\partial x \partial y^2} - B_{22}\frac{\partial^3 w}{\partial y^3} = 0 \tag{A.26}$$

$$D_{11}\frac{\partial^4 w}{\partial x^4} + 4D_{16}\frac{\partial^4 w}{\partial x^3 \partial y} + 2(D_{12} + 2D_{66})\frac{\partial^4 w}{\partial x^2 \partial y^2} + 4D_{26}\frac{\partial^4 w}{\partial x \partial y^3} + D_{22}\frac{\partial^4 w}{\partial y^4} - B_{11}\frac{\partial^3 u_0}{\partial x^3} - 3B_{16}\frac{\partial^3 u_0}{\partial x^2 \partial y} - (B_{12} + 2B_{66})\frac{\partial^3 u_0}{\partial x \partial y^2} - B_{26}\frac{\partial^3 u_0}{\partial y^3} - B_{16}\frac{\partial^3 v_0}{\partial x^3} - (B_{12} + 2B_{66})\frac{\partial^3 v_0}{\partial x^2 \partial y} - 3B_{26}\frac{\partial^3 v_0}{\partial x \partial y^2} - B_{22}\frac{\partial^3 v_0}{\partial y^3} = N_x^i\frac{\partial^2 w}{\partial x^2} + 2N_{xy}^i\frac{\partial^2 w}{\partial x \partial y} + N_y^i\frac{\partial^2 w}{\partial y^2} \tag{A.27}$$

A.1.3 Boundary conditions

For the purpose of illustration, we consider a laminate subjected to simply supported boundary conditions and a uni-axial load P_x in the $x-$ direction as shown in Figure A.2. After linearization and separating out the pre-buckling and buckling equaitons, the corresponding boundary conditions for the pre-buckling and buckling problem can be described. From Equation A.8 and Equation A.9, substituting in the linearization from Equation A.10 and Equation A.16

At $x = 0$ and $x = a$,

$$N_x = -P_x \implies N_x^i + \lambda N_x = -P_x \implies N_x^i = -P_x, \quad N_x = 0 \tag{A.28}$$

$$N_{xy} = 0 \implies N_{xy}^i + \lambda N_{xy} = 0 \implies N_{xy}^i = 0, \quad N_{xy} = 0$$

$$w = 0 \implies w^i + \lambda w = 0 \implies w^i = 0, \quad w = 0$$

$$M_x = 0 \implies M_x^i + \lambda M_x = 0 \implies M_x^i = 0, \quad M_x = 0$$

Similarly, at $y = 0$ and $y = b$,

$$N_y = 0 \implies N_y^i + \lambda N_y = 0 \implies N_y^i = 0, \quad N_y = 0 \tag{A.29}$$

$$N_{xy} = 0 \implies N_{xy}^i + \lambda N_{xy} = 0 \implies N_{xy}^i = 0, \quad N_{xy} = 0$$

$$w = 0 \implies w^i + \lambda w = 0 \implies w^i = 0, \quad w = 0$$

$$M_y = 0 \implies M_y^i + \lambda M_y = 0 \implies M_y^i = 0, \quad M_y = 0$$

Thus, collecting the terms as described in the above equations, for pre- buckling,

At $x = 0$ and $x = a$

$$\begin{aligned} N_x^i &= -P_x \quad N_{xy}^i = 0 \\ w^i &= 0 \qquad\quad M_x^i = 0 \end{aligned} \tag{A.30}$$

At $y = 0$ and $y = b$

$$\begin{aligned} N_y^i &= 0 \quad N_{xy}^i = 0 \\ w^i &= 0 \quad M_y^i = 0 \end{aligned} \tag{A.31}$$

And for buckling, the *homogenous boundary conditions* are,

At $x = 0$ and $x = a$

$$\begin{aligned} N_x &= 0 \quad N_{xy} = 0 \\ w &= 0 \quad M_x = 0 \end{aligned} \tag{A.32}$$

At $y = 0$ and $y = b$

$$\begin{aligned} N_y = 0 \quad N_{xy} &= 0 \\ w^i = 0 \quad M_y &= 0 \end{aligned} \tag{A.33}$$

A.2 Special Cases

Special lay-ups, such as cross-ply and angle ply laminates with specific sets of boundary conditions may yield a trivial solution. As discussed in *Jones* (1973), *Qatu and Leissa* (1993), a general laminated plate has a non-zero coupling matrix, *viz.*, $[B_{ij}] \neq 0$ and thus will start to deform out-of-plane as we start to apply an in-plane edge loading. Thus, the concept of a buckling (bifurcation) load, exists only for symmetric laminates and for some special cases of unsymmetric laminates, with the assumption of negligible initial curvatures, as explained in the forthcoming discussions.

For a general laminate, therefore we must solve a geometrically non-linear response problem to extract the transition load. The transition load can be defined as the load at which a significant change in the axial stiffness of the plate occurs. This point is extracted from a plot of the external edge load vs. end displacement. For external loads below this load, the out-of-plane displacements and plate curvatures will remain small. Beyond the transition load, the plate curvatures become large.

A.2.1 Symmetric Laminates

When the laminate is symmetric, invoking the definitions in Equation A.2, the coupling matrix $[B_{ij}] = 0$. This means that from Equation A.2, $\{M^i\} = 0$ for any combination of in-plane loads applied. Thus, a solution $w^i = 0$ exists for the pre- buckling equations, as now the zero state of moments satisfies both the out of plane equilibrium equation and the plate boundary conditions.

Furthermore, when $[B_{ij}] = 0$, the in-plane equations and the out-of plane equations become uncoupled.

Upon inspection, $N_x^i = -P_x$, $N_y^i = 0$, $N_{xy}^i = 0$, in the initially flat pre-buckled state, automatically satisfies the uncoupled in-plane Equation A.5 and Equation A.6. Thus, with this initial solution, Equation A.27 for the out-of-plane buckling equation can be modified as

$$D_{11}\frac{\partial^4 w}{\partial x^4} + 4D_{16}\frac{\partial^4 w}{\partial x^3 \partial y} + 2(D_{12} + 2D_{66})\frac{\partial^4 w}{\partial x^2 \partial y^2} + 4D_{26}\frac{\partial^4 w}{\partial x \partial y^3} + D_{22}\frac{\partial^4 w}{\partial y^4} = N_x^i \frac{\partial^2 w}{\partial x^2} \tag{A.34}$$

Now, $w = 0$ is a trivial solution for this buckling equation, but we seek the existence of a non-trivial solution that will satisfy this equation and the associated homogeneous boundary conditions, Equation A.32 and Equation A.33. Analytical closed-form solution for Equation A.34 is available only for special cases of laminates where D_{16} and D_{26} terms vanish. These are called specially orthotropic laminates, which includes cross-ply laminates ($[0_n/90_m]_s$), $[0]_n$ and $[90]_m$ lay-ups. Equation A.34 subject to homogeneous boundary conditions on w at the plate edges leads to an eigen value problem. The formulation of this eigen value and thus the critical buckling load and mode for such laminates, based on double Fourier series are discussed exhaustively in various textbooks on laminated composites [*Reddy* (2003), *Whitney* (2018)].

A.2.2 Unsymmetric Laminates

Certain special unsymmetric laminates exist where $w^i = 0$ as an analytical solution for the pre- buckling equations are possible. Though coupled, the equations render such that appropriate guesses for the in-plane and out-of-plane deformations that satisfies the equilibrium equations and boundary conditions can be possible.

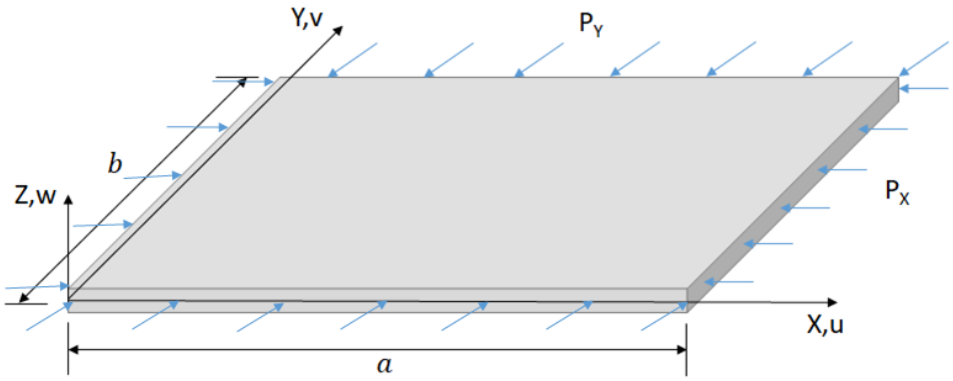

Figure A.3: Buckling of an unsymmetric laminate of special lay-up under uniform bi-axial compression.

Consider the case of laminate that has

$$\begin{aligned} A_{16} = A_{26} &= 0 \\ B_{11} = B_{12} = B_{22} = B_{66} &= 0 \\ D_{16} = D_{26} &= 0 \end{aligned} \tag{A.35}$$

Angle ply laminates of the layup $[\pm\theta]_n$ are such special laminates where these are satisfied [*Whitney* (2018)]. Recently, a class of laminates have come to prominence, called Double-Double (DD) [*Vijayachandran and Waas* (2021)]. Such laminates are of the lay-up $[\pm\theta/\pm\phi]$ and their multiple stacking. There, DD laminates are stacks of $[A/B/A/B...A/B]$ which can be concisely written as $[A/B]_N$ where A and B are pairs of $\pm\theta$ and $\pm\phi$. A variant of such DD laminates exists, of the form $[\pm\theta/\pm\phi/\pm\phi/\pm\theta]_n$ which can be written as $[A/B/B/A]_n$. These may be referred to as $D\bar{D}$

Suppose the plate is supported in the same manner as the previous problem except that there is a proportional bi-axial loading, *i.e.*, $N_x = P_x$ and $N_y = kP_x$, (Figure A.3).

Then at,

$$\begin{aligned} x = 0,\ &\Rightarrow u_0 = 0, \quad N_{xy} = 0,\ w = 0, \quad M_x = 0 \\ x = a,\ &\Rightarrow u_0 \neq 0, \quad N_{xy} = 0,\ w = 0, \quad M_x = 0 \\ y = 0,\ &\Rightarrow v_0 = 0, \quad N_{xy} = 0,\ w = 0, \quad M_y = 0 \\ x = b,\ &\Rightarrow v_0 \neq 0, \quad N_{xy} = 0,\ w = 0, \quad M_y = 0 \end{aligned} \tag{A.36}$$

Thus suppose we assume that,

$$N_x^i = -P_x \ , \quad N_y^i = -kP_x \ , \quad w^i = 0 \tag{A.37}$$

which would be our pre-bucking state. This initial satisfies boundary conditions Equation A.36 and also satisfies the in-plane pre-buckling equations, Equation A.21 and Equation A.22. Now, from Equation A.37 we can find the initial strains ϵ_x^i, ϵ_y^i and γ_{xy}^i. Thus if we have proportional loading, *i.e.*, $N_x = P_x$ and $N_y = kP_x$, then,

$$\left\{ N^i \right\} = \begin{Bmatrix} -P_x \\ -kP_x \\ 0 \end{Bmatrix}$$

Substituting this into Equation A.2

$$\begin{aligned} \Longrightarrow \ A_{11}\epsilon_x^{0i} + A_{12}\epsilon_y^{0i} &= -P_x \\ A_{12}\epsilon_x^{0i} + A_{22}\epsilon_y^{0i} &= -kP_x \\ A_{66}\gamma_{xy}^{0i} &= 0 \end{aligned}$$

and solving the above set of equations provides the strain field

$$\left.\begin{aligned} \implies \qquad \epsilon_x^{0i} &= \frac{(1-k)A_{12}P_x}{A_{12}^2 - A_{11}A_{22}} \\ \epsilon_y^{0i} &= \left(\frac{kA_{11} - A_{12}}{A_{12}^2 - A_{11}A_{22}}\right) P_x \\ \gamma_{xy}^{0i} &= 0 \end{aligned}\right\} \tag{A.38}$$

Substituting Equation A.38 into the second of the Equation A.2

$$\begin{Bmatrix} M_x^i \\ M_y^i \\ M_{xy}^i \end{Bmatrix} = \begin{bmatrix} 0 & 0 & B_{16} \\ 0 & 0 & B_{26} \\ B_{16} & B_{26} & 0 \end{bmatrix} \begin{Bmatrix} \epsilon_x^{0i} \\ \epsilon_y^{0i} \\ \gamma_{xy}^{0i} \end{Bmatrix} \implies M_x^i = 0 \quad M_y^i = 0$$

Thus, the moments $M_x^i = 0$, $M_y^i = 0$ and $M_{xy}^i = B_{16}\epsilon_x^{0i} + B_{26}\epsilon_y^{0i}$ (a constant) satisfies the out-of-plane pre-buckling Equation A.24. Looking at the boundaries, moments $M_x^i = 0$ at $x = 0, a$ and $M_y^i = 0$ at $y = 0, b$ is satisfied by the proposed solution to the pre-buckling equilibrium equations.

The equations that determine the buckling displacements (the perturbations) *Whitney* (2018) are,

$$\left.\begin{aligned} A_{11}\frac{\partial^2 u_0}{\partial x^2} + A_{66}\frac{\partial^2 u_0}{\partial y^2} + (A_{12} + A_{66})\frac{\partial^2 v_0}{\partial x \partial y} - 3B_{16}\frac{\partial^3 w}{\partial x^2 \partial y} - B_{26}\frac{\partial^3 w}{\partial x \partial y^3} &= 0 \\ (A_{12} + A_{66})\frac{\partial^2 u_0}{\partial x \partial y} + A_{66}\frac{\partial^2 v_0}{\partial x^2} + A_{22}\frac{\partial^2 v_0}{\partial y^2} - B_{16}\frac{\partial^3 w}{\partial x^3} - 3B_{26}\frac{\partial^3 w}{\partial x \partial y^2} &= 0 \\ D_{11}\frac{\partial^4 w}{\partial x^4} + 2(D_{12} + 2D_{66})\frac{\partial^4 w}{\partial x^2 \partial y^2} + D_{22}\frac{\partial^4 w}{\partial y^4} - B_{16}\left(3\frac{\partial^3 u_0}{\partial x^2 \partial y} + \frac{\partial^3 v_0}{\partial x^3}\right) \dots & \\ -B_{26}\left(\frac{\partial^3 u_0}{\partial y^3} + 3\frac{\partial^3 v_0}{\partial x \partial y^2}\right) + P_x\left(\frac{\partial^2 w}{\partial x^2} + k\frac{\partial^2 w}{\partial y^2}\right) &= 0 \end{aligned}\right\} \tag{A.39}$$

The solutions to these equations must satisfy the homogeneous boundary condi-

tions. i.e., at $\underline{x = 0, a}$

$$w = M_x = 0$$

$$u_0 = N_{xy} = 0$$

or in explicit form,

$$\left.\begin{aligned} w = 0\ , \quad M_x = B_{16}\left(\frac{\partial v_0}{\partial x} + \frac{\partial u_0}{\partial y}\right) - D_{11}\frac{\partial^2 w}{\partial x^2} - D_{12}\frac{\partial^2 w}{\partial y^2} = 0 \\ u_0 = 0\ , \quad N_{xy} = A_{66}\left(\frac{\partial v_0}{\partial x} + \frac{\partial u_0}{\partial y}\right) - B_{16}\frac{\partial^2 w}{\partial x^2} - B_{26}\frac{\partial^2 w}{\partial y^2} = 0 \end{aligned}\right\} \tag{A.40}$$

Equation A.39 and Equation A.40 are simultaneously satisfied by,

$$\left.\begin{aligned} u_0(x,y) &= A\sin\left(\frac{m\pi x}{a}\right)\cos\left(\frac{n\pi y}{b}\right) \\ v_0(x,y) &= B\cos\left(\frac{m\pi x}{a}\right)\sin\left(\frac{n\pi y}{b}\right) \\ w(x,y) &= C\sin\left(\frac{m\pi x}{a}\right)\sin\left(\frac{n\pi y}{b}\right) \end{aligned}\right\} \tag{A.41}$$

Substituting Equation A.41 into Equation A.39 provides,

$$\begin{bmatrix} k_1 & k_2 & k_3 \\ k_2 & k_4 & k_5 \\ k_3 & k_5 & (k_6 - \lambda) \end{bmatrix} \begin{Bmatrix} A \\ B \\ C \end{Bmatrix} = \begin{Bmatrix} 0 \\ 0 \\ 0 \end{Bmatrix} \tag{A.42}$$

$$k_1 = A_{11}m^2 + A_{66}n^2R^2$$

$$k_2 = (A_{12} + A_{66})mnR$$

$$k_3 = -\frac{n\pi}{b}(3B_{16}m^2 + B_{26}n^2R^2)$$

$$k_4 = A_{66}m^2 + A_{22}n^2R^2$$

$$k_5 = -\frac{m\pi}{Rb}(B_{16}m^2 + 3B_{26}n^2R^2)$$

$$k_6 = \frac{\pi^2}{R^2b^2}(D_{11}m^4 + 2(D_{12} + 2D_{66})m^2n^2R^2 + D_{22}n^4R^4)$$

$$\lambda = P_x(m^2 + kn^2R^2)$$

$$R = \frac{a}{b}$$

The homogeneous linear system, Equation A.42, has the trivial solution,

$$\begin{Bmatrix} A \\ B \\ C \end{Bmatrix} = \begin{Bmatrix} 0 \\ 0 \\ 0 \end{Bmatrix}$$

which produces the pre-buckled displacement field. The condition for a non-trivial solution of Equation A.42 are obtained if

$$\begin{vmatrix} k_1 & k_2 & k_3 \\ & k_4 & k_5 \\ \text{sym} & & (k_6 - \lambda) \end{vmatrix} = 0 \tag{A.43}$$

This leads to,

$$\begin{aligned} P_x = &\frac{\pi^2}{r^2b^2(m^2 + kn^2R^2)}[D_{11}m^4 + 2(D_{12} + 2D_{66})m^2n^2R^2 + D_{22}n^4R^4) \\ &- \frac{1}{J_1}m(B_{16}m^2 + 3B_{26}n^2R^2)J_2 + nR(3B_{16}m^2 + B_{26}n^2R^2)J_3] \end{aligned}$$

where,

$$J_1 = (A_{11}m^2 + A_{66}n^2R^2)(A_{66}m^2 + A_{22}n^2R^2) - (A_{12} + A_{66})^2m^2n^2R^2$$

$$J_2 = (A_{11}m^2 + A_{66}n^2R^2)(B_{16}m^2 + 3B_{26}n^2R^2) - n^2R^2(A_{12} + A_{66})(3B_{16}m^2 + B_{26}n^2R^2)$$

$$J_3 = (A_{66}m^2 + A_{22}n^2R^2)(3B_{16}m^2 + B_{26}n^2R^2) - n^2R^2(A_{12} + A_{66})(B_{16}m^2 + 3B_{26}n^2R^2)$$

The buckling load is the lowest value of P_x. It is an integer function of the wave numbers m, n. For a given laminate and given laminate aspect ratio, $R = \frac{a}{b}, P_x = f(m, n)$. The objective is to find the minimum value of (m, n) that render this. The constant k is associated with the load bi-axiality and is prescribed.

APPENDIX B

Introduction to Double-Double and other non-traditional stacking

Lightweight, stiffness critical aerospace structures are usually thin gage, ranging in thickness from 8-plies (typical pre-preg tape based laminates are used here) to about 48 plies of fiber reinforced laminae, where a nominal lamina (ply) thickness is about 0.0075 in (0.2mm). Buckling under various loading cases is usually a design driver, setting the skin thickness of wings, fuselages, wing boxes, rocket wall thicknesses etc. At the same time, an optimized design calls for non-uniform skin thickness, usually requiring taper. The taper is achieved by ply-drops in traditional manufacturing and may result in resin pockets that can act as stress raisers and regions of lowered local stiffness. Therefore, the quest to manufacture tapered and non-tapered high performing structures efficiently at minimum cost is a continuing challenge. Many air-framers and other manufacturers of lightweight aerostructures have risen to this challenge. Robotically manufactured, steered fiber panels and woven structures are two of the more recent advances that will undoubtedly find significant applications in the future. At the same time, stacking sequences that provide the best pathway for producing thickness tapering, while maximizing structural performance, is also a challenge that needs to be addressed.

Recently, a new class of laminates, referred to as Double-Double (DD) [*Shrivastava et al.* (2020)] has been studied for applications to aerospace structures because of the inherent advantages associated with manufacturability, especially thickness tapering and ease of automation. In these laminates, the stacking sequence is dictated by a lay-up that has the form, $(\theta_1/-\theta_1/\theta_2/-\theta_2)$, where the signs are interchangeable but the angle pairs occur in that order. Stacks of these for appropriate values of θ_1 and θ_2 lead to laminates that have shown ease of manufacturability and thickness tapering. Therefore, a natural question that arises is their structural performance under in-plane loads.

In this paper, we consider the buckling performance of a laminated square plate that is simply supported on all sides and subjected to uni-axial and bi-axial loads. An optimization study produces the lay-ups that maximize the uni-axial buckling loads. These lay-ups are contrasted against the traditional quad-lay-ups and associated DD laminates. For the DD class, both symmetric and unsymmetric lay-ups are studied. In the latter case, in addition to the response problem of a perfectly flat plate, a thermal cycle is used to first manufacture the laminate, followed by the application of in-plane compressive loads, in order to determine the magnitude of load that pushes the laminate to the post-buckled regime.

B.1 Buckling loads and transition loads

Figure B.1 describes the co-ordinates used and Figure. B.2 illustrates the in-plane load and moment resultants in an infinitesimal element of a laminated composite plate. Using Classical Lamination Theory, a constitutive relationship between the force and moment resultants (N and M) and the strains and curvatures (ϵ and χ)

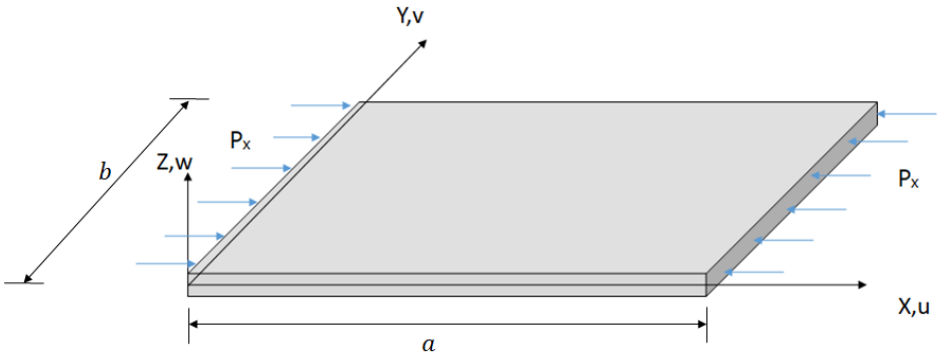

Figure B.1: Co-ordinates used with nomenclature for displacement components

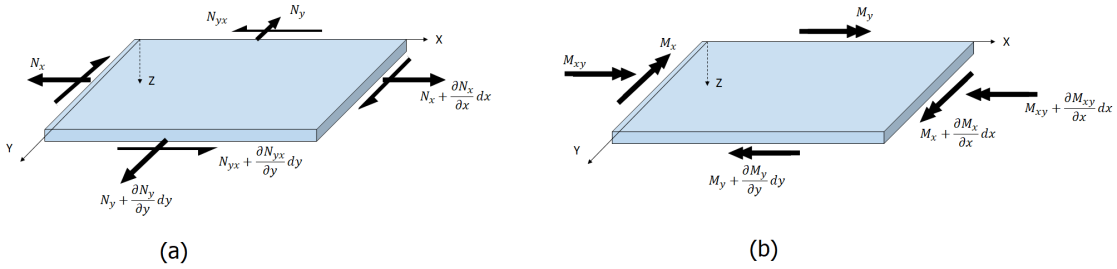

Figure B.2: (a) Force and (b)Moment resultants on an infinitesimal plate element.

are established as in Equation B.1 [*Reddy* (2003)].

$$\begin{Bmatrix} N \\ M \end{Bmatrix} = \begin{bmatrix} A & B \\ B & D \end{bmatrix} \begin{Bmatrix} \epsilon^0 \\ \chi \end{Bmatrix} \tag{B.1}$$

where,

A - Extensional stiffness matrix

B - Coupling (extensional-bending) stiffness matrix

D - Bending stiffness matrix

$$
\begin{aligned}
A_{ij} &= \sum_{k=1}^{n} \bar{Q}_{ij}^{k}(h_k - h_{k-1}) \\
B_{ij} &= \frac{1}{2}\sum_{k=1}^{n} \bar{Q}_{ij}^{k}(h_k^2 - h_{k-1}^2) \\
D_{ij} &= \frac{1}{3}\sum_{k=1}^{n} \bar{Q}_{ij}^{k}(h_k^3 - h_{k-1}^3)
\end{aligned}
\tag{B.2}
$$

The geometrically nonlinear Von-Karman strains, ϵ and curvatures χ, interms of the mid-plane displacements, $u_0(x,y), v_0(x,y)$ and $w(x,y)$, are,

$$
\begin{aligned}
\epsilon_x &= \frac{\partial u_0}{\partial x} - z\frac{\partial^2 w}{\partial x^2} + \frac{1}{2}\left(\frac{\partial w}{\partial x}\right)^2 \\
\epsilon_y &= \frac{\partial v_0}{\partial y} - z\frac{\partial^2 w}{\partial y^2} + \frac{1}{2}\left(\frac{\partial w}{\partial y}\right)^2 \\
\epsilon_{xy} &= \frac{\partial u_0}{\partial y} + \frac{\partial v_0}{\partial x} - 2z\frac{\partial^2 w}{\partial x \partial y} + \frac{\partial w}{\partial x}\frac{\partial w}{\partial y}
\end{aligned}
\tag{B.3}
$$

$$
\begin{Bmatrix} \chi_x \\ \chi_y \\ \chi_{xy} \end{Bmatrix} = \begin{Bmatrix} -\frac{\partial^2 w_0(x,y)}{\partial x^2} \\ -\frac{\partial^2 w_0(x,y)}{\partial y^2} \\ -2\frac{\partial^2 w_0(x,y)}{\partial x}\frac{}{\partial y} \end{Bmatrix}
\tag{B.4}
$$

We consider an initially flat laminate that is subjected to only in-plane loads. The laminate equilibrium equations are then written in the current deformed configuration, where a general point on the mid-plane of the laminate can have non-zero axial displacements and out of plane displacements, respectively. Equation B.5, and Equation B.6, represents the in-plane equations of equilibrium and Equation B.7 represents the out of plane equation for equilibrium, [*Reddy* (2003)].

$$\frac{\partial N_x}{\partial x} + \frac{\partial N_{xy}}{\partial y} = 0 \tag{B.5}$$

$$\frac{\partial N_{xy}}{\partial x} + \frac{\partial N_y}{\partial y} = 0 \tag{B.6}$$

$$N_x \frac{\partial^2 w}{\partial x^2} + 2N_{xy}\frac{\partial^2 w}{\partial x \partial y} + N_y \frac{\partial^2 w}{\partial y^2} + \frac{\partial^2 M_x}{\partial x^2} + 2\frac{\partial^2 M_{xy}}{\partial x \partial y} + \frac{\partial^2 M_y}{\partial y^2} = 0 \tag{B.7}$$

B.1.1 Boundary conditions

For the purpose of this paper, we will consider a laminate that is subjected to simply supported boundary conditions. With the assumed linearization, the boundary conditions for the pre-buckling and buckling problem are as follows.

For pre- buckling,

At $x = 0$ and $x = a$

$$\begin{aligned} N_x^i &= -P_x \\ w^i &= 0 \\ N_{xy}^i = M_x^i \quad &= 0 \end{aligned} \tag{B.8}$$

At $y = 0$ and $y = b$

$$\begin{aligned} v_0^i = w^i \quad &= 0 \\ N_{xy}^i = M_y^i \quad &= 0 \end{aligned} \tag{B.9}$$

and for buckling, the homogenous boundary conditions are,

At $x = 0$ and $x = a$

$$\begin{aligned} N_x &= 0 \\ w &= 0 \\ N_{xy} = M_x \quad &= 0 \end{aligned} \tag{B.10}$$

At $y = 0$ and $y = b$

$$\begin{aligned} v_0 = w \quad &= 0 \\ N_{xy} = M_y \quad &= 0 \end{aligned} \tag{B.11}$$

We next consider the solution of the pre-buckling and buckling equations for symmetric and unsymmetric laminates. We will see that a trivial solution that satisfies the pre-buckling equations and the prebuckling boundary conditions does not exist, in general, for an unsymmetric laminate. Special lay-ups, such as angle ply laminates with specific sets of boundary conditions may yield a trivial solution. As discussed in *Jones* (1973), *Qatu and Leissa* (1993), a generally laminated plate with a non-zero coupling matrix starts to deform out-of-plane as soon as in-plane edge loading is applied. Thus, the concept of a buckling (bifurcation) load, therefore, only exists for symmetric laminates and for some special cases of unsymmetric laminates, with the assumption of negligible initial curvatures. Consequently, we solve a geometrically non-linear response problem for the unsymmetric laminate from which we extract the transition load. The transition load is the load at which a significant change in the plate axial stiffness is seen to take place. This load can be extracted from a plot of the external edge load vs. load-point displacement response plot, as shown later in this note. Furthermore, we observe that for external loads below the transition load, the out-of-plane displacements and plate curvatures remain small. Consequently, the transition load is also the load beyond which the plate curvatures become large.

B.1.2 Symmetric Laminates

In cases I, II, III to be studied later, it is to be noted that the lay-up is symmetric. Thus invoking the definitions in Equation B.2, one could see that the coupling matrix $[B_{ij}] = 0$. Thus, the terms containing $[B_{ij}]$ vanish, thereby uncoupling the in-plane equations from the out-of plane equation.

Upon inspection, $N_x^i = -P_x$, $N_y^i = 0$, $N_{xy}^i = 0$, in the initially flat pre-buckled state, automatically satisfies the uncoupled in-plane Equation B.5 and Equation B.6. Thus, with this initial solution, the out of plane equation takes the form of Equation B.12

$$D_{11}\frac{\partial^4 w}{\partial x^4} + 4D_{16}\frac{\partial^4 w}{\partial x^3 \partial y} + 2(D_{12} + 2D_{66})\frac{\partial^4 w}{\partial x^2 \partial y^2} + 4D_{26}\frac{\partial^4 w}{\partial x \partial y^3} + D_{22}\frac{\partial^4 w}{\partial y^4} = N_x^i \frac{\partial^2 w}{\partial x^2} \tag{B.12}$$

Upon inspection $w = 0$ is a trivial solution, but we seek the existence of a non-trivial solution that will satisfy this equation and the associated homogeneous boundary conditions, Equation B.10 and Equation B.11. Since an analytical closed-form solution for Equation B.12 is not available, numerical methods like the Rayleigh-Ritz method or Finite Element Analysis (FEA) [*Reddy* (2003)] are sought to obtain the solution. In this work, an FEA formulation using the commercial software Abaqus is adopted.

B.1.3 Unsymmetric Laminates

In Case IV, an unsymmetric laminate of the type DD is analyzed. Two problems for this case are considered. First, a fully non linear response problem is analyzed for an initially flat unsymmetric laminate. The expected behavior would dictate a bi-linear response, as stated earlier. The load at the intersection of the two stable equilibrium paths is considered as the transition load for this case. Second, to examine the knock down of the transition load due to initial curvatures that could be caused during the manufacturing, a thermal analysis is first conducted to compute the initial deformation. Next, in-plane edge loading is applied in conjunction with a geometrically nonlinear analysis to capture the reduction in the transition load.

Table B.1: Material Properties of $T800/3900S$

Property	Value	Unit
E_{11}	21.5	Msi
E_{22}	1.23	Msi
ν_{12}	0.329	
G_{12}	0.571	Msi
α_1	-0.1	$\mu m/m^{\circ}C$
α_2	31.6	$\mu m/m^{\circ}C$

B.2 Problem Statement

A flat, square panel, of size 20inx 20in, that is simply supported on all the edges (S4) with an applied in-plane uni-axial compressive load as shown in Fig. 3, is considered. An 8ply, symmetric configuration is considered as the layup. In general this is represented as $[\theta_1/\theta_2/\theta_3/\theta_4]_s$ The material properties of T800/3900S are used, and are detailed in Table B.1.

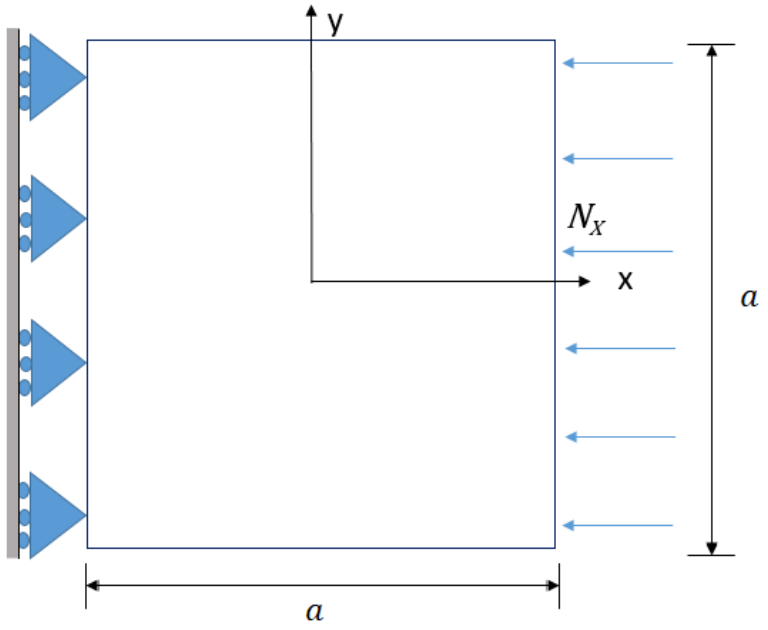

Figure B.3: Loading and Boundary conditions

The optimization problem seeks the maximization of the critical buckling loads

for the three symmetric layup cases, $[\theta_1/\theta_2]_{2s}$,$[\theta_1/-\theta_1/\theta_2/-\theta_2]_s$ and a general $[\theta_1/\theta_2/\theta_3/\theta_4]_s$. The optimization problem seeks the values of θ_i, where, $i = 1, 2$, for the first two cases, and $i = 1 - 4$, for the last case, that would maximize the critical buckling load. The improvement in performance is then compared to the critical buckling load of a legacy quad laminate (LQL) that is commonly used for aerospace applications. It is to be noted that since the number of layers and material remains the same, the mass of all these layups and LQL will remain the same.

Further, for case II laminates, generally referred to as DD or Double-Double, a corresponding unsymmetric lay-up $[\theta_1/-\theta_1/\theta_2/-\theta_2]_2$ is also considered in case IV. No optimization is considered for case IV, but the effect of unsymmetric lay-up in the critical transitional load is analyzed. First, a response problem of an initially flat panel of this unsymmetric lay-up is discussed, comparing the reduction in transitional load to case II. Secondly, since this unsymmetric lay-up is expected to not remain flat after manufacturing, a response problem is considered by first invoking a curing process from $350°F$ to $70°F$, and then obtaining the load displacement response when a compressive in-plane load is applied. After computing the buckling and transition loads for the above four cases, bi-axial buckling under 1:1 and 2:1 bi-axial in-plane loads are investigated.

B.3 Finite Element Model

A commercial FEA package, Abaqus was used to perform the recursive finite element calculations during the optimization process. A python code was set up in Abaqus that would interact with the optimizer to provide the values of objective function in every iteration. Composite shell elements were used with a pixelated mesh of 100 x 100 grid containing 10201 nodes, with each node having three translational and two rotational degrees of freedom.

B.3.1 Symmetric Case

The development of the weak form of Equation B.12 is provided in *Reddy* (2003). A flexural stiffness matrix $[K]$ is obtained from the weakform corresponding to the terms on the left side of Equation B.12 . A geometric stiffness matrix $[G]$, due to a unit distributed load is obtained from the weak form corresponding to the terms on the right side, thus resulting in an eigenvalue problem as shown in Equation B.13.

$$\left[K - \lambda_i G\right] \Phi_i = 0 \tag{B.13}$$

where, λ_i is the i^{th} eigenvalue and Φ_i is the corresponding eigen mode. The critical buckling load corresponds to the lowest eigenvalue.

B.3.2 Unsymmetric Case

Following the weak form formulations for the plate buckling equations, an eigenvalue problem can be set up for this case, though as mentioned earlier, a fully nonlinear response analysis is conducted to find the effect of unsymmetric layup on the transition load. In setting up the eigenvalue problem and proceeding, it turns out that a trivial solution, $w^i = 0$ does not exist for any value of the in-plane external loads. Thus, no eigenvalues exist for the unsymmetric case considered here, and therefore a buckling (bifurcation) load does not exist. However, by performing a geometrically nonlinear response analysis, a transition load can be identified. It is noted that one can seek an eigenvalue for the unsymmetric case considered in this study, using the commercial code Abaqus, but this value does not correspond to any meaningful aspect of the unsymmetric plate response.

We first study the load-displacement response to compute the transition load. A

bi-linear behavior is expected for the response and a transition load is calculated approximately at the intersection of the slopes of the two stable paths. Next, to capture the effect of manufacturing, at first a curing simulation is carried out, subjecting the laminate to a temperature change from $350°F$ to $70°F$. This would provide the initial geometry of the panel after the cure cycle. Next, a response analysis is conducted in which in-plane compressive load is applied to seek the response of the plate and a transition load is identified.

B.4 Optimization Problem

An optimization problem is set up to maximize the buckling load for three different lay-ups- $[\theta_1/\theta_2]_{2s}$,$[\theta_1/-\theta_1/\theta_2/-\theta_2]_s$ and $[\theta_1/\theta_2/\theta_3/\theta_4]_s$, where where, $i = 1, 2$, for the first two cases, and $i = 1-4$, for the third case, respectively. The angles represent the straight fiber angle of each layer. Hence, these $\theta_i's$ become the optimization variables. The bounds on the fiber angles are $-90° \leq \theta_i \leq 90°$. The mathematical representation of the optimization problem is as seen in Equation B.14

$$\begin{aligned} \min_{X} \quad & (-N_{CR}) \\ \text{subject to} \quad & -90° \leq \theta_i \leq 90° \end{aligned} \tag{B.14}$$

where N_{CR} is the critical buckling load , θ_i, ($i = 1, 2$ or $i = 1-4$) are the fiber angles A general optimization work flow is shown in Figure. B.4.

B.5 Results

The three cases studied are described as below. Table 2 shows the comparison of the performance of these results with Legacy Quad $[0/90/\pm 45]_s$ laminates

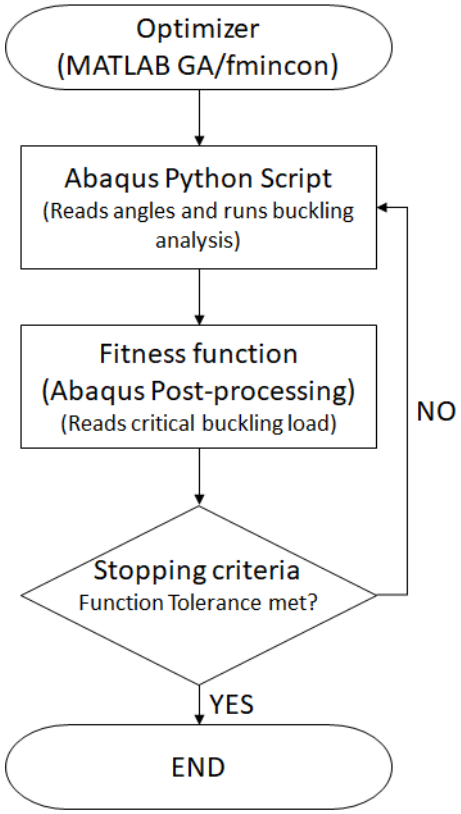

Figure B.4: Workflow for optimization set-up

B.5.1 Case I: $[\theta_1/\theta_2]_{2s}$

Here an 8 ply laminate is considered with the layup $[\theta_1/\theta_2]_{2s}$. A coarse sweep of the design space was conducted to determine the convexity of the objective function. *'fmincon'*, which is Sequential Quadratic Programming (SQP) function in-built in the MATLAB ®optimization toolbox was used to conduct optimization starting at various initial points near the cusps of the objective function in the design space. Since SQP is a gradient based solver, it converges to the closest local minimum. In such a layup, multiple minimum were observed as seen in Figure. B.5. It is interesting to note that, while intuition suggests an 8-ply unidirectional laminate $[0]_8$ might provide the best buckling load, it is only one of the local minima of the objective function.Global minima was observed at $[27/-27]_{2s}$ with buckling load 13.23 lb/in (2.32 N/mm) compared to 11.88lb/in (2.08N/mm) and 9.79lb/in (1.71 N/mm) of unidirectional

and LQL $[0/90/\pm 45]_s$ respectively. Thus these designs offer increased buckling loads of upto 35% compared to LQL. The corresponding mode shapes for $[27/-27]_{2s}$, is shown in Figure B.6.

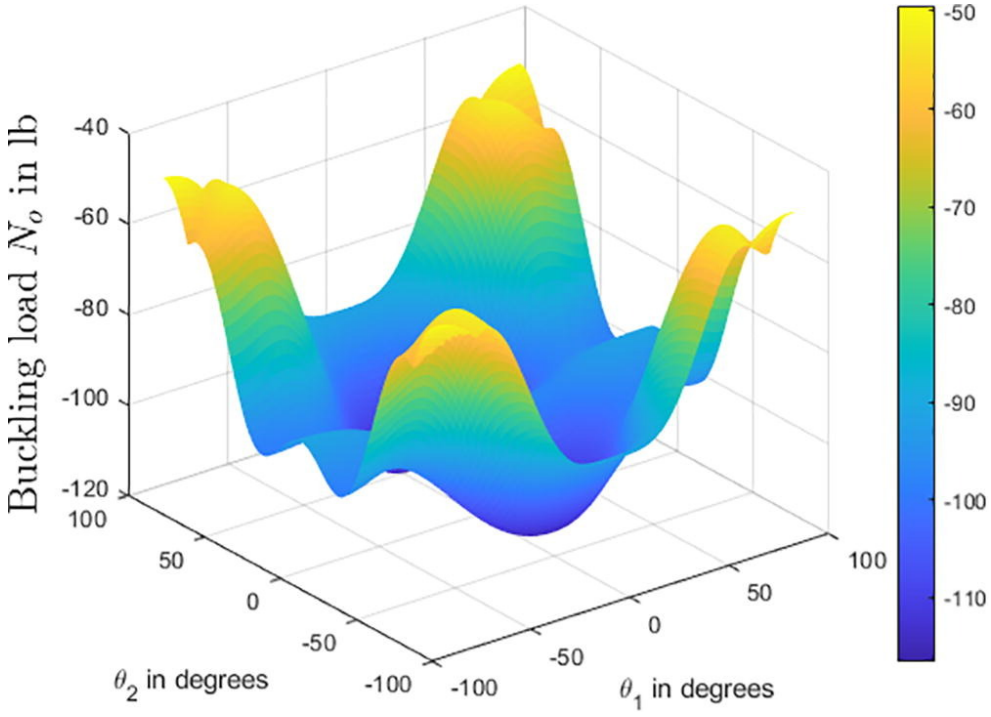

Figure B.5: Response surface obtained for critical buckling loads

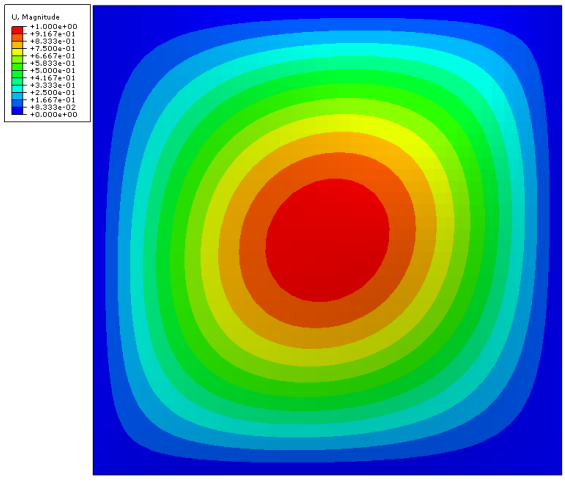

Figure B.6: Critical mode shape for $[27/-27]_{2s}$

B.5.2 Case II: $[\theta_1/-\theta_1/\theta_2/-\theta_2]_s$

In this case, an 8-layer laminate of type DD(Double-Double) is considered. A symmetric layup is considered, as an unsymmetric layup involves a fully populated $[B]$ matrix, and this is relegated to case IV. Similar to as described for Case I, SQP functionality of MATLAB ®was used to perform optimization which converged to a global optimum of $[+41/-41/+2.5/-2.5]_s$. The critical buckling load for this design is 15.4lb/in (2.69N/mm) which is 58% higher than LQL $[0/90/\pm 45]_s$ which has a critical buckling load of 9.79 lb/in(1.71N/mm).The buckling mode is shown in Figure B.7.

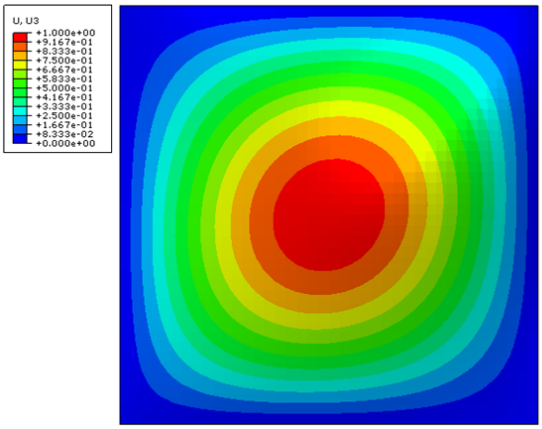

Figure B.7: Critical mode shape for $[+41/-41/+2.5/-2.5]_s$

B.5.3 Case III: $[\theta_1/\theta_2/\theta_3/\theta_4]_s$

In this case, a most general 8-ply, symmetric laminate is considered with each lamina having a discrete fiber angle. While in case I and case II, plotting a response surface was straight forward in an $\mathbb{R}^2$ design space, it was easy to identify points close to a local minima and assign them as initial guess for the SQP application, which converges to the optimum quickly. In this case, we have a $\mathbb{R}^4$ design space and it might be easier to do a direct optimization without a variable sweep. Taking advantage of the less computational time for the FE model, a global optimization technique is

Table B.2: Comparison of Optimal solutions for case I,II,III

Case	Layup	N_{cr} - lb/in (N/mm)
Unidirectional	$[0]_8$	11.88 (2.08)
Legacy Quad	$[0/90/\pm 45]_s$	9.79 (1.71)
Case I	$[\pm 27]_{2s}$	13.23 (2.32)
Case II	$[\pm 41/\pm 2.5]_s$	15.4 (2.69)
Case III	$[41/-42/-6/0]_s$	15.46 (2.71)

used. Genetic Algorithm (GA) function in MATLAB ®global optimization toolbox was used for the same. The global optimum obtained was $[41/-42/-6/0]_s$, with a critical buckling load of 15.46lb/in (2.71N/mm), only higher than Case II by 0.4%. The mode shape is shown in Figure B.8

Table. B.2 describes the optimal solutions of all the cases in comparison to Legacy

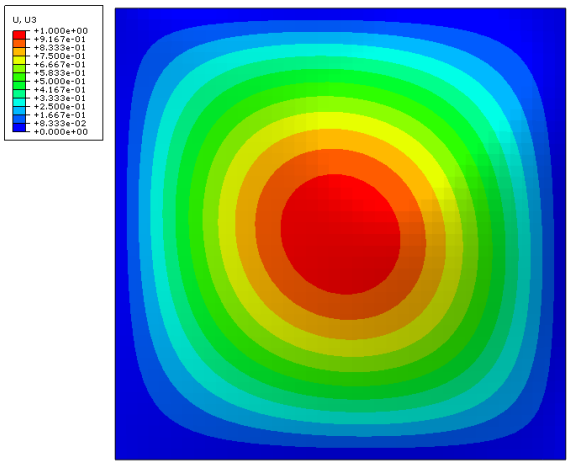

Figure B.8: Critical mode shape for $[41/-42/-6/0]_s$

Quad and Unidirectional Layups

B.5.4 Case IV: Response of $[\theta_1/-\theta_1/\theta_2/-\theta_2]_2$

In the case of unsymmetric laminate the lay-up considered uses the optimal angles from case II as $[+41/-41/+2.5/-2.5]_2$. In the first analysis, a non linear response of the initially flat panel is studied. It shows a clear bi-linear behavior in the axial load v/s axial deformation ($P-\Delta$) plot. This response is then used to calculate

the transition load at the intersection of the slopes of these stable paths as shown in Figure B.9. The transition load is computed as 225lb (1kN) and an equivalent distributed load of 11.25 lb/in (1.97 N/mm), thus causing a 27% reduction in the load compared to case II. A plot of load (P in lb) as a function of out of plane displacement (w in) at the location x=a/4, y=0 is shown in Figure B.10. This plot also points to the transition in response at approximately 200lb.

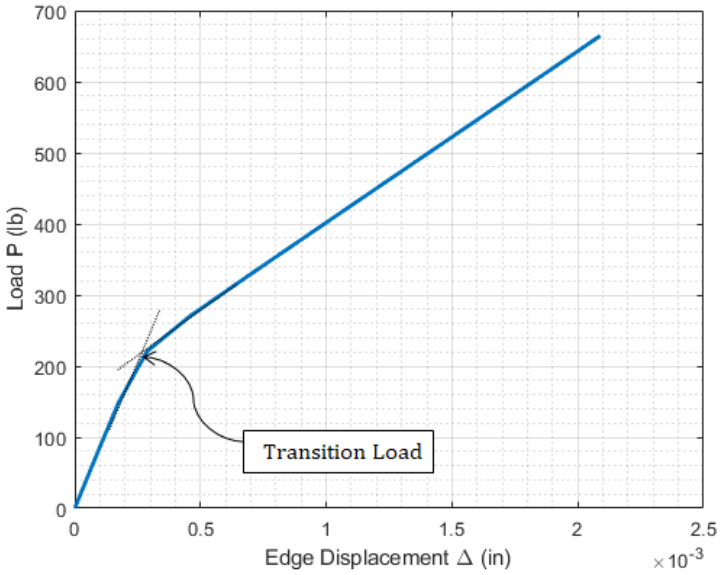

Figure B.9: $P - \Delta$ response of an intially flat $[+41/-41/+2.5/-2.5]_2$panel

Next, a two step fully non linear analysis is conducted, where the first step is a thermal analysis to capture the effect of curing during manufacturing. The flat plate is first subjected to a thermal cycle from $350°F$ to $70°F$. Then a non-linear response analysis is conducted to obtain the transition load.

To obtain the transition load, the load-deflection curve is observed as shown in Figure B.11. An approximately bi-linear response is observed. Slopes are drawn to match the stiffnesses before and after the point of transition. The intersection of these two slopes is the transition load and is calculated as 170 lb. This converts to

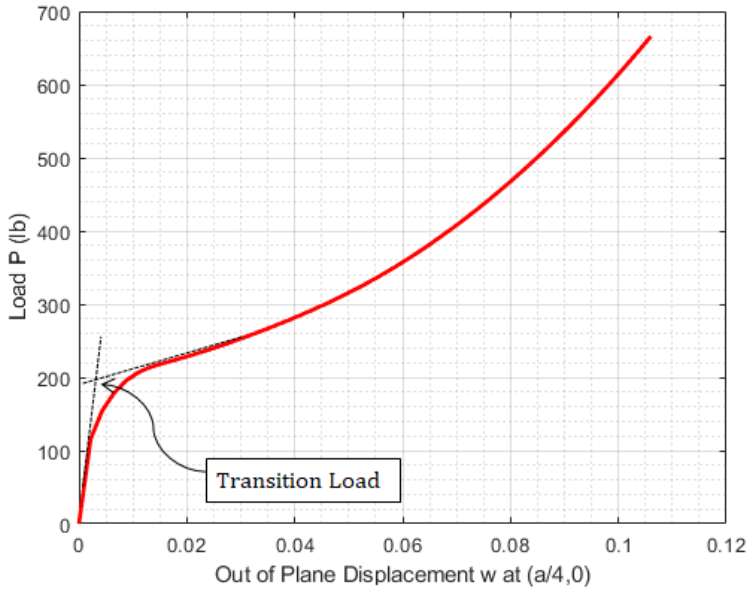

Figure B.10: $P - w$ out of plane displacement w at x=a/4, y=0 for an initially flat $[+41/-41/+2.5/-2.5]_2$panel

an equivalent distributed load of 8.5 lb/in (1.49 N/mm), which is a 45% reduction when compared to the critical buckling load of the corresponding symmetric lay-up in case II. It is also lower than the transition load of the perfectly flat unsymmetric DD laminate response suggesting that the initial manufacturing can influence the axial load carrying capacity and hence the transition load. As the laminate becomes thicker, it is expected that the differences between the symmetric and unsymmetric laminate responses will diminish *Jones* (1973). For the sake of brevity, a similar study was conducted for a 48 ply laminate. The transitional loads of an initially flat $[+41/-41/+2.5/-2.5]_{12}$ and a cured panel of the same layup was compared to the buckling load of a $[+41/-41/+2.5/-2.5]_{6S}$ panel, each of 48 plies. The buckling load of the symmetric panel was computed as 2960lb/in (518N/mm). Transitional loads for an initially flat unsymmetric panel was computed as 2800lb/in (490N/mm) and the cured panel was computed as 2750lb/in (480N/mm). The corresponding reduction in transition loads compared the buckling load of the symmetric panel was only 5% and7% respectively.

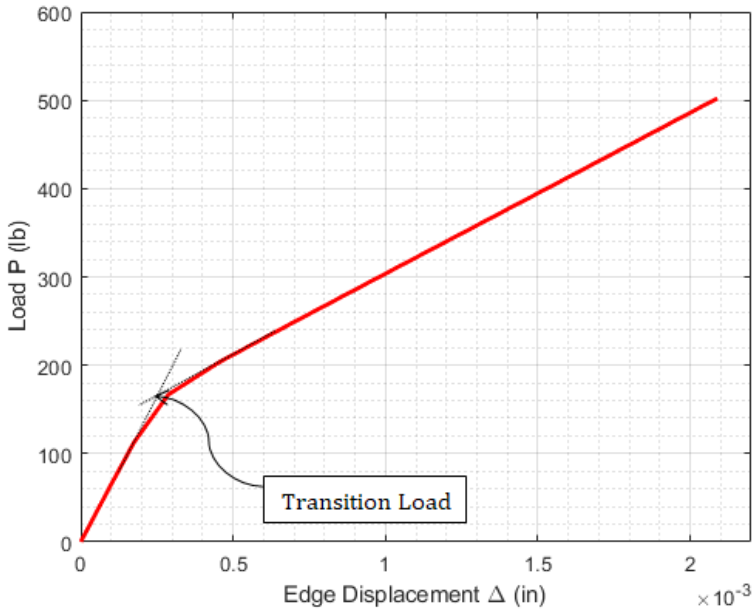

Figure B.11: $P - \Delta$ response for the post curing $[+41/-41/+2.5/-2.5]_2$panel including identification of the transitional load

B.5.5 Response under bi-axial in-plane looads

The three cases of non traditional lay-ups, corresponding to cases I-III have produced significant improvement of the critical buckling load under in-plane uni-axial loading. Among them case II, identified as DD, particularly stands out due to its easiness in manufacturing albeit providing one of the highest uni-axial buckling performance. It is imperative, therefore, that we discuss the performance of these designs under the effect of bi-axial in-plane loads. Two loading cases are considered, 1:1 bi-axial loading and 2:1 bi-axial loading as seen in Figure B.12

B.5.5.1 1:1 Bi-axial loading

A 1:1 bi-axial in-plane loading state, *viz.*, edge loads $N_y = N_x$, is considered. For the LQL lay-up $[0/90/\pm 45]_s$, the critical buckling load in this case is 6.41 lb/in (1.13 N/mm). Each of the designs in cases I-III provide improved buckling performance. In case I, $[\pm 27]_{2s}$ has a critical bi-axial buckling load at 8.26 lb/in (1.45 N/mm),

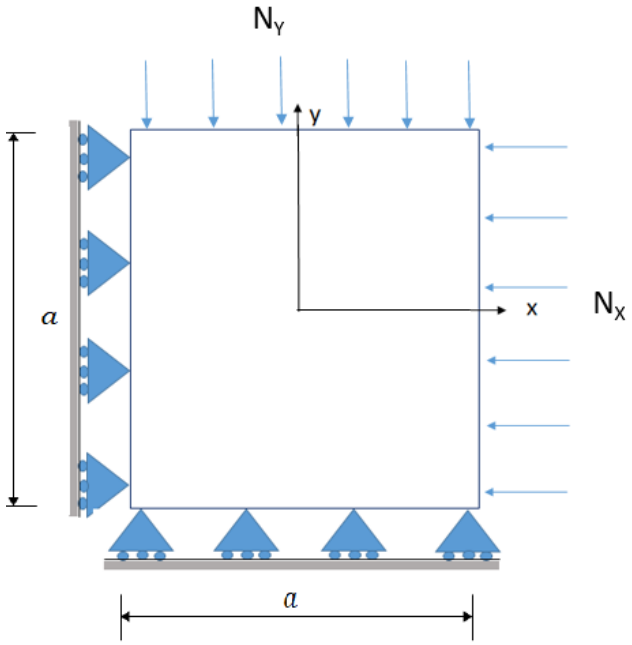

Figure B.12: Case V: Bi-axial loading

providing a corresponding 29 % increase compared to LQL. In cases II nd III, the lay-ups $[\pm 45/\pm 2.5]_s$ and $[41/-42/-6/0]_s$, provides a buckling load of 9.15 lb/in (1.60 N/mm) and 9.23 lb/in (1.62 N/mm) respectively with a corresponding improvement in buckling performance by 43 % and 44%. These results are tabulated in Table B.3.

B.5.5.2 2:1 Bi-axial loading

Similar to the above section, an analysis is conducted to investigate the buckling performance of the optimal solutions under a 2:1 bi-axial in-plane loading state, *viz.*, edge loads $N_y = 2N_x$. For the LQL lay-up $[0/90/\pm 45]_s$ considered, the critical buckling load in this case is 4.28 lb/in (0.75 N/mm). Similar to the 1:1 bi-axial loading, each of the optimal designs in cases I-III provide improved buckling performance. In case I, $[\pm 27]_{2s}$ has a critical bi-axial buckling load at 5.51 lb/in (0.96 N/mm), providing a corresponding 29 % increase compared to LQL. In case II nd III, the lay-ups $[\pm 45/\pm 2.5]_s$ and $[41/-42/-6/0]_s$, provides a buckling load of 6.10 lb/in (1.07

Table B.3: Comparison of 1:1 bi-axial performance of optimal solutions

Case	Layup	$1:1 N_{cr}$ - lb/in (N/mm)
Legacy Quad	$[0/90/\pm 45]_s$	6.41 lb/in (1.13 N/mm)
Case I	$[\pm 27]_{2s}$	8.26 lb/in (1.45 N/mm)
Case II	$[\pm 41/\pm 2.5]_s$	9.15 lb/in (1.60 N/mm)
Case III	$[41/-42/-6/0]_s$	9.23 lb/in (1.62 N/mm)

Table B.4: Comparison of 2:1 bi-axial performance of optimal solutions

Case	Layup	$2:1 N_{cr}$ - lb/in (N/mm)
Legacy Quad	$[0/90/\pm 45]_s$	4.28 lb/in (0.75 N/mm)
Case I	$[\pm 27]_{2s}$	5.51 lb/in (0.96 N/mm)
Case II	$[\pm 41/\pm 2.5]_s$	6.10 lb/in (1.07 N/mm)
Case III	$[41/-42/-6/0]_s$	6.15 lb/in (1.08 N/mm)

N/mm) and 6.15 lb/in (1.08 N/mm) respectively with a corresponding improvement in buckling performance by 43 % and 44%. These results are tabulated in Table Table B.4.

Figures B.13, B.13, B.15shows the critical buckling mode shapes for each of the above cases for both $1:1$ and $2:1$ in-plane bi-axial compressive loads.

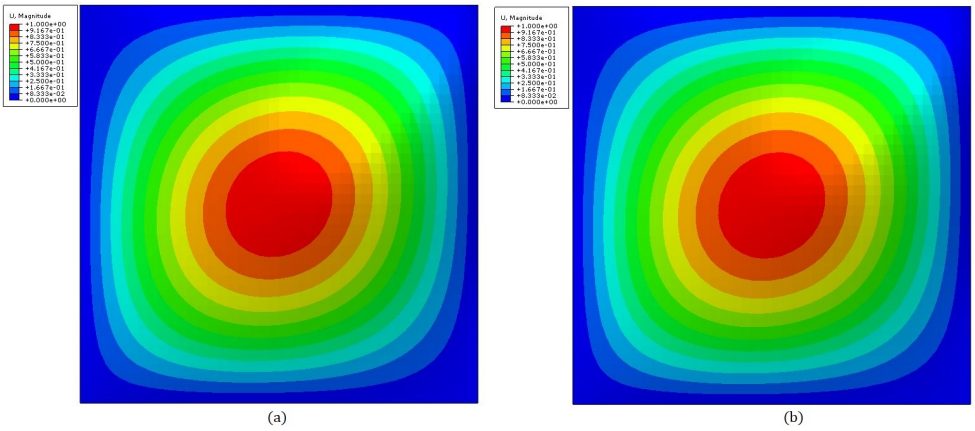

Figure B.13: Critical Mode shape for $[\pm 27]_{2s}$ (a) 1:1 Loading (b) 2:1 Loading

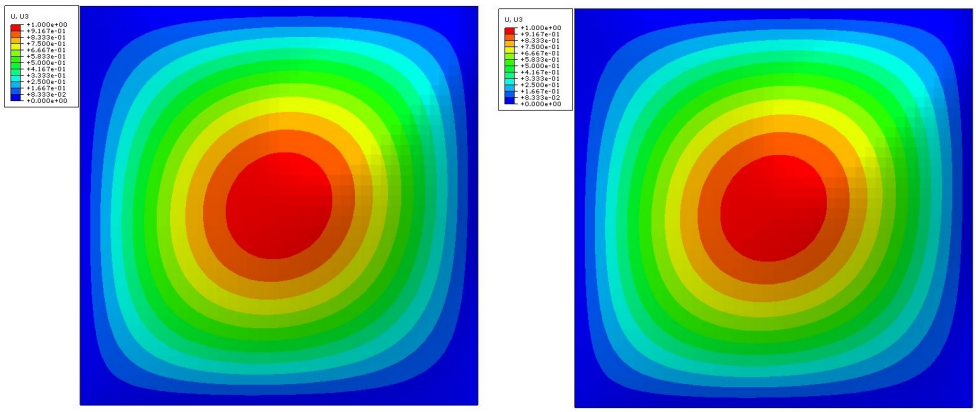

Figure B.14: Critical Mode shape for $[\pm 41/\pm 2.5]_s$ (a) 1:1 Loading (b) 2:1 Loading

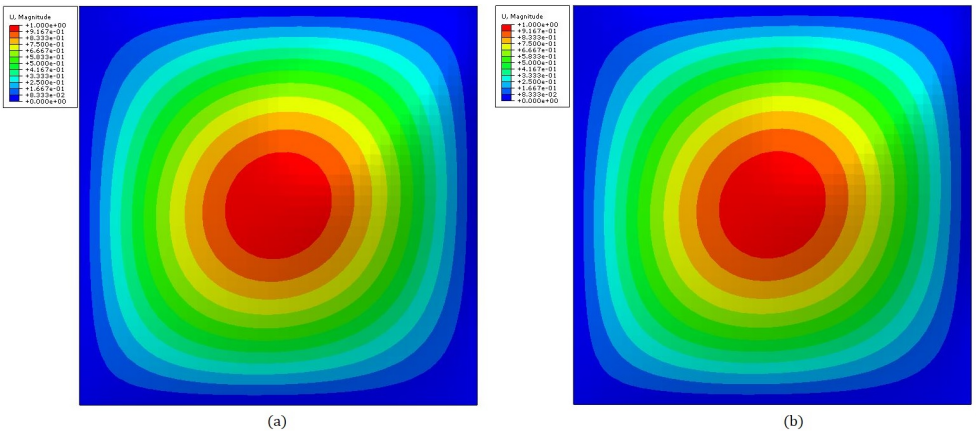

Figure B.15: Critical Mode shape for $[41/-42/-6/0]_s$ (a) 1:1 Loading (b) 2:1 Loading

BIBLIOGRAPHY

BIBLIOGRAPHY

Abdalla, M. M., S. Setoodeh, and Z. GÜrdal (2006), Design of variable-stiffness composite panels for maximum buckling load, in *III European Conference on Computational Mechanics*, pp. 480–480, Springer Netherlands.

Albazzan, M. A., R. Harik, B. F. Tatting, and Z. Gürdal (2019), Efficient design optimization of nonconventional laminated composites using lamination parameters: A state of the art, *Composite Structures*, *209*, 362–374.

Aragh, B. S., E. B. Farahani, B. Xu, H. Ghasemnejad, and W. Mansur (2021), Manufacturable insight into modelling and design considerations in fibre-steered composite laminates: State of the art and perspective, *Computer Methods in Applied Mechanics and Engineering*, *379*, 113,752.

ASTM D7137/D7137M, D. (2017), Standard test method for compressive residual strength properties of damaged polymer matrix composite plates, *ASTM Intl.*, *17*.

Blom, A. W., B. F. Tatting, J. M. Hol, and Z. Gurdal (2006), Path definitions for elastically tailored conical shells, in *47th SDM Conference, Newport, RI*, pp. 1–14, American Institute of Aeronautics and Astronautics Inc.(AIAA).

Blom, A. W., M. M. Abdalla, and Z. Gürdal (2007), Optimization of tow-placed, tailored composite laminates, in *Proceedings of the 16th International Conference on Composite Materials*.

Blom, A. W., S. Setoodeh, J. M. Hol, and Z. Gürdal (2008), Design of variable-stiffness conical shells for maximum fundamental eigenfrequency, *Computers & structures*, *86*(9), 870–878.

Blom, A. W., C. S. Lopes, P. J. Kromwijk, Z. Gurdal, and P. P. Camanho (2009), A theoretical model to study the influence of tow-drop areas on the stiffness and strength of variable-stiffness laminates, *Journal of composite materials*, *43*(5), 403–425.

Blom, A. W., M. M. Abdalla, and Z. Gürdal (2010), Optimization of course locations in fiber-placed panels for general fiber angle distributions, *Composites Science and Technology*, *70*(4), 564–570.

Brampton, C. J., and H. A. Kim (2013), Optimization of tow steered fibre orientation using the level set method, in *10th World Congress on Structural and Multidisciplinary Optimization, Orlando FL*.

Brush, D. O., B. O. Almroth, and J. Hutchinson (1975), Buckling of bars, plates, and shells, *Journal of Applied Mechanics*, *42*(4), 911.

Bruyneel, M., and S. Zein (2011), A new strategy avoiding gaps and overlaps in the simulation of fiber placement trajectories, in *16 th International Conference on Composite Structures ICCS16*, pp. 28–30.

Bruyneel, M., and S. Zein (2013), A modified fast marching method for defining fiber placement trajectories over meshes, *Computers & Structures*, *125*, 45–52.

Coburn, B. H., Z. Wu, and P. M. Weaver (2014), Buckling analysis of stiffened variable angle tow panels, *Composite structures*, *111*, 259–270.

Cohen, B., W. Farren, W. Duncan, and A. Wheeler (1955), Report of the court of inquiry into the accidents to comet g-alyp on 10 january 1954 and comet g-alyy on 8 april 1954, *Her Majesty Station of Office: London, UK*.

Crothers, P., K. Drechsler, D. Feltin, I. Herszberg, and T. Kruckenberg (1997), Tailored fibre placement to minimise stress concentrations, *Composites Part A: Applied Science and Manufacturing*, *28*(7), 619–625.

Demir, E., P. Yousefi-Louyeh, and M. Yildiz (2019), Design of variable stiffness composite structures using lamination parameters with fiber steering constraint, *Composites Part B: Engineering*, *165*, 733–746.

Fayazbakhsh, K., M. A. Nik, D. Pasini, and L. Lessard (2013), Defect layer method to capture effect of gaps and overlaps in variable stiffness laminates made by automated fiber placement, *Composite Structures*, *97*, 245–251.

Fukunaga, H., and H. Sekine (1993), Optimum design of composite structures for shape, layer angle and layer thickness distributions, *Journal of composite materials*, *27*(15), 1479–1492.

Fukunaga, H., and G. N. Vanderplaats (1991), Stiffness optimization of orthotropic laminated composites using lamination parameters, *AIAA journal*, *29*(4), 641–646.

Fukunaga, H., H. Sekine, and M. Sato (1994), Optimal design of symmetric laminated plates for fundamental frequency, *Journal of sound and vibration*, *171*(2), 219–229.

Ghiasi, H., K. Fayazbakhsh, D. Pasini, and L. Lessard (2010), Optimum stacking sequence design of composite materials part ii: Variable stiffness design, *Composite structures*, *93*(1), 1–13.

Gomes, V. S., C. S. Lopes, F. F. A. Pires, Z. Gürdal, and P. P. Camanho (2014), Fibre steering for shear-loaded composite panels with cutouts, *Journal of Composite Materials*, *48*(16), 1917–1926.

Grenestedt, J. (1991), Layup optimization against buckling of shear panels, *Structural optimization*, *3*(2), 115–120.

Grenestedt, J., and P. Gudmundson (1993), Layup optimization of composite material structures, *Optimal design with advanced materials*, pp. 311–336.

Groenwold, A. A., and R. T. Haftka (2006), Optimization with non-homogeneous failure criteria like tsai–wu for composite laminates, *Structural and Multidisciplinary Optimization*, *32*(3), 183–190.

Gurdal, Z., and R. Olmedo (1992), Composite laminates with spatially varying fiber orientations-variable stiffness panel concept, in *33rd Structures, Structural Dynamics and Materials Conference*, p. 2472.

Gurdal, Z., and R. Olmedo (1993), In-plane response of laminates with spatially varying fiber orientations-variable stiffness concept, *AIAA journal*, *31*(4), 751–758.

Gürdal, Z., and B. Tatting (1998), Design and manufacture of tow-placed variable stiffness composite laminates with manufacturing considerations. sl: 13th us national congress of applied mechanics, *June 25th*.

Gurdal, Z., B. Tatting, and K. Wu (2005), Tow-placement technology and fabrication issues for laminated composite structures, in *46th AIAA/ASME/ASCE/AHS/ASC structures, structural dynamics and materials conference*, p. 2017.

Gürdal, Z., B. F. Tatting, and C. Wu (2008), Variable stiffness composite panels: effects of stiffness variation on the in-plane and buckling response, *Composites Part A: Applied Science and Manufacturing*, *39*(5), 911–922.

Hammer, V. B., M. Bendsøe, R. Lipton, and P. Pedersen (1997), Parametrization in laminate design for optimal compliance, *International Journal of Solids and Structures*, *34*(4), 415–434.

Hyer, M. W., and R. Charette (1991), Use of curvilinear fiber format in composite structure design, *AIAA journal*, *29*(6), 1011–1015.

Hyer, M. W., and H. Lee (1991), The use of curvilinear fiber format to improve buckling resistance of composite plates with central circular holes, *Composite structures*, *18*(3), 239–261.

IJsselmuiden, S. T., M. M. Abdalla, and Z. Gurdal (2010), Optimization of variable-stiffness panels for maximum buckling load using lamination parameters, *AIAA journal*, *48*(1), 134–143.

Jegley, D., B. Tatting, and Z. Gurdal (2003), Optimization of elastically tailored tow-placed plates with holes, in *44th AIAA/ASME/ASCE/AHS/ASC Structures, Structural Dynamics, and Materials Conference*, p. 1420.

Jones, R. M. (1973), Buckling and vibration of unsymmetrically laminated cross-ply rectangular plates, *AIAA journal*, *11*(12), 1626–1632.

Khani, A., S. T. IJsselmuiden, M. M. Abdalla, and Z. Gürdal (2011), Design of variable stiffness panels for maximum strength using lamination parameters, *Composites Part B: Engineering*, *42*(3), 546–552.

Khani, A., M. Abdalla, and Z. Gürdal (2015), Optimum tailoring of fibre-steered longitudinally stiffened cylinders, *Composite Structures*, *122*, 343–351.

Khani, A., M. Abdalla, Z. Gürdal, J. Sinke, A. Buitenhuis, and M. Van Tooren (2017), Design, manufacturing and testing of a fibre steered panel with a large cut-out, *Composite Structures*, *180*, 821–830.

Kim, B. C., K. Potter, and P. M. Weaver (2012a), Continuous tow shearing for manufacturing variable angle tow composites, *Composites Part A: Applied Science and Manufacturing*, *43*(8), 1347–1356.

Kim, B. C., K. Potter, and P. M. Weaver (2012b), Multi-tow shearing mechanism for high-speed manufacturing of variable angle tow composites, in *15th European Conference on Composite Materials*.

Kim, B. C., P. M. Weaver, and K. Potter (2014), Manufacturing characteristics of the continuous tow shearing method for manufacturing of variable angle tow composites, *Composites Part A: Applied Science and Manufacturing*, *61*, 141–151.

Kim, B. C., P. M. Weaver, and K. Potter (2015), Computer aided modelling of variable angle tow composites manufactured by continuous tow shearing, *Composite Structures*, *129*, 256–267.

Kirsch, C. (1898), Die theorie der elastizitat und die bedurfnisse der festigkeitslehre, *Zeitschrift des Vereines Deutscher Ingenieure*, *42*, 797–807.

Liguori, F. S., G. Zucco, A. Madeo, D. Magisano, L. Leonetti, G. Garcea, and P. M. Weaver (2019), Postbuckling optimisation of a variable angle tow composite wingbox using a multi-modal koiter approach, *Thin-Walled Structures*, *138*, 183–198.

Lincoln, R. L., P. M. Weaver, A. Pirrera, and R. Groh (2021), Imperfection-insensitive continuous tow-sheared cylinders, *Composite Structures*, *260*, 113,445.

Lopes, C., Z. Gürdal, and P. Camanho (2008), Variable-stiffness composite panels: Buckling and first-ply failure improvements over straight-fibre laminates, *Computers & Structures*, *86*(9), 897–907.

Lopes, C. S., P. P. Camanho, Z. Gürdal, and B. F. Tatting (2007), Progressive failure analysis of tow-placed, variable-stiffness composite panels, *International Journal of Solids and Structures*, *44*(25-26), 8493–8516.

Lopes, C. S., Z. Gürdal, and P. Camanho (2010), Tailoring for strength of composite steered-fibre panels with cutouts, *Composites Part A: Applied Science and Manufacturing*, *41*(12), 1760–1767.

Lucas, D., M. J. Van Tooren, and A. Elham (2017), Stiffness corrections for overlaps and gaps in steered composite panel optimization, in *58th AIAA/ASCE/AHS/ASC Structures, Structural Dynamics, and Materials Conference*, p. 0895.

Madeo, A., R. Groh, G. Zucco, P. M. Weaver, G. Zagari, and R. Zinno (2017), Post-buckling analysis of variable-angle tow composite plates using koiter's approach and the finite element method, *Thin-Walled Structures*, *110*, 1–13.

Mansfield, E. (1953), Neutral iioles in plane sheet—reinforced iioles which are elastically equivalent to the uncut sheet, *The Quarterly Journal of Mechanics and Applied Mathematics*, *6*(3), 370–378.

Marouene, A., R. Boukhili, J. Chen, and A. Yousefpour (2016a), Buckling behavior of variable-stiffness composite laminates manufactured by the tow-drop method, *Composite Structures*, *139*, 243–253.

Marouene, A., R. Boukhili, J. Chen, and A. Yousefpour (2016b), Effects of gaps and overlaps on the buckling behavior of an optimally designed variable-stiffness composite laminates–a numerical and experimental study, *Composite structures*, *140*, 556–566.

Nagendra, S., S. Kodiyalam, J. Davis, and V. Parthasarathy (1995), Optimization of tow fiber paths for composite design, in *36th Structures, Structural Dynamics and Materials Conference*, p. 1275.

Nguyen, M. H., A. A. Vijayachandran, P. Davidson, D. Call, D. Lee, and A. M. Waas (2019a), Effect of automated fiber placement (afp) manufacturing signature on mechanical performance, in *AIAA Scitech 2019 Forum*, p. 0516.

Nguyen, M. H., A. A. Vijayachandran, P. Davidson, D. Call, D. Lee, and A. M. Waas (2019b), Effect of automated fiber placement (afp) manufacturing signature on mechanical performance of composite structures, *Composite Structures*, *228*, 111,335.

Nik, M. A., K. Fayazbakhsh, D. Pasini, and L. Lessard (2014), Optimization of variable stiffness composites with embedded defects induced by automated fiber placement, *Composite Structures*, *107*, 160–166.

Oliveri, V., et al. (2019), Design, manufacture and test of an in-situ consolidated thermoplastic variable-stiffness wingbox, *AIAA Journal*, *57*(4), 1671–1683.

Olmedo, R., and Z. Gurdal (1993), Buckling response of laminates with spatially varying fiber orientations, in *34th Structures, Structural Dynamics and Materials Conference*, p. 1567.

Panesar, A., and P. Weaver (), Optimization of blended bistable laminates for morphing control surfaces, in *51st AIAA/ASME/ASCE/AHS/ASC Structures, Structural Dynamics, and Materials Conference 18th AIAA/ASME/AHS Adaptive Structures Conference 12th*, p. 2988.

Panesar, A. S., and P. M. Weaver (2012), Optimisation of blended bistable laminates for a morphing flap, *Composite Structures*, *94*(10), 3092–3105.

Panesar, A. S., K. Hazra, and P. M. Weaver (2012), Investigation of thermally induced bistable behaviour for tow-steered laminates, *Composites Part A: Applied Science and Manufacturing*, *43*(6), 926–934.

Qatu, M., and A. Leissa (1993), Buckling or transverse deflections of unsymmetrically laminated plates subjected to in-plane loads, *AIAA journal*, *31*(1), 189–194.

Raju, G., Z. Wu, B. C. Kim, and P. M. Weaver (2012), Prebuckling and buckling analysis of variable angle tow plates with general boundary conditions, *Composite Structures*, *94*(9), 2961–2970.

Raju, G., Z. Wu, and P. M. Weaver (2013), Postbuckling analysis of variable angle tow plates using differential quadrature method, *Composite Structures*, *106*, 74–84.

Raju, G., Z. Wu, and P. M. Weaver (2015), Buckling and postbuckling of variable angle tow composite plates under in-plane shear loading, *International Journal of Solids and Structures*, *58*, 270–287.

Raju, G., Z. Wu, S. White, and P. M. Weaver (2018), Optimal postbuckling design of variable angle tow composite plates, *AIAA Journal*, *56*(5), 2045–2061.

Reddy, J. N. (2003), *Mechanics of laminated composite plates and shells: theory and analysis*, CRC press.

Rouhi, M., H. Ghayoor, S. V. Hoa, and M. Hojjati (2014), Effect of structural parameters on design of variable-stiffness composite cylinders made by fiber steering, *Composite Structures*, *118*, 472–481.

Rouhi, M., H. Ghayoor, S. V. Hoa, and M. Hojjati (2015), Multi-objective design optimization of variable stiffness composite cylinders, *Composites Part B: Engineering*, *69*, 249–255.

Senocak, E., and A. Waas (1992), Design considerations for symmetrically laminated plates with cutouts, in *33rd Structures, Structural Dynamics and Materials Conference*, p. 2486.

Senocak, E., and A. M. Waas (1993), Neutrally reinforced holes in symmetrically laminated plates, *Journal of aircraft*, *30*(3), 428–430.

Setoodeh, S., M. M. Abdalla, and Z. Gürdal (2006a), Design of variable–stiffness laminates using lamination parameters, *Composites Part B: Engineering*, *37*(4-5), 301–309.

Setoodeh, S., A. Blom, M. Abdalla, and Z. Gürdal (2006b), Generating curvilinear fiber paths from lamination parameters distribution, in *47th AIAA/ASME/ASCE/AHS/ASC Structures, Structural Dynamics, and Materials Conference*, p. 1875.

Setoodeh, S., M. M. Abdalla, S. T. IJsselmuiden, and Z. Gürdal (2009), Design of variable-stiffness composite panels for maximum buckling load, *Composite Structures*, *87*(1), 109–117.

Shirinzadeh, B., G. Cassidy, D. Oetomo, G. Alici, and M. H. Ang Jr (2007), Trajectory generation for open-contoured structures in robotic fibre placement, *Robotics and Computer-Integrated Manufacturing*, *23*(4), 380–394.

Shrivastava, S., N. Sharma, S. W. Tsai, and P. Mohite (2020), D and dd-drop layup optimization of aircraft wing panels under multi-load case design environment, *Composite Structures*, *248*, 112,518.

Tatting, B. F., and Z. Gurdal (2002), Design and manufacture of elastically tailored tow placed plates.

Tatting, B. F., and Z. Gurdal (2003), Automated finite element analysis of elastically-tailored plates.

Telford, R., D. Peeters, V. Oliveri, G. Zucco, D. Jones, R. O'Higgins, and P. M. Weaver (2018), Enhanced buckling performance of a stiffened, variable angle tow thermoplastic composite panel, in *2018 AIAA/ASCE/AHS/ASC Structures, Structural Dynamics, and Materials Conference*, p. 0480.

Tsai, S., and H. Hahn (1980), Introduction to composite materials, tech-nomic, lancaster, pennsylvania.

van Tooren, M. J., A. Elham, and R. Harik (2015), Optimal variable stiffness distribution for a composite plate with a row of holes subjected to tension/shear load cases, in *16th AIAA/ISSMO Multidisciplinary Analysis and Optimization Conference*, p. 2488.

Van Tooren, M. J., I. Jahangir, and A. Elham (2016), Optimization of variable stiffness composite plates with cut-outs subjected to compression, tension and shear using an adjoint formulation, in *57th AIAA/ASCE/AHS/ASC Structures, Structural Dynamics, and Materials Conference*, p. 1970.

van Zanten, F. J., C. R. Pupo, D. Barazanchy, and M. J. Van Tooren (2019), Optimization of 3d curved fiber steered shells, in *AIAA Scitech 2019 Forum*, p. 0417.

Vijayachandran, A., and A. Waas (2021), On the use of non traditional stacking to maximize critical buckling loads in flat composite panels, *Composite Structures*, *261*, 113,320.

Vijayachandran, A. A., P. Davidson, and A. M. Waas (2017), Optimal paths for steered fibers in a composite laminate with a stress raiser, in *Proceedings of the American Society for Composites—Thirty-second Technical Conference*.

Vijayachandran, A. A., P. Davidson, and A. M. Waas (2019), Manufacturable designs for optimized buckling performance of flat panels using steered fibers, in *Proceedings of the American Society for Composites—Thirty-fourth Technical Conference*.

Vijayachandran, A. A., P. Davidson, and A. M. Waas (2020a), Optimal steered fiber paths for maximizing biaxial buckling load of a flat plate manufactured using afp, in *AIAA Scitech 2020 Forum*, p. 0165.

Vijayachandran, A. A., P. Davidson, and A. M. Waas (2020b), Optimal fiber paths for robotically manufactured composite structural panels, *International Journal of Non-Linear Mechanics*, *126*, 103,567.

Waldhart, C., Z. Gurdal, and C. Ribbens (1996), Analysis of tow placed, parallel fiber, variable stiffness laminates, in *37th Structure, Structural Dynamics and Materials Conference*, p. 1569.

Wang, G. G., and S. Shan (2007), Review of metamodeling techniques in support of engineering design optimization.

Wang, P., X. Huang, Z. Wang, X. Geng, and Y. Wang (2018), Buckling and post-buckling behaviors of a variable stiffness composite laminated wing box structure, *Applied Composite Materials*, *25*(2), 449–467.

White, S. C., P. M. Weaver, and K. C. Wu (2015), Post-buckling analyses of variable-stiffness composite cylinders in axial compression, *Composite Structures*, *123*, 190–203.

Whitney, J. M. (2018), *Structural analysis of laminated anisotropic plates*, Routledge.

Wu, C., Z. Gurdal, and J. Starnes (2002), Structural response of compression-loaded, tow-placed, variable stiffness panels, in *43rd AIAA/ASME/ASCE/AHS/ASC Structures, Structural Dynamics, and Materials Conference*, p. 1512.

Wu, K., and Z. Gurdal (2001), Thermal testing of tow-placed, variable stiffness panels, in *19th AIAA Applied Aerodynamics Conference*, p. 1190.

Wu, K., B. Tatting, B. Smith, R. Stevens, G. Occhipinti, J. Swift, D. Achary, and R. Thornburgh (2009), Design and manufacturing of tow-steered composite shells using fiber placement, in *50th AIAA/ASME/ASCE/AHS/ASC Structures, Structural Dynamics, and Materials Conference 17th AIAA/ASME/AHS Adaptive Structures Conference 11th AIAA No*, p. 2700.

Wu, K. C. (2008), Design and analysis of tow-steered composite shells using fiber placement, in *Proceedings of the ASC 23rd Annual Technical Conference. Memphis, Tennessee*.

Wu, K. C., B. K. Stanford, G. A. Hrinda, Z. Wang, R. A. Martin, and H. A. Kim (2013a), Structural assessment of advanced tow-steered shells, in *54th AIAA/ASME/ASCE/AHS/ASC Structures, Structural Dynamics, and Materials Conference*, p. 1769.

Wu, Z., P. M. Weaver, G. Raju, and B. C. Kim (2012), Buckling analysis and optimisation of variable angle tow composite plates, *Thin-walled structures*, *60*, 163–172.

Wu, Z., P. M. Weaver, and G. Raju (2013b), Postbuckling optimisation of variable angle tow composite plates, *Composite structures*, *103*, 34–42.

Wu, Z., G. Raju, and P. M. Weaver (2015), Framework for the buckling optimization of variable-angle tow composite plates, *AIAA Journal*, *53*(12), 3788–3804.

Wu, Z., G. Raju, and P. M. Weaver (2018), Optimization of postbuckling behaviour of variable thickness composite panels with variable angle tows: Towards "buckle-free" design concept, *International Journal of Solids and Structures*, *132*, 66–79.

Zucco, G., M. Rouhi, V. Oliveri, E. Cosentino, R. O'Higgins, and P. Weaver (2021), Continuous tow steering around an elliptical cut-out in a composite panel, in *AIAA Scitech 2021 Forum*, p. 0918.

Zucco, G., et al. (2020), Static test of a variable stiffness thermoplastic composite wingbox under shear, bending and torsion, *The Aeronautical Journal*, *124*(1275), 635–666.